Entanglement and state characterisation from two-photon interference

DISSERTATION

Submitted for the degree of
Doctor of Philosophy
by
Federica A. Beduini

ICFO - The institute of Photonic Sciences
UPC - Universitat Politecnica de Catalunya

Thesis Advisor: Prof. Dr. Morgan W. Mitchell

September, 2015

ABSTRACT

This thesis analyses the effects of two-photon interference in a polarisation squeezed state under two different points of view: on one hand, it presents a new method to obtain the temporal wavefunction of a state of two photons; on the other hand, it studies the microscopic entanglement properties of a collective nonclassical polarisation state, such as the polarisation squeezed state.

The complete characterisation of an unknown quantum state often requires complicated reconstruction methods due to its complex nature: in the first part of this thesis, we describe a new technique to recover completely the wavefunction of a state with two photons (a "biphoton") with just few simple measurements, thanks to the interference with a coherent reference. With this technique, we reconstruct successfully the wavefunction of single-mode biphotons from a low-intensity narrowband squeezed vacuum state.

Many large collective systems that feature nonclassical properties, e.g. superconductivity and squeezing, show entanglement among their components at their microscopic level. Here we report the first direct study of this kind of entanglement for light polarisation. In analogy with the spin-squeezing inequalities that connect squeezing to entanglement for atomic ensembles, we derive an inequality valid for states with classical polarisation correlations, whose violation implies pairwise entanglement among the photons in the state. We consider a polarisation squeezed state that results from the combination in the same spatial mode of a squeezed vacuum state, generated by an optical parametric oscillator (OPO), and a coherent state with orthogonal polarisations: we find that this kind of state always violates our inequality within the coherence time of the squeezed vacuum state. We also quantify the entanglement between the photon pairs by computing the concurrence of the two-photon reduced density matrix: we find that the states that exhibit higher entanglement satisfy the condition for higher visibility of the two-photon interference. We also find that the concurrence is larger for lower squeezing levels, in agreement with the monogamy of entanglement and in analogy to the atomic case. This translation of spin-squeezing inequalities to the optical domain enables us to test directly the squeezing-entanglement relationship.

We generate a squeezed vacuum state with an OPO and we combine it with a coherent state to generate a polarisation squeezed state and we measure the photon pair counts for different polarisation bases. We recover the density matrices corresponding to different realisations of the polarisation squeezed state via quantum tomography: all the density matrices that we reconstruct with this method are entangled, with concurrence up to 0.7. Our measurements confirm several theoretical predictions, including entanglement of all photon pairs within the squeezing coherence time.

RESUMEN

En esta tesis se analizan los efectos de la interferencia de dos fotones en un estado comprimido en polarización desde dos puntos de vista: por un lado, se presenta un nuevo método para obtener la función de onda temporal de un estado de dos fotones; por el otro, se estudian las propiedades de entrelazamiento microscópico de un estado colectivo de polarización no clásico, como el estado comprimido en polarización.

La completa caracterización de un estado cuántico desconocido requiere frecuentemente métodos de reconstrucción complicados debido a su compleja naturaleza: en la primera parte de esta tesis describimos una nueva técnica para recuperar completamente la función de onda de un estado con dos fotones (un "bifotón") usando pocas medidas sencillas, gracias a la interferencia con un estado coherente de referencia. Con esta técnica, reconstruimos con éxito la función de onda de los bifotones que pertenecen a un estado de vacío comprimido de banda estrecha y de baja intensidad.

Muchos sistemas colectivos con un gran número de partículas que presentan propiedades no clásicas, como por ejemplo superconductividad y estados comprimidos, muestran entrelazamiento entre sus componentes a nivel microscópico. Aquí describimos el primer estudio directo de este tipo de entrelazamiento para los estados de polarización de la luz. En analogía con las desigualdades para estados comprimidos en espín, derivamos una desigualdad válida para estados con correlaciones clásicas en polarización, cuya violación implica entrelazamiento en parejas entre los fotones del estado. Consideramos un estado comprimido en polarización, que es el resultado de la combinación en el mismo modo espacial de un estado de vacío comprimido generado por un oscilador óptico paramétrico (OPO) y de un estado coherente con polarización ortogonal al primero: hallamos que estos estados violan nuestra desigualdad siempre que nos encontremos dentro del tiempo de coherencia del estado de vacío comprimido. Cuantificamos también el entrelazamiento entre las parejas de fotones calculando la *concurrencia* de la matriz de densidad reducida de dos fotones: observamos que los estados que tienen mayor entrelazamiento satisfacen la condición para la visibilidad máxima de la interferencia entre bifotones. Hallamos también que la concurrencia es mayor para niveles de compresión menores, en acuerdo con la *monogamia* del entrelazamiento, siendo este resultado análogo al caso atómico. El trasladar estas desigualdades para los estados comprimidos en espín al dominio óptico nos permite observar directamente la relación entre estados comprimidos y entrelazamiento de manera experimental.

Con este fin generamos un estado de vacío comprimido con un OPO y lo combinamos con un estado coherente para obtener un estado comprimido en polarización y contamos las parejas de fotones en diferentes bases de polarización. Con estas medidas reconstruimos las matrices de densidad que corresponden a diferentes versiones del estado comprimido en polarización usando tomografía cuántica: todas las matrices de densidad que hemos obtenido con este método están entrelazadas, mostrando valores de concurrencia de hasta 0.7. Nuestras medidas confirman las

predicciones teóricas, entre las que se encuentra el entrelazamiento de todas las parejas de fotones dentro del tiempo de coherencia del estado entrelazado.

I believe [...] that light is a wave and a particle, that there's a cat in a box somewhere who's alive and dead at the same time (although if they don't ever open the box to feed it it'll eventually just be two different kinds of dead).

Neil Gaiman, *American Gods*

CONTENTS

1

INTRODUCTION

The connection between light and interference dates back to the seventeenth century, with the first scientific studies on the nature of light by Hooke and Huygens. Nevertheless, the observations they made at the time could also be explained by describing light as composed by particles, so that the wave theory of light has not been universally accepted till the first years of the 19th century, when the double-slit experiment designed by Thomas Young demonstrated the validity of the wave theory of light and of the superposition principle for light waves. About a century later, the wave-particle duality introduced to explain quantum effects put interference and the superposition principle back at the centre of physical investigation. Their importance is highlighted by Feynman, who, in its lectures, refers to the superposition principle as "the only mystery" in quantum mechanics [FLS65], as it lies at the heart of quantum theory, giving rise to many of its peculiar nonclassical features, with entanglement amongst them.

This means that interference can be observed not only with classical light, but also with single photons: a review of photon interference can be found in [Man99]. According to quantum optics, even a single photon can generate interference patterns, as observed by Grangier and his coworkers in 1986 [GRA86]. With two photons, a larger set of effects and experiments are possible, as explained in the review by Greenberger and coworkers [GHZ93]. With a modern version of Young's experiment, Gosh and Mandel [GM87] first observed spatial interference of light at the quantum level: they generated two photons by down conversion and imaged them on a plane, where two single-photon detectors recorded detection events with different separations between the detectors. The signature of the interference between the two photons was the oscillation of coincidence counts that they observed as function of the distance between the detectors.

As with classical light, the effects of the superposition principle can be studied with different types of interferometers. The first experiment of this kind was realised by changing slightly the setup of Ghosh and Mandel to obtain a Mach-Zehnder-like setup: two photons that are generated by down conversion in two different spatial modes are combined in a beam splitter. Two single-photon detectors collected the light at the two output ports of the beam splitter, while they changed the length of one of the arms before the beam splitter. When the lengths of the two arms matched perfectly, they observed a significant decrease in the coincidence events, due to the interference between the two photons. This effect, known as Hong-Ou-Mandel (HOM) effect, is a direct consequence of two-photon interference and it is often used to prove photon indistinguishability, even for photon coming from different sources [KBŻ$^+$06].

Interference causes a variation of the measured intensity when the relative phase between the two photon changes: the phase may be changed by modifying the path of one of the two photons as in the Hong-Ou-Mandel experiment [HOM87], or by adding a Mach-Zehnder interferometer to both arms, as in the Franson interferometer [Fra89]. One can also change the polarisation of the photons before the beam splitter as in the experiment by Shih and Alley (S-A) [SA88].

In all these experiments we observe the interference of two photons, where each one is in a different mode before the beam splitter. However, the state that we can generate with our setup is more similar to a NOON state

$$|\psi_{NOON}\rangle \propto |N,0\rangle + e^{i\phi}\,|0,N\rangle, \tag{1.1}$$

with $N = 2$ photons in a superposition of states where they are always found in the same mode. Also for this class of states it is possible to observe the HOM effect [WXC+08]. Alternatively, one can observe the interference pattern also by changing the phase ϕ between the two polarisation modes, in analogy with the S-A experiment [MLS04]. The period of the interference pattern is smaller as the number of photons in each mode grows, so these states have interesting metrological applications [KM98, MLS04, NOO+07, AAS10, WVB+13].

It is evident that the term *two-photon interference* can be applied to a varied class of experiments. In our case, the two-photon part of the polarisation squeezed state generated by our setup can be similar to a NOON state, with two photons in the two orthogonal polarisation modes, H and V. When we refer to two-photon interference in this thesis, we are pointing at oscillations in the coincidence rates when the phase between the polarisation modes is changed, like the ones that are observed for a NOON state, as in [MLS04].

We have seen that two-photon interference has been widely studied in the last thirty years and that it has been used for different purposes depending on the situation: for example, it is a way to prove the indistinguishability of photons or to highlight the metrological advantage given by NOON state. In this thesis, we employ it as the core element of two different experiments: in the first one, we introduce a new technique to recover complete information about the temporal wavefunction of two photons; the second one demonstrates the presence of microscopic entanglement in a collective state, like the polarisation squeezed state.

In **Chapter 2** we illustrate the concept of the two-photon wavefunction, relating it to already existing work. We then describe how we can obtain the temporal wave-function of an unknown two-photon state with a measurement technique common in quantum optics, i.e. the recording of photon pair statistics for different polarisation bases. The trick is to interfere the unknown state with a low-power coherent state with orthogonal polarisation. Given that the states are stationary, we provide a simple analytic expression to derive the wavefunction from measurements associated to just three polarisation bases.

Chapter 3 gives an overview of spin squeezing and of how it is related to entanglement. We study the entanglement properties of an analogous system, i.e. a polarisation squeezed state, finding results similar to the ones found for atomic spins. In analogy with the atomic case, we show that nonclassical polarisation statistics, e.g. polarisation squeezing, implies two-particle entanglement

in the whole state. In addition, we consider a feasible implementation of a polarisation squeezed state, given by a squeezed vacuum state and a coherent state in orthogonal polarisation modes. We derive the two-photon reduced density matrix by computing the second-order correlation functions and quantify its entanglement with the concurrence, finding that any two photons in the state are entangled.

Chapter 4 describes in detail the experimental setup that allowed us to demonstrate both the effects predicted in the previous Chapters. We explain how the polarisation squeezed state is generated and selected from the wideband background by means of an atomic filter of our design. Particular attention is devoted to the setup that guarantees that the phase between the two polarisation components is stable, allowing the observation of two-photon interference effects. We describe also a system to alternate between phase stabilisation and data acquisition, while synchronising the different parts of the setup.

In **Chapter 5** we present the evidence for two-photon interference in our setup. This demonstrates the feasibility of the two experiments we proposed in Chapters 2 and 3.

Chapter 6 is dedicated to the experimental implementation of the technique presented in Chapter 2. We reconstruct successfully the wavefunction of a weak squeezed vacuum state, using the other component of the polarisation squeezed state as the coherent reference.

Chapter 7 explains how the same setup, but with different settings, gives useful data to recover the two-photon reduced density matrix of a polarisation state. To do this, we use a maximum likelihood algorithm, modified to take into account the imperfections of our setup. All the density matrices we obtain are entangled, in agreement with the predictions of Chapter 3.

Part I

Theory

2

TWO-PHOTON TEMPORAL WAVEFUNCTION RECONSTRUCTION

Wavefunctions are complex functions that describe completely the state of a quantum system. Due to their complex nature, it is not easy to characterise them completely. In this Chapter, we will define the second-order correlation functions that predict the measurement results and their relation to the two-photon temporal wavefunction. We will then describe a new technique that allows us to obtain the two-photon temporal wavefunction of a state due to the interference with an ancillary coherent state.

2.1 PHOTON WAVEFUNCTION

Wavefunctions have been used to represent the state of material particles since the beginning of quantum mechanics: as they obey the superposition principle, they account for all quantum effects that derive from it, e.g. interference and diffraction of matter waves. They are complex functions that are solution to the Schrödinger equation and whose squared modulus is the probability density of finding the particle in a certain position.

The mere existence of a similar function for a photon has been the object of a long debate: a detailed review can be found in [SZ97, SR07]. There is no way to define a photon wavefunction that corresponds *strictly* to the one for material particles: in 1949, Newton and Wigner [NW49] demonstrated that massless spin 0 particles like photons cannot be localised, i.e. there is no localised probability density. This implies that no proper position operator nor eigenstate can be written for the photon: hence, we cannot define a wavefunction as for the massive particles. However, there is a way to bypass this problem, by defining a function ψ whose square modulus gives the energy density, instead of the position probability density [Sip95, BB94]. With this definition, the Maxwell equations become analogous to the Dirac equations of a massless material particle, e.g. the neutrino [BB94]. This makes ψ a good candidate for the photon wavefunction, even if it is not a wavefunction in the strict sense, as it is not related to the position probability density. In this sense, the association of the wavefunction to a particle, typical of the quantum mechanical approach, cannot be applied strictly for the photon: however, ψ is compatible with the interpretation of the photon as an excitation of a mode of the electro-magnetical field, as in quantum field theory. We can then write the one-photon wavefunction for a state $|\lambda\rangle$ in the space-time event ($\mathbf{r}$,t) [Sip95] as

$$\psi_i^{(\lambda)}(\mathbf{r},t) \equiv \langle 0|\hat{a}_i(\mathbf{r},t)|\lambda\rangle, \tag{2.1}$$

where $\hat{a}_i(\mathbf{r}, t)$ is the positive-frequency part of the electric field operator for mode i. Because $\hat{a}_i(\mathbf{r}, t)$ removes one photon, this represents $|\lambda\rangle$ projected onto the one-photon subspace. From now on, we will consider effects that have no relevant spatial structure, so we omit the spatial dependence, keeping only the temporal information. Similarly, the "two-photon wave function" (TPWF)is [SSR95]

$$\psi_{i,j}^{(\lambda)}(t_1, t_2) \equiv \langle 0|\hat{a}_i(t_1)\hat{a}_j(t_2)|\lambda\rangle. \tag{2.2}$$

As with Schrödinger wave functions, neither $\psi_i^{(\lambda)}(t)$ nor $\psi_{i,j}^{(\lambda)}(t_1, t_2)$ is directly observable.

In many experiments, the performance of a source of correlated photon pairs, or *biphotons*, is closely tied to the two-photon wave function that describes the temporal correlations of the photons. For example, the visibility of Hong-Ou-Mandel interference depends on the TPWF, even when some other degree of freedom, e.g. polarisation, is used to encode quantum information [ASMS07]. Measurements of the TPWF are also used to characterise realistic photon pairs sources, allowing the diagnosis of experimental defects, e.g. imperfect poling in the down-conversion crystal [KWKT08] or dispersion [OU09].

The TPWF $\psi(t_1, t_2)$ is an intrinsically multi-dimensional object, depending on the two time coordinates t_1 and t_2 [VCS+07]. Methods to characterise the TPWF include measurement of the joint spectral density [MLS+08], measurement of the joint temporal density [KWKT08], non-classical interference using the Hong-Ou-Mandel effect [SSR95, GMSW02, OTS06], and nonlinear optical processes [DPFS04, PDFS05, OU09, SAKYH09]. All of these techniques give partial information about the TPWF. For example, the joint temporal density gives the magnitude $|\psi(t_1, t_2)|$, while the joint spectral density gives the magnitude of the Fourier components.

Full measurement of the TPWF requires a phase-sensitive and tomographic measurement, applied to a continuous range of time values. Some elements of this approach have been demonstrated: quantum state tomography [SBRF93] has been widely used to characterise aggregate measures of a quantum state, e.g. the integrated field of a pulse, or the mode describing a single frequency component. This includes traditional homodyne methods using strong local oscillators [SBRF93] and mesoscopic methods using weak local oscillators plus photon-counting detection [PLB+09]. Homodyne [NNNH+06, MFL13] and polychromatic heterodyne [QPB+15] characterisation of a single photon wave function has also been reported. A recent experiment [CSG+15] showed complete wavefunction reconstruction without a coherent state as a reference for spontaneous four-wave mixing in cold atoms, where the two photons are in different spatial and frequency mode.

Here we demonstrate full characterisation of a two-photon wave function, based on the phenomenon of interference of two-photon amplitudes [TM97, LO01, DEW+13]. A similar method is proposed in [RH12]. Our approach [BZL+14] combines the use of a weak phase reference and photon counting detection as in [PLB+09] with wave-function detection over an extended timespan as in [NNNH+06, MFL13], and adds the new elements of time-correlated photon counting, as required by the dimensionality of the TPWF. An attractive feature of our approach is a very direct data interpretation, without the ill-posed inverse problem typically encountered in tomography.

2.2 CORRELATION FUNCTIONS

The complex nature of wavefunctions prevents the collection of complete information with a single direct measurement. However, their square modulus can be easily connected to the *correlation functions*:

$$G^{(1)}_{i,j}(\tau) \equiv \langle\, \hat{a}^\dagger_i(t)\, \hat{a}_j(t+\tau)\,\rangle \qquad \textit{first}-\textit{order} \tag{2.3}$$

$$G^{(2)}_{ij,mn}(\tau) \equiv \langle\, \hat{a}^\dagger_i(t)\hat{a}^\dagger_j(t+\tau)\hat{a}_n(t+\tau)\hat{a}_m(t)\,\rangle \qquad \textit{second}-\textit{order}. \tag{2.4}$$

where $i, j, n, m \in \{H, V\}$, H and V correspond to horizontal and vertical polarisation, respectively, and $\mathbf{G}^{(k)}$ is a $2^k \times 2^k$ matrix in the computational basis. We have inverted the last two indices in the definition of $\mathbf{G}^{(2)}$, keeping the convention in photonic quantum state tomography [JKMW01]. The above expressions do not depend on t when considering stationary fields, as we will do throughout this thesis. It is easy to see that $|\psi^{(\lambda)}_i(t)|^2 \propto G^{(1)}_{i,i}(0)$ when $|\lambda\rangle$ contains at most one photon and that $|\psi^{(\lambda)}_{i,j}(t_1, t_2)|^2 \propto G^{(2)}_{ij,ij}(t_1 - t_2)$ when there are no more than two photons in $|\lambda\rangle$. The correlation functions are fundamental tools for the prediction of the experimental outcomes in a photonic experiment. The theory of photodetection developed by Glauber [Gla63] connects them to the rate of detected photons, so that the rate $R^{(1)}_{\mathbf{p}}$ of detecting one photon with polarisation described by the unit vector $\mathbf{p}$ is

$$R^{(1)}_{\mathbf{p}} \propto \langle\, \hat{a}^\dagger_{\mathbf{p}}(t)\hat{a}_{\mathbf{p}}(t)\,\rangle = \mathrm{Tr}[\Pi_{\mathbf{p}}\, \mathbf{G}^{(1)}(0)], \tag{2.5}$$

where $\Pi_{\mathbf{p}} = \mathbf{p} \wedge \mathbf{p}$ is a projector onto $\mathbf{p}$. Similarly, the detection rate within a detection window $\Delta\tau$ for a pair of photons, one with polarisation $\mathbf{p}$ at time t and the other with polarisation $\mathbf{q}$ at time $t+\tau$, is

$$\begin{aligned} R^{(2)}_{\mathbf{p}\otimes\mathbf{q}}(\bar{\tau}) &\propto \int_{\bar{\tau}-\Delta\tau/2}^{\bar{\tau}+\Delta\tau/2} \langle\, \hat{a}^\dagger_{\mathbf{q}}(t)\hat{a}^\dagger_{\mathbf{p}}(t+\tau)\hat{a}_{\mathbf{p}}(t+\tau)\hat{a}_{\mathbf{q}}(t)\,\rangle \mathrm{d}\tau \\ &= \int_{\bar{\tau}-\Delta\tau/2}^{\bar{\tau}+\Delta\tau/2} \mathrm{Tr}[\Pi_{\mathbf{p}\otimes\mathbf{q}}\, \mathbf{G}^{(2)}(\tau)]\mathrm{d}\tau. \end{aligned} \tag{2.6}$$

If we normalise the expressions above to obtain detection probabilities $P^{(k)} \equiv R^{(k)}/\mathrm{Tr}\left[\mathbf{G}^{(k)}\right]$ instead of detection rates, we obtain

$$P^{(1)}_{\mathbf{p}} = \mathrm{Tr}[\Pi_{\mathbf{p}}\, \mathcal{G}^{(1)}(0)], \tag{2.7}$$

$$P^{(2)}_{\mathbf{p}\otimes\mathbf{q}} = \mathrm{Tr}[\Pi_{\mathbf{p}\otimes\mathbf{q}}\, \mathcal{G}^{(2)}(\tau)], \tag{2.8}$$

which are the Born rules for the k-photon *observable density matrices* (ODM)

$$\mathcal{G}^{(k)} \equiv \mathbf{G}^{(k)}/\mathrm{Tr}\left[\mathbf{G}^{(k)}\right], \tag{2.9}$$

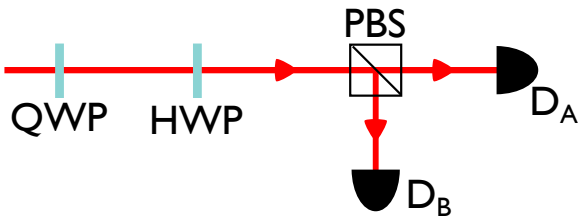

Figure 2.1: Polarimeter setup.

which describe the polarisation state associated to the observed photons. The ODM is different from the density matrix of the whole state before the detection, unless it has exactly k photons. Even if the ODM does not give a complete description of the state of the light pre-detection, it is a convenient way to model the outcome of a real experiment that involves the detection of k photons. In fact, this approach takes into account many of the imperfections that may occur in a real experiment: the ODM is invariant with respect to losses, and it can be obtained also for mixed states. Moreover, in real implementations it happens often that the state does not contain exactly k photons, i.e. it is not a Fock state, but it is a superposition of Fock states with different photon numbers: the k-photon ODM includes also the contribution of the detection of k photons belonging to the Fock components associated to photon numbers larger than k. Given these properties, we can conclude that the discrete quantum state tomography technique [JKMW01], applied to the photon detection rates $R^{(k)}$ measured for different polarisation bases, gives the k-photon ODM as a result.

2.3 RECONSTRUCTION TECHNIQUE

Here we show how the correlation functions defined previously can connect measurable quantities to theoretical predictions, e.g. the temporal wavefunction of a two-photon state $|\lambda\rangle$.

We consider a scenario in which $|\lambda\rangle$ occupies one propagating mode (V), while a time-independent coherent state $|\alpha\rangle$ occupies an ancilla mode (H). The global state is then $|\kappa\rangle = |\lambda\rangle \otimes |\alpha\rangle$ and we measure it with a polarimeter setup like the one in Fig. 2.1, where a quarter- (QWP) and a half-wave plate (HWP) apply a unitary transformation on the polarisation, then a polarisation beam splitter (PBS) separates the two polarisation components, so that the field operator polarisation associated to the single photon detector A(B) is

$$\hat{a}_A(t) = \cos\theta\, \hat{a}_H(t) + e^{i\phi} \sin\theta\, \hat{a}_V(t)\,, \tag{2.10}$$

$$\hat{a}_B(t) = e^{-i\phi} \sin\theta\, \hat{a}_H(t) - \cos\theta\, \hat{a}_V(t)\,, \tag{2.11}$$

where θ and ϕ are the polar and azimuthal angle in the Bloch sphere, respectively.

The two-photon wavefunction associated to the global state $|\kappa\rangle$ takes the form

$$\tilde{\psi}^{(\kappa)}_{AB}(t_1, t_2) = \langle 0|\hat{a}_A(t_1)\hat{a}_B(t_2)|\kappa\rangle. \tag{2.12}$$

We cannot directly measure this quantity, but its squared modulus is proportional to the rate of photon pairs detected by the detectors A and B when both $|\lambda\rangle$ and $|\alpha\rangle$ contain at maximum two photons each:

$$|\tilde{\psi}^{(\kappa)}_{AB}(t_1,t_2)|^2 \propto \langle\kappa|\hat{a}^\dagger_B(t_2)\hat{a}^\dagger_A(t_1)\hat{a}_A(t_1)\hat{a}_B(t_2)|\kappa\rangle = G^{(2)}_{BA,BA}(t_1-t_2). \tag{2.13}$$

The two-photon wave function of the global state becomes then

$$\begin{aligned}\tilde{\psi}^{(\kappa)}_{AB}(t_1,t_2) =& e^{-i\phi}\cos\theta\sin\theta\,\psi^{(\alpha)}_{H,H}\,\langle 0|\lambda\rangle - e^{i\phi}\cos\theta\sin\theta\,\psi^{(\lambda)}_{V,V}(t_1,t_2)\,\langle 0|\alpha\rangle \\ &+\sin^2\theta\,\psi^{(\lambda)}_V(t_1)\,\psi^{(\alpha)}_H - \cos^2\theta\,\psi^{(\alpha)}_H\,\psi^{(\lambda)}_V(t_2),\end{aligned} \tag{2.14}$$

where we omitted the time dependence of the wavefunctions associated to the H mode, because the both the one-photon and the two-photon wavefunctions of a monochromatic and stationary coherent state are independent of the detection time.

The last line in Eq. (2.14) vanishes for a broad class of states $|\lambda\rangle$ that includes the ones generated by experiments using spontaneous, i.e. vacuum-driven, down-conversion, including squeezed vacuum states. In fact, the down-conversion hamiltonian $H \propto \chi^{(2)} a^\dagger_V a^\dagger_V a_p + \text{h.c.}$, and the dephasing and decoherence processes are invariant under

$$\hat{a}_V(t) \to -\hat{a}_V(t), \tag{2.15}$$

or equivalently

$$a_V(\omega) \to a_V(\omega)\exp[i\pi], \tag{2.16}$$

which implies $\psi^{(\lambda)}_V(t) = \langle 0|\hat{a}_V(t)|\lambda\rangle = 0$.

If we consider only stationary fields, $\tilde{\psi}^{(\kappa)}_{AB}$ depends only on the detection time difference $\tau = t_1 - t_2$. Taking $\theta = \pi/4$ for simplicity and following Eqs. (2.6) and (2.13), we can write the measurable second order correlation function as

$$R^{(2)}_{BA,BA}(\bar{\tau}) \propto \int_{\bar{\tau}-\Delta\tau/2}^{\bar{\tau}+\Delta\tau/2} |\tilde{\psi}^{(\kappa)}_{AB}(\tau)|^2 d\tau. \tag{2.17}$$

For a small detection window $\Delta\tau$, we can approximate the integral in the previous expression:

$$R^{(2)}_{BA,BA}(\bar{\tau}) \approx \left|\tilde{\psi}^{(\kappa)}_{AB}(\bar{\tau})\right|^2 \Delta\tau \propto \left|\gamma e^{-2i\phi} - \psi^{(\lambda)}_{V,V}(\bar{\tau})\right|^2, \tag{2.18}$$

where $\gamma = \psi^{(\alpha)}_{H,H}\langle 0|\lambda\rangle\langle 0|\alpha\rangle^{-1}$. We note that now $R^{(2)}_{BA,BA}$, which is directly measurable, contains information about the phase of $\psi^{(\lambda)}_{V,V}(\bar{\tau})$, through interference against $|\alpha\rangle$. For convenience, we choose the phase origin so that α, and thus γ, is real. To find $\psi^{(\lambda)}_{V,V}$, it is convenient to measure with the azimuthal angle $\phi_k = k\pi/3$, $k = \{0,1,2\}$, i.e., symmetrically placed within the period of $\exp[2i\phi_k]$. We denote the resulting values of $R^{(2)}_{BA,BA}(\bar{\tau})$ when $\phi = \phi_k$ as y_k.

It is then possible to solve Eq. (2.18) to obtain the TPWF

$$\psi_{VV}^{(\lambda)} = \mathring{y}/\gamma\,, \tag{2.19}$$

$$\mathring{y} \equiv -\sum_{k=0}^{2} y_k \frac{e^{-ik2\pi/3}}{3}\,, \tag{2.20}$$

$$\gamma = \frac{1}{\sqrt{2}}\sqrt{\bar{y} + \sqrt{3\bar{y}^2 - 2\overline{y^2}}}\,, \tag{2.21}$$

where $\bar{y} \equiv (y_0 + y_1 + y_2)/3$ and $\overline{y^2} \equiv (y_0^2 + y_1^2 + y_2^2)/3$, keeping in mind that $\psi_{V,V}^{(\lambda)}$, the y_k and γ all depend on $\bar{\tau}$.

This result is remarkable for its simplicity; the inverse problem to find $\psi_{VV}^{(\lambda)}$ from the various $R_{BA,BA}^{(2)}(\bar{\tau})$ measurements gives an analytic solution. With the addition of a coherent state, we relate a measurable quantity to the two-photon wavefunction, recovering both its real and imaginary parts from experimental results.

3

OPTICAL SPIN SQUEEZING

Spin squeezing is an interesting source of entanglement: being a collective phenomenon, it implies entanglement among its components. By measuring the moments of the collective spin vector, it is possible to detect and quantify entanglement by means of spin-squeezing inequalities (SSIs). In this Chapter we propose an inequality with analogous characteristics, whose violation implies entanglement of the two-photon reduced density matrix of a photonic system. In analogy with the SSIs for atoms, polarisation squeezing of a light beam violates our inequality. Moreover, we show that every pair of photons is entangled in a polarisation squeezed state generated by merging the output of a sub-threshold optical parametric oscillator and a coherent state in the same spatial mode. Finally, we estimate the amount of entanglement that can be feasibly generated in an experiment.

3.1 SQUEEZING

In general, the squeezing of a quantity $\hat{O}$ is defined as a reduction of its variance $(\Delta\hat{O})^2 = \langle \hat{O}^2 \rangle - \langle \hat{O} \rangle^2$ below a standard quantum limit. Depending on the system or the application, one can choose a different limit, so that multiple definitions of squeezing coexist.

If we consider an atomic ensemble composed of $2J$ atoms with spin $1/2$, we can define and measure the collective spin $\hat{\mathbf{J}}$, which is the sum of all the individual spins of the ensemble. This can be decomposed in $\hat{J}_{\parallel}$, which is parallel to the average spin vector $\langle \hat{\mathbf{J}} \rangle$, and in $\hat{\mathbf{J}}_{\perp}$, which is orthogonal to it. The most intuitive definition of squeezing of the spin vector for such a system is the one given by Kitagawa and Ueda [KU93], where the standard quantum limit is set by the coherent spin states [Rad71], the atomic equivalent of optical coherent states:

$$(\Delta J_{\perp})^2 \geqslant 2J. \tag{3.1}$$

The states that violate the above inequality are squeezed. They have small fluctuations in the plane perpendicular to $\langle \hat{\mathbf{S}} \rangle$, but this does not necessarily imply a metrological advantage. A stricter definition by Wineland and coworkers [WBI+92, WBIH94]

$$2J\frac{(\Delta J_{\perp})^2}{\left|J_{\parallel}\right|^2} \geqslant 1 \tag{3.2}$$

is violated by states that improve the accuracy of spectroscopy measurements, e.g. as in atomic clocks.

Similar definitions for squeezing can be found for the squeezing of the polarisation of light. In fact, the Stokes operators, which are the four operators that describe the polarisation of a quantised optical field, are equivalent to the Schwinger representation of angular-momentum operators for atoms. They are defined as functions of $\hat{a}_i$ and $\hat{a}_i^\dagger$, which are the annihilation and creation operators associated to a frequency mode with polarisation $i \in \{H, V\}$ of an electromagnetic field [KLL+02]:

$$\begin{aligned} S_0 &= \hat{a}_H^\dagger \hat{a}_H + \hat{a}_V^\dagger \hat{a}_V, & S_x &= \hat{a}_H^\dagger \hat{a}_H - \hat{a}_V^\dagger \hat{a}_V, \\ S_y &= \hat{a}_H^\dagger \hat{a}_V + \hat{a}_V^\dagger \hat{a}_H, & S_z &= -i\left(\hat{a}_H^\dagger \hat{a}_V - \hat{a}_V^\dagger \hat{a}_H\right). \end{aligned} \tag{3.3}$$

The commutation relations of the creation and annihilation operators,

$$\left[\hat{a}_j, \hat{a}_k^\dagger\right] = \delta_{jk}, \quad j, k \in \{H, V\}, \tag{3.4}$$

imply that the Stokes operator S_0 commutes with all the others

$$\left[S_0, S_j\right] = 0, \quad j \in \{x, y, z\}, \tag{3.5}$$

and that the other Stokes operators obey the SU(2) algebra commutation relations,

$$\left[S_j, S_k\right] = 2i\epsilon_{jkl} S_l, \quad j, k, l \in \{x, y, z\}. \tag{3.6}$$

It is convenient to write the polarisation squeezing condition in a form that is invariant under SU(2) transformations [LK06], similarly to the atomic case. To this purpose, we define the Stokes vector $\mathbf{S}$, whose Cartesian components are $\{S_x, S_y, S_z\}$: we call $S_\parallel$ its component along the mean polarisation $\langle \mathbf{S} \rangle$, while $\mathbf{S}_\perp$ is the component in the orthogonal plane.

If we define a polarisation coherent state as the product state of two coherent states in two orthogonal polarisation modes, e.g. $|\alpha_H\rangle \otimes |\alpha_V\rangle$, and use it to select the standard quantum limit, we obtain a definition for polarisation squeezing that resembles Eq. (3.1) [LK06]:

$$(\Delta \mathbf{S}_\perp)^2 \geqslant \langle S_0 \rangle. \tag{3.7}$$

For metrological applications, a definition that mimics the Wineland condition (3.2) is more convenient [LK06]:

$$\langle S_0 \rangle \frac{(\Delta S_\perp)^2}{|S_\parallel|^2} \geqslant 1. \tag{3.8}$$

3.2 SPIN SQUEEZING INEQUALITIES

In this Section we summarise the relationship between the SSIs in Eqs. (3.1) and (3.2) and entanglement of an atomic ensemble: a more detailed report about the relation between spin squeezing inequalities and entanglement can be found in [GT09].

The connection between the inequality (3.2) that defines spin squeezing and entanglement has been known since 2001, when Sørensen and his collaborators [SDCZ01] showed that, for a spin-$^1/_2$ atomic ensemble, squeezed states that satisfy the definition (3.2) are entangled. Similar results have been found for larger-spin systems, for other kinds of squeezing, and for multi-partite entanglement [VHET11, KCL05, KGL$^+$06, GT09]. Spin squeezing has been produced in a number of experiments [AWO$^+$09, LSSV10, GZN$^+$10, CBS$^+$11, SKN$^+$12, BvFB$^+$13, OSRT13, BCN$^+$14, MSL$^+$14]. However, to date, there has been no direct observation of the implied entanglement.

More details about the nature of the entanglement in spin squeezed states are added by Sørensen and Mølmer [SM01], who showed that spin squeezed states are k-entangled states [GTB05], which means that one needs k-partite entanglement to produce such a state. A more precise definition of k-entangled state is based on the concept of k-producible state [GTB05], i.e. a state with at least k particles entangled. More precisely, a pure k-producible state is defined as

$$|\psi^{(N)}_{k_{prod}}\rangle = \otimes_{\alpha=1}^{M_N} |\psi_\alpha^{(N_\alpha)}\rangle, \tag{3.9}$$

where $|\psi_\alpha^{(N_\alpha)}\rangle$ is a state with $N_\alpha \leqslant k$ particles, with $\sum_{\alpha=1}^{M_N} = N$. This definition can be extended to mixed states, so that in general a k-producible state can be written as

$$\rho^{(N)}_{k-prod} = \sum_l p_l |\psi^{(N)}_{k_l-prod}\rangle\langle\psi^{(N)}_{k_l-prod}|, \tag{3.10}$$

with $k_l \leqslant k$ for all l and $\sum_l p_l = 1$. A k-producible state that is not $(k-1)$-producible is what we called before a k-entangled state, which means that at least one of the terms in the convex sum above is an entangled state of k particles.

The work by Sørensen and Mølmer [SM01] shows that Eq. (3.2) is not only a tool for detecting entanglement in atomic systems: given that spin squeezed states are k-entangled, they show that the SSI (3.2) can be used to estimate the value of k, also known as *entanglement depth*. This is very useful, as it has been the only method used up to now to quantify the number of entangled particles in spin squeezed states: spin squeezing experiments [GZN$^+$10, BMCC$^+$14] have used SSIs to claim 500,000 entangled atoms and entanglement depth of 170.

3.2.1 *Optical spin squeezing inequality*

Some experiments [GZN$^+$10, BMCC$^+$14] have already demonstrated entanglement in a spin squeezed ensemble, a collective phenomenon, through measurements of the collective atomic spin. However, this is an indirect demonstration, based on the fact that the SSI (3.2) implies entanglement. A more direct demonstration of entanglement would involve measurements of the individual particles of the ensemble to reconstruct their state and show that the collective state is entangled. Current technology does not allow this approach for atoms. Nevertheless, this is possible for polarisation qubits, the natural analogous system of spin-$^1/_2$ atoms that we introduced in Sec. 3.1. For this reason, we aim to develop a SSI for photons to connect polarisation squeezing to entanglement.

Thanks to the work of Hyllus and coworkers [HPS10], who extended the results of [SM01] to systems with fluctuating number of particles, we can use Eq. (3.8), the photonic analogous of the SSI (3.2), to estimate the entanglement depth of a polarisation squeezed state. For realistic levels of squeezing, we predict large values of k ($k \approx 1000$) [MB14]. The same entanglement could be in principle demonstrated more directly by measuring the polarisation of individual photons with available photonic technologies [MB14], such as an array of single photon detectors. This is in principle feasible, but requires a large number of experimental resources.

With just few photon detectors, we can check directly with light another prediction that has been made for atoms: for symmetric spin systems, Wang and Sanders [WS03] considered symmetric spin systems and showed that squeezing implies entanglement in every reduced two-atom density matrix. Its experimental verification implies the reconstruction of the two-particle density matrix from individual measurements: while this is not possible yet for spin squeezing experiments, for photons there are already well-known techniques, such as photon counting and discrete quantum tomography, to recover the microscopic polarisation state from experimentally-accessible values.

Here we present a result analogous to that of Wang and Sanders, but for optical fields: we predict that any photon pair belonging to a state that features non-classical polarisation is entangled [BM13]. This is the first spin-squeezing-type inequality in the optical domain i.e., the first demonstration that optical continuous-variable (CV) non-classicality implies discrete variable (DV) entanglement. Production and detection of optical squeezing is a well-developed technology, with quadrature squeezing levels reaching 12.3 dB [MAE+11]. Simultaneously, efficient detection of photons is routine in quantum optics laboratories, as is quantum state tomography of entangled pairs [JKMW01, ASMS07]. Together, these offer the possibility to test the predicted relations between macroscopic squeezing and microscopic entanglement.

A simple non-classicality condition is found applying the Cauchy-Schwarz inequality to the second-order correlation function defined in Eq. (2.4). In fact, for classical fields, the field operators $\hat{a}_i(t)$ act like the c-numbers $\alpha_i(t)$, so that we can write

$$\begin{aligned}
\left|G^{(2)}_{HH,VV}(\tau)\right|^2 &= |\langle\, \alpha^*_H(t)\alpha^*_H(t+\tau)\alpha_V(t+\tau)\alpha_V(t)\,\rangle|^2 \\
&= |\langle\, \alpha^*_H(t)\alpha_V(t+\tau)\alpha^*_H(t+\tau)\alpha_V(t)\,\rangle|^2 \\
&\leqslant \langle\, \alpha^*_H(t)\alpha_V(t+\tau)\alpha^*_V(t+\tau)\alpha_H(t)\,\rangle\langle\, \alpha^*_V(t)\alpha_H(t+\tau)\alpha^*_H(t+\tau)\alpha_V(t)\,\rangle \\
&= \langle\, \alpha^*_H(t)\alpha^*_V(t+\tau)\alpha_V(t+\tau)\alpha_H(t)\,\rangle\langle\, \alpha^*_V(t)\alpha^*_H(t+\tau)\alpha_H(t+\tau)\alpha_V(t)\,\rangle \\
&= G^{(2)}_{HV,HV}(\tau)G^{(2)}_{VH,VH}(\tau) \qquad (3.11)
\end{aligned}$$

Acting in a similar way on $G^{(2)}_{HV,VH}(\tau)$, we obtain the two classical inequalities

$$\left|G^{(2)}_{HH,VV}(\tau)\right|^2 \leqslant G^{(2)}_{HV,HV}(\tau)G^{(2)}_{VH,VH}(\tau), \qquad (3.12a)$$

$$\left|G^{(2)}_{HV,VH}(\tau)\right|^2 \leqslant G^{(2)}_{HH,HH}(\tau)G^{(2)}_{VV,VV}(\tau). \qquad (3.12b)$$

The violation of at least one of these inequalities is thus a sufficient condition for nonclassicality.

The second-order correlation functions involved in the inequalities above become the elements of the two-photon observable density matrix $\mathbf{G}^{(2)}$ defined in Eq. (2.4) when divided by the common normalisation factor $\mathrm{Tr}[\mathbf{G}^{(2)}]$. For a two-qubit density matrix like $\mathcal{G}^{(2)}$, the Peres-Horodecki criterion [Per96, HHH96a] gives a necessary and sufficient condition for entanglement: the state is entangled if and only if the partial transpose of its density matrix is negative, i.e. if the matrix obtained by transposing only one qubit has some negative eigenvalue.

For states that are invariant under the transformation (2.15) or (2.16), as the ones we considered in Section 2.3, we obtain a simplified ODM where half of the elements are null:

$$\mathcal{G}^{(2)} \propto \begin{pmatrix} G^{(2)}_{HH,HH} & 0 & 0 & G^{(2)}_{HH,VV} \\ 0 & G^{(2)}_{HV,HV} & G^{(2)}_{HV,VH} & 0 \\ 0 & G^{(2)}_{VH,HV} & G^{(2)}_{VH,VH} & 0 \\ G^{(2)}_{VV,HH} & 0 & 0 & G^{(2)}_{VV,VV} \end{pmatrix}, \tag{3.13}$$

where all elements are functions of τ. This describes a mixture of a state in the $\{HH, VV\}$ subspace and another in $\{HV, VH\}$. Following from their definitions, and as required for the hermiticity of $\mathcal{G}^{(2)}$, we have $G^{(2)}_{VV,HH} = [G^{(2)}_{HH,VV}]^*$, and $G^{(2)}_{VH,HV} = [G^{(2)}_{HV,VH}]^*$. The partial transpose of the state in Eq. (3.13) is negative when at least one of the inequalities (3.12a) and (3.12b) is violated. The Peres-Horodecki criterion thus creates an equivalence between the violation of the inequalities (3.12a) and (3.12b) and pairwise entanglement for a class of states relevant for experimental quantum optics, i.e. the states that are invariant with respect to (2.15). Polarisation squeezed states, for example, belong to this class and violate the inequalities (3.12a) and (3.12b), as we will show in the next Section. Our result is thus analogous to the result of Wang and Sanders for symmetric atomic systems [WS03]: they show that satisfying inequality (3.1), the Kitagawa-Ueda condition for squeezing, implies pairwise entanglement and vice versa for relevant experimental implementations of spin squeezing.

3.3 POLARISATION SQUEEZING AND ENTANGLEMENT

Here we describe a feasible experimental scenario that violates the spin-squeezing-type inequalities (3.12) with available technologies.

Continuous wave (CW) non-classical polarisations have been produced by combining two bright squeezed beams with orthogonal polarisation [KLL+02, BTSL02], by optical self-rotation [RBL03] and by combining a coherent state (H-polarised) with V-polarised squeezed vacuum [PZCM08]. We consider the last case, where the squeezed vacuum is generated via a sub-threshold optical parametric oscillator (OPO), as described by Collett and Gardiner [CG84]: for this system, symmetry under the transformation (2.16) is assured by the associated Hamiltonian:

$$H = \hbar\omega_0 \hat{a}_V^\dagger \hat{a}_V + \frac{i\hbar}{2}\left[\epsilon\, e^{-i\omega_p t}(\hat{a}_V^\dagger)^2 - \epsilon^* e^{i\omega_p t}\,\hat{a}_V^2\right], \tag{3.14}$$

where ϵ is the nonlinear coupling, and ω_0 and ω_p are the frequency of the output and pump of the OPO, respectively.

We compute the two-photon ODM for the polarisation squeezed state obtained by combining the V-polarised output of a CW OPO with an H-polarised monochromatic coherent state $|\alpha\rangle$ with amplitude $\alpha \equiv e^{i\varphi_{CS}}\sqrt{\Phi_C}$. Here we report the results of the calculations, where we consider only stationary states. More details can be found in Appendix A. The field operator $\hat{a}_V$ is expressed via a Bogoliubov transformation of the vacuum input and loss reservoir operators $\hat{a}_1$ and $\hat{a}_2$, respectively

$$\hat{a}_V(\omega) = f_1(\omega)\,\hat{a}_1(\omega) + f_2(\omega)\,\hat{a}_1^\dagger(-\omega) + f_3(\omega)\,\hat{a}_2(\omega) + f_4(\omega)\,\hat{a}_2^\dagger(-\omega). \tag{3.15}$$

The coefficients

$$f_1(\omega) = \frac{1}{A(\omega)}\left[\eta^2 - \left(1-\eta-i\frac{\omega}{\delta\nu}\right)^2 + |\mu|^2\right] \tag{3.16}$$

$$f_2(\omega) = \frac{2\eta\mu}{A(\omega)} \tag{3.17}$$

$$f_3(\omega) = \frac{2\sqrt{\eta(1-\eta)}}{A(\omega)}\left(1-i\frac{\omega}{\delta\nu}\right) \tag{3.18}$$

$$f_4(\omega) = \frac{2\mu\sqrt{\eta(1-\eta)}}{A(\omega)} \tag{3.19}$$

$$A(\omega) = \left(1-i\frac{\omega}{\delta\nu}\right)^2 - |\mu|^2 \tag{3.20}$$

are functions of the experimental parameters of the OPO: the cavity FWHM bandwidth $\Gamma = \delta\nu/\pi$, and the cavity escape coefficient $\eta = T_1(T_1 - T_2)^{-1}$, i.e. the ratio between the transmission of the output coupler T_1 and the sum of both the intracavity losses T_2 and the transmission of the output coupler. The parameter $\mu = |\mu|e^{i\varphi_p}$ is the amplitude of the OPO pump, expressed in units of the OPO threshold power P_{th}, giving $|\mu|^2 = P_p/P_{th}$, where P_p is the OPO pump power.

The time-domain correlation functions required for the ODM can be computed as Fourier integrals, to find

$$\mathcal{G}^{(2)} = \begin{pmatrix} a & 0 & 0 & c \\ 0 & b & d & 0 \\ 0 & d & b & 0 \\ c^* & 0 & 0 & e \end{pmatrix}, \tag{3.21}$$

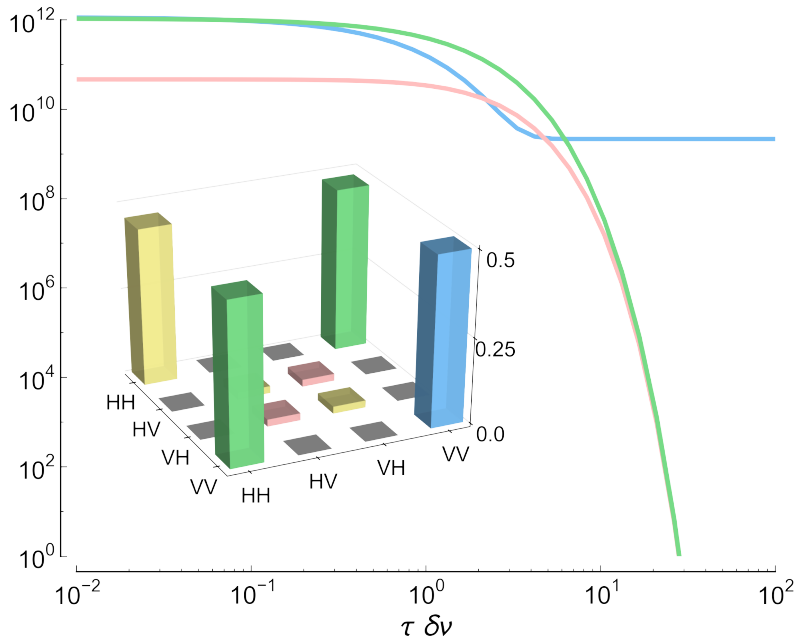

Figure 3.1: Elements of a typical two-photon ODM of a polarisation squeezed state as a function of the time interval between detection τ in units of the inverse OPO bandwidth $\delta\nu$. The colours of the lines match the one of the matrix elements of the $\mathcal{G}^{(2)}(1\text{ns})$ that is shown in the inset. The yellow matrix elements are not shown in the plot because they do not depend on τ. Fixed parameters: $\Phi_C = 10^6$ photons/s, $\Phi_S = 5 \times 10^4$ photons/s, $\delta\nu = 8.4\pi$ MHz, $\eta = 0.93$.

with

$$a = \quad G^{(2)}_{HH,HH} = {\Phi_C}^2 \tag{3.22a}$$

$$b = \quad G^{(2)}_{HV,HV} = \Phi_C\,\Phi_S, \tag{3.22b}$$

$$c = \quad G^{(2)}_{HH,VV}(\tau) = \Phi_C\Phi_S\left[\sinh(|\mu|x) + \frac{1}{|\mu|}\cosh(|\mu|x)\right] e^{i(\varphi_p - 2\varphi_{CS}) - x} \tag{3.22c}$$

$$d = \quad G^{(2)}_{HV,VH}(\tau) = \Phi_C\,\Phi_S\left[\frac{1}{|\mu|}\sinh(|\mu|x) + \cosh(|\mu|x)\right] e^{-x} \tag{3.22d}$$

$$e = \quad G^{(2)}_{VV,VV}(\tau) = {\Phi_S}^2\left\{1 + \frac{e^{-2x}}{|\mu|^2}\left[(1+|\mu|^2)\cosh(2|\mu|x) + 2|\mu|\sinh(2|\mu|x)\right]\right\} \tag{3.22e}$$

where $x = \delta\nu|\tau|$, and Φ_C and Φ_S are the photon fluxes of the coherent and of the squeezed vacuum state, respectively:

$$\Phi_C = G^{(1)}_{H,H}(0), \tag{3.23}$$

$$\Phi_S = G^{(1)}_{V,V}(0) = \frac{\mu^2\,\eta\,\delta\nu}{1-\mu^2}. \tag{3.24}$$

Note that a and b do not depend on the time interval τ between the detection of the two photons. The others depend exponentially on τ, so that they decrease rapidly when $\tau \gtrsim 1/\delta\nu$, as shown in Figure 3.1: the off-diagonal elements become null, while $G^{(2)}_{VV,VV}$ reaches a constant value corresponding to the rate of detecting two uncorrelated photons, i.e. the accidental counts rate. As a consequence, $\mathcal{G}^{(2)}$ becomes a diagonal matrix for $\tau \gtrsim 1/\delta\nu$, so we expect no entanglement for photons that are so separated in time.

We can now substitute the matrix elements into the inequalities (3.12a) and (3.12b) to check whether the polarisation squeezed state is entangled or not. While the second inequality, which takes the form

$$\left[\frac{1}{|\mu|}\sinh(|\mu|x) + \cosh(|\mu|x)\right]^2 e^{-2x} \leqslant 1, \tag{3.25}$$

is never violated, the first one, which can be written as

$$\left[\sinh(|\mu|x) + \frac{1}{|\mu|}\cosh(|\mu|x)\right]^2 e^{-2x} \leqslant 1, \tag{3.26}$$

is violated for each value of Φ_C and Φ_S when $x \ll 1$, i.e. when $|\tau| \ll 1/\delta\nu$. For large time separation between the photons, as expected, there is no entanglement independently of the values of Φ_C and Φ_S. Thus, for a polarisation squeezed state generated combining a coherent and a squeezed vacuum state, any two photons detected within a time interval sufficiently small are entangled.

3.3.1 *Entanglement under realistic conditions*

We now show that it is possible to achieve either high entanglement or high rates of entangled pairs with feasible experimental values.

We quantify the entanglement associated with a pair extracted from a polarisation squeezed state by means of the concurrence [Woo98]

$$\mathcal{C} = \max(0, \sqrt{\lambda_1} - \sqrt{\lambda_2} - \sqrt{\lambda_3} - \sqrt{\lambda_4})\,, \tag{3.27}$$

where λ_i are the eigenvalues of $\mathcal{G}^{(2)}(\tau)[\sigma_y \otimes \sigma_y][\mathcal{G}^{(2)}]^*[\sigma_y \otimes \sigma_y]$ in decreasing order and σ_y is a Pauli matrix. The relevant experimental parameters are the time interval τ between detections and the average photon fluxes of the coherent and squeezed state, Φ_C and Φ_S respectively. Changing

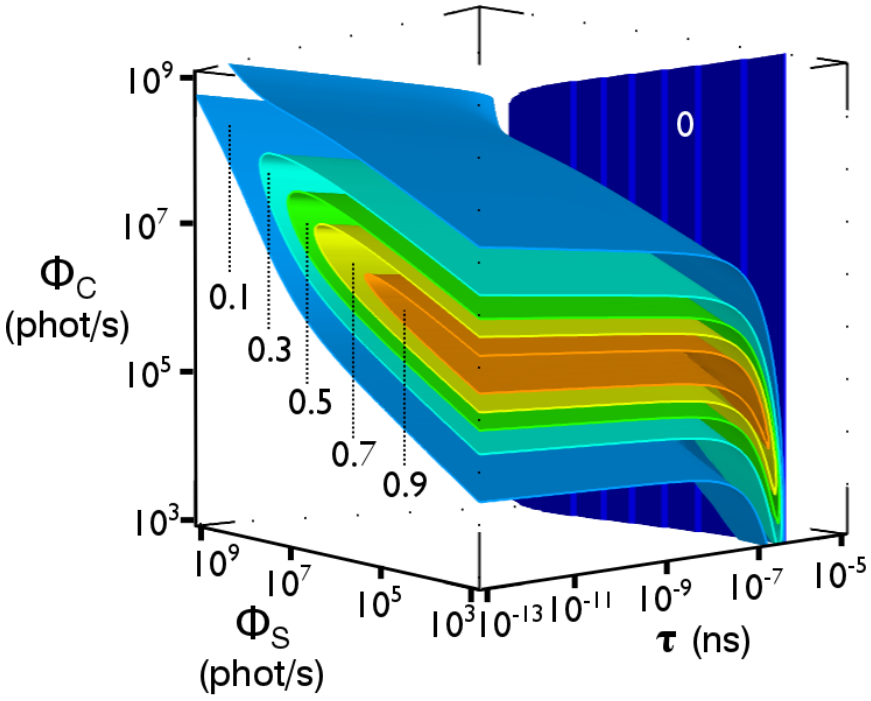

Figure 3.2: Entanglement of photon pairs within a polarisation-squeezed state that contains squeezed vacuum from a sub-threshold OPO and an orthogonally-polarised coherent state, as described in the text. Contours show concurrence $\mathcal{C}$ versus average photon fluxes in the coherent (Φ_C) and squeezed (Φ_S) beams, and versus time separation τ. Fixed experimental parameters: cavity linewidth $\delta\nu = 8.4\pi$ MHz and cavity escape coefficient $\eta = 0.93$.

the other parameters does not change significantly the concurrence, so we fix them to typical experimental values, specifically $\delta\nu = 8.4\pi$ MHz and $\eta = 0.93$, from [PZCM08]. Figure 3.2 shows that the state is entangled, i.e. it has $\mathcal{C} > 0$, provided that the two photons are detected within the coherence time of the squeezed state. As predicted, the concurrence goes to zero when $\tau \gtrsim 1/\delta\nu$. However, the concurrence does not change much in a wide range of time separations τ, which goes up to hundreds of nanoseconds ($\approx 1/\delta\nu$). The predicted ODM shows large concurrence, up to 100%, for pure squeezed vacuum (SV) with low squeezing. In these conditions, the concurrence is large for a region defined by

$$\Gamma\Phi_S \approx {\Phi_C}^2, \quad \Phi_S < \Gamma, \quad \tau\Gamma < 1. \tag{3.28}$$

Our results confirm that increasing the squeezing is detrimental to the pairwise entanglement, as observed for the atoms by Wang and Mølmer [WM02]. This happens because, similarly to the

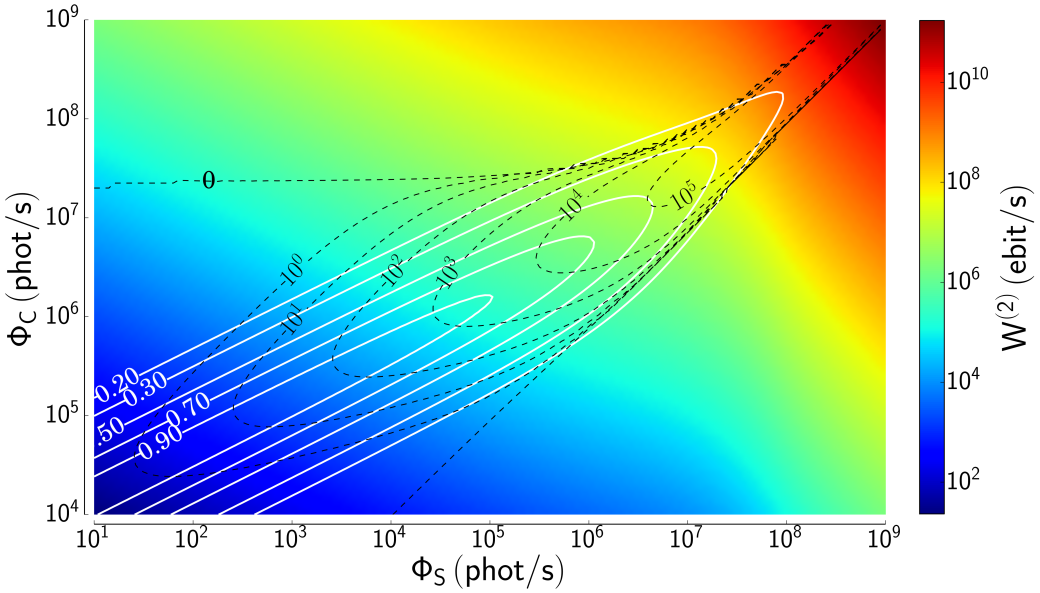

Figure 3.3: Total concurrence flux $W^{(2)}$ versus input fluxes Φ_C and Φ_S. Solid white contours show concurrence $\mathcal{C}$ for τ=1 ns. Dashed black contours show non-locality figure of merit β (see text) for $\Delta\tau$=1 ns.

atomic case, the entanglement depth grows as the squeezing increases, as we showed for single-mode polarisation squeezed states in [MB14]: because of the monogamy of entanglement [CKW00], the pairwise entanglement measured by concurrence decreases as the entanglement is shared by more and more particles.

We estimate the entangled pair flux by averaging the concurrence with the corresponding photon flux:

$$W^{(2)} = \int_{-\infty}^{+\infty} d\tau \, \mathrm{Tr}[\mathbf{G}^{(2)}(\tau)] \, \mathcal{C}(\tau), \tag{3.29}$$

and we plot it in Fig. 3.3 compared to concurrence: the experimental parameters Φ_C and Φ_S can be suitably chosen in order to obtain a Bell-like state with high concurrence ($\mathcal{C} \geqslant 0.9$ inside the innermost surface in Fig. 3.2).

However, there are some cases where high entanglement flux can be more important than maximal entanglement. For example, non-maximally entangled spin-1/2 states which violate a Bell

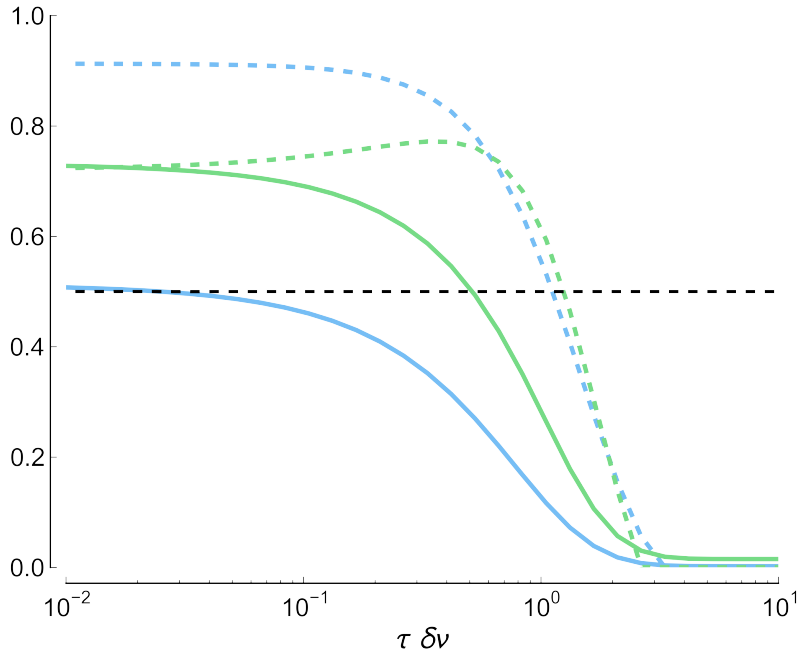

Figure 3.4: Concurrence (dashed lines) and $\mathcal{G}^{(2)}_{VV,VV}$ (solid lines) versus the time interval τ in units of the OPO bandwidth $\delta\nu$. The green lines are calculated for $\Phi_S = 1.5 \times 10^5$ photons/s, while the blue lines correspond to $\Phi_S = 5 \times 10^4$ photons/s. We observe maximum concurrence when $\mathcal{G}^{(2)}_{VV,VV}$ is near to the 0.5 level, marked by the dashed black line. Fixed parameters: $\delta\nu = 8.4\pi$ MHz, $\eta = 0.93$, $\Phi_C = 10^6$ photons/s.

inequality can be useful for teleportation [HHH96b]. A "typical" state satisfying these requirements

$$\mathcal{G}^{(2)}_{\text{typ}} \approx \begin{pmatrix} 0.436 & 0 & 0 & 0.472 \\ 0 & 0.044 & 0.044 & 0 \\ 0 & 0.044 & 0.044 & 0 \\ 0.472 & 0 & 0 & 0.520 \end{pmatrix}, \tag{3.30}$$

obtained with squeezed beam flux $\Phi_S = 2 \times 10^5$ photons/s (2.6% OPO threshold), coherent beam flux $\Phi_C = 2 \times 10^6$ photons/s and arrival-time difference $\tau = 1$ ns, can combine a high rate of entangled pairs with easily detectable concurrence. The state of Eq. (3.30) has $\mathcal{C} = 0.86$ and $W^{(2)} = 5 \times 10^5$ ebit/s, well above the 8×10^4 ebits/s that can be reached by states with high concurrence ($\mathcal{C} \geqslant 0.95$). Such a state can be used for teleportation with up to 96% fidelity [Hu13] and can be generated feasibly with current technology: in fact, it only needs 1.3 dB of squeezing, well within existing capabilities. The ability to trade brightness against entanglement purity may be advantageous also in applications of quantum non-locality. Hu [Hu13] calculates the achievable Clauser-Horne-Shimony-Holt inequality violation $\Delta s \equiv s - 2$ for states with the form of $\mathcal{G}^{(2)}$.

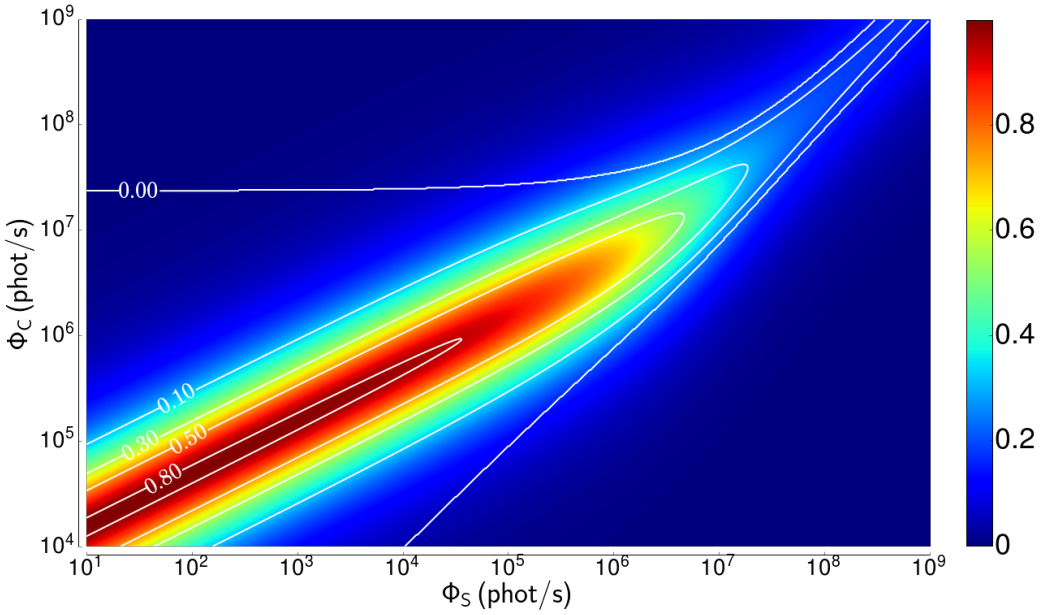

Figure 3.5: Concurrence as a function of photon fluxes Φ_C and Φ_S. The solid lines connect the points that violate the CHSH version of the Bell inequality of the same amount ΔS.

Fig. 3.5 shows that the largest violations of the inequality occur for the most entangled states, as expected. However, these states have a lower rate of photons as shown in Fig. 3.3, meaning that one needs longer measurements to obtain a violation that is statistically significant. Using the fact that statistical significance (in standard deviations) scales as $(T\Phi_{\Delta\tau})^{1/2}$, where T is the acquisition time and $\Phi_{\Delta\tau} \approx \mathrm{Tr}[\mathbf{G}^{(2)}(0)]\Delta\tau$ is the rate of detections within a coincidence window of width $\Delta\tau \ll \delta\nu^{-1}$, we find the figure of merit $\beta \equiv \Delta s^2 \Phi_{\Delta\tau}$ to describe how quickly a Bell inequality violation acquires statistical significance. As shown in Fig. 3.3, the largest values of β occur for bright, modestly-entangled states with $\mathcal{C} < 0.5$, and in some regions entanglement dilution (increasing Φ_C while keeping Φ_S constant) increases β.

Even though the polarisation squeezed state is a product of a frequency-entangled state (squeezed vacuum) and a classical one (coherent) with orthogonal polarisation, our result shows that the contribution of both initial states is fundamental for the pairwise entanglement of the final state. In fact, the maximum concurrence corresponds to the case that most resembles a Bell state, in which it is equally probable to detect two H-polarised or two V-polarised photons ($\mathcal{G}^{(2)}_{HH,HH}(\tau) \approx \mathcal{G}^{(2)}_{VV,VV}(\tau) \approx 0.5$), showing that the coherent state plays an important role in the generation of polarisation entangled pairs. In the previous Chapter, the quantity (2.18) that we measure for the wave-function reconstruction is the result of the interference between the two-photon component of the coherent and the V-polarised state: hence, the best condition for the measurement is when $G^{(2)}_{HH,HH}(\tau) \approx G^{(2)}_{VV,VV}(\tau)$, because the visibility of the interference is higher. Similarly, in this case, an equal contribution of HH and VV pairs leads to higher entanglement, as shown in Figure 3.4.

Moreover, as in the wavefunction reconstruction, a constant relative phase between the two polarisation components is fundamental for the experimental measurement. In fact, the only element that depends on the phase is $\mathcal{G}^{(2)}_{HH,VV}$: if the phase drifts on a time scale smaller than the measurement time scale, the measured value will be a null average, and this implies no entanglement, as (3.12a) cannot be violated when $G^{(2)}_{HH,VV} = 0$.

Part II

Experiment

4

EXPERIMENTAL SETUP

The previous Chapters describe two different theoretical results that can be demonstrated with the same experimental setup. The polarisation squeezed state, which is necessary to observe the entanglement described in Chapter 3, can be also used to test the reconstruction technique proposed in Chapter 2. In fact, the polarisation squeezed state is composed of a squeezed vacuum mode, which is a good approximation of a two-photon state in the low power limit, and by a coherent reference state in the orthogonal polarisation mode. By collecting statistics of photon pair arrivals for different polarisation bases, we obtain sufficient information to reconstruct completely the temporal two-photon wavefunction of the squeezed vacuum state. The same kind of measurement is at the basis of discrete quantum tomography [JKMW01], that gives us the observable density matrix of two photons extracted from the polarisation squeezed state, so that we can measure its entanglement and compare it to the results of Chapter 3.

This Chapter describes in detail the experimental setup (see Fig. 4.1) that allows us to demonstrate the theoretical results described in the previous Chapters. We illustrate the state generation and the measurement process, with particular attention to the techniques we employed for the stabilisation of the phase between the two orthogonal polarisation modes, which is crucial to observe the interference effect that is at the base of the results of Chapter 2, and the quantum coherences that are the proof of entanglement in a polarisation squeezed state, as predicted in Chapter 3.

4.1 STATE GENERATION

In this Section, we describe schematically how we generate the polarisation squeezed state that we use for the experiments described in the following Chapters. More details on the polarisation squeezing generation can be found in the PhD thesis of Ana Predojević [Pre09], who designed and built the system, shown in Figure 4.2. This is capable to generate up to 3.6 dB squeezing and has been used to improve the signal-to-noise ratio of an optical magnetometer [WCB+10].

The polarisation squeezed state that we described in Section 3.1 is composed of a coherent state (CS) and a squeezed vacuum (SV) state that share the same frequency and spatial mode, but that belong to orthogonal polarisation modes (see Fig. 4.3). While the H-polarised coherent state is simply laser light, we need a sub-threshold optical parametric oscillator (OPO) to generate the V-polarised squeezed vacuum. Our OPO is a type-I nonlinear crystal (a 10 mm long periodically

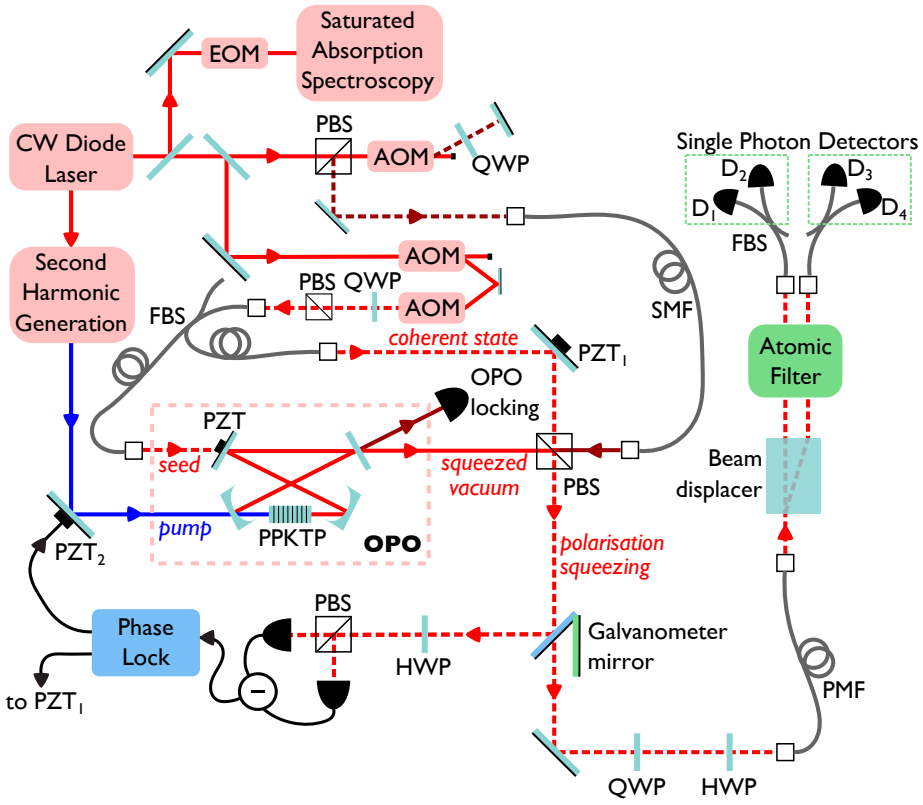

Figure 4.1: Full experimental setup. AOM: Acousto-optic modulator; EOM: electro-optic modulator; PBS: polarising beam splitter; QWP (HWP): quarter-(half-)wave plate; FBS: fibre beam splitter; PMF: polarisation maintaining fibre; SMF: single-mode fibre; PZT: piezo-electric actuator.

poled potassium titanyl phosphate - PPKTP) enclosed in a bow-tie optical cavity to enhance the downconversion process. Its output spectrum looks like a frequency comb with 8.4 MHz peaks, separated by a cavity free spectral range (FSR, 501 MHz). Their power is modulated by a $\approx$ 150 GHz FWHM envelope, given by the phase-matching of the nonlinear process in the crystal. Among these, only the degenerate mode, where the two down-converted photons have the same frequency, features the one-mode squeezing that characterises the squeezed vacuum state.

Polarisation squeezing appears only when the two polarisation components are at the same frequency and in the same spatial mode: we use an external-cavity diode laser (DL - Toptica TA-SHG 110) that provides both the 795 nm coherent beam and its second harmonic (397 nm), that serves as a pump for the OPO, so that the generated photon pairs are in the same frequency mode of the coherent state, but in a different spatial mode. We combine them in the same spatial mode by means of a polarisation beam splitter as in Fig. 4.3. To check and improve the mode matching, we take an additional beam (seed) at 795 nm from the same DL and we add it to the OPO as in Fig. 4.1

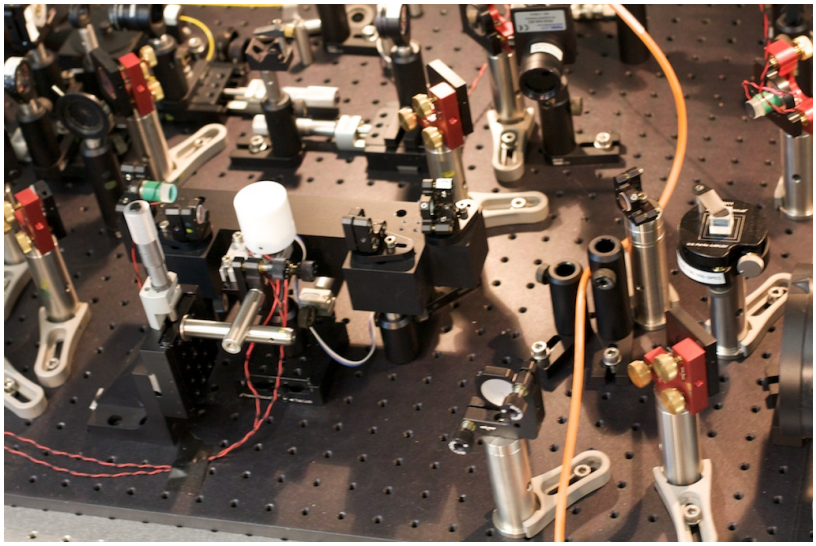

Figure 4.2: A photo of the optical parametric oscillator with the polarisation beam splitter (on the right) that allows us to combine in the same spatial mode the two polarisation components of the polarisation squeezed state.

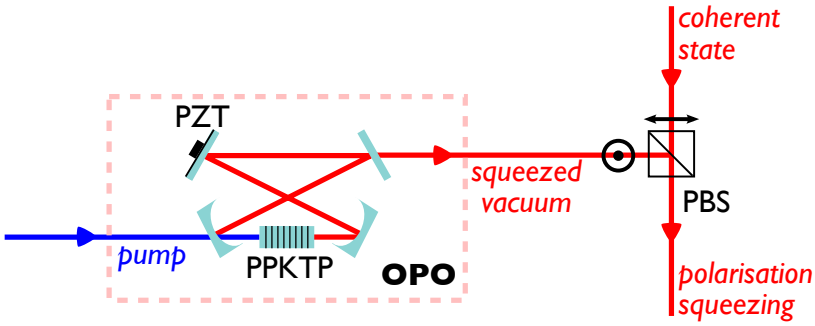

Figure 4.3: Schematic setup for the generation of a polarisation squeezed state.

to have a seeded interaction in the crystal. We then maximise the visibility (98%) of the interference fringes between the coherent state and the OPO output. We use this same DL to generate all the additional beams used in the experiments.

We use a modified Pound-Drever-Hall (PDH) technique [Bla01] to stabilise the length of the OPO cavity. The laser is current-modulated, and thus frequency-modulated, at 20 MHz, as required by the PDH technique. One of the outputs of the laser at 795 nm is used as locking beam and passes through a double-pass acousto-optic modulator (AOM) that adds an adjustable offset ($\approx$ 630 MHz) to its frequency, to make it resonant to a higher order transverse mode of the cavity with H polarisation, orthogonal to the OPO output. As shown in Fig. 4.1, this beam enters counter-propagating to the squeezed vacuum. This allows us to stabilise the cavity with very little contamination of the squeezed vacuum by the locking beam, which is simultaneously at a different frequency, polarisation, spatial mode, and direction of propagation. The nonlinear crystal is birefringent, which implies that the cavity resonates at different frequencies for orthogonal polarisation modes. We adjust the locking-beam frequency to make the cavity resonate simultaneously for both the squeezed vacuum and the locking-beam modes. We use then the error signal given by the locking beam to stabilise the cavity length, to keep the cavity resonant to the squeezed vacuum mode.

This setup was designed to operate at maximum nonlinear gain to obtain as large squeezing as possible [PZCM08, WCB$^+$10]: this forced us to realign thoroughly the whole setup to adapt it to the new pump power regime required by the experiments described in the following Chapters. We need to reduce the pump power by more than 90%, so that the squeezed vacuum state can be approximated by a state with no more than two photon, allowing the complete reconstruction of its temporal wavefunction and at the same time maximising the spin-squeezing-like entanglement. A reduction in the OPO pump power causes a reduction of the thermal lensing effect in the crystal that was observed in previous experiments [Pre09]: as a consequence, a dramatic change of pump power modifies significantly the cavity mode, and then all the alignment of the beams entering and exiting the cavity, so that we had to optimise all the polarisation squeezing setup to adapt it to the new pump power regime.

4.2 MEASUREMENT

After generating the polarisation squeezed state, we collect information about the arrival time and the polarisation of photon pairs belonging to it with a polarimeter like the one sketched in Fig. 2.1, modified as in Fig. 4.4 so that we can measure also the photon pairs that share the same polarisation. The data that we collect in this way are simply related to second-order correlation functions, as shown in Section 2.2. This allows us to check all the theoretical predictions of the previous Chapters with this simple detection setup.

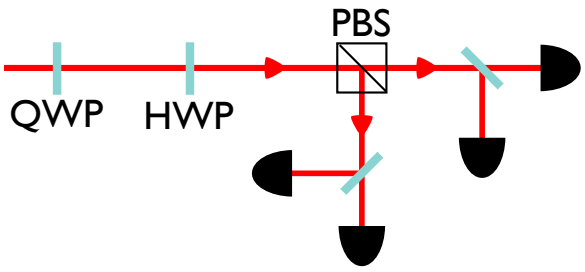

Figure 4.4: Polarimeter detection setup.

4.2.1 *Single-Photon Detectors*

We use a Perkin Elmer SPCM-AQ4C single-photon counting module, containing four fiber-connected avalanche photodetectors with a dark count rate that amounts to 500 counts/s and ≈ 0.5 quantum efficiency at 795 nm. This detectors have the same or higher quantum efficiency for a wide region of the spectrum that goes from 550 nm up to 800 nm: this prevents us from distinguishing the polarisation squeezed state from the other frequency modes in the OPO output spectrum (separated by multiples of the 501 MHz FSR). The hundreds of nondegenerate modes could then mask the contribution of the squeezed vacuum state, unless we block them. For this purpose, we designed a Faraday Anomalous Dispersion Optical Filter (FADOF) with high rejection outside its narrowband transmission window, described in detail in [ZANW12].

4.2.2 *Narrowband atomic filter*

The filter is composed of a hot rubidium cell between two crossed polarisers (see Fig.4.5). A coil wrapped around the cell generates a magnetic field that induces polarisation rotation via Faraday effect: we tune the temperature (365 K) and the magnetic field intensity (4.5 mT) so that the light around the frequency ω_0, at 2.7 GHz to the red of the Rb D_1 line centre, gets rotated by 90°, getting to pass through the final polariser. Conversely, this blocks non-resonant light that does not get rotated, while resonant light gets absorbed. This leads to a very narrowband transmission window (223 MHz HWHM) that selects the degenerate OPO output mode and rejects all the others, which are at least one FSR away. With few simple modifications, we adapt the filter to work for two orthogonal polarisations at a time, as in Fig. 4.6 and Fig. **??**: instead of two crossed polarisers, we use a beam displacer at the input to separate the two polarisation components into two parallel paths and a Wollaston prism after the cell to separate the rotated from the unrotated light. In this configuration, we characterise the filter when applied to photon pair counting [ZBLM14]. The transmission spectrum shown in Fig. 4.8 presents some secondary transmission peaks that are asymmetric with respect to the main peak: however, even if some photons belonging to non-degenerate modes can pass through the filter, their twin photons are blocked, reducing to 2% the probability of detecting a photon pair with the wrong frequency. We check experimentally that

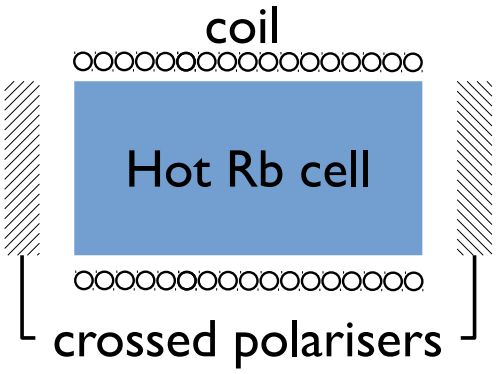

Figure 4.5: Schematic setup of the FADOF.

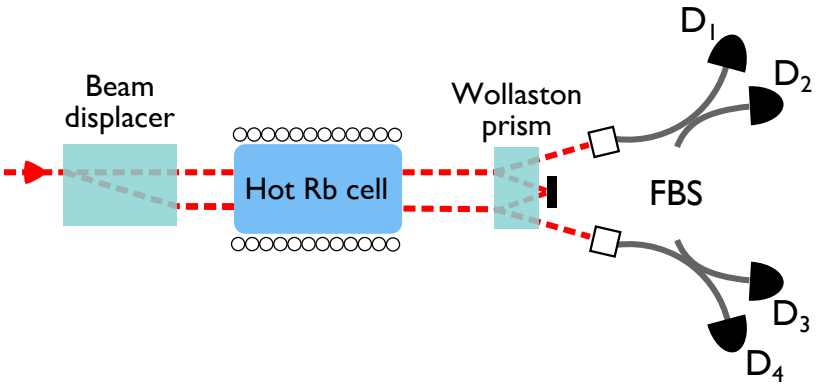

Figure 4.6: FADOF setup adapted to work for two linear polarisation modes.

98% of the pairs transmitted by the FADOF are resonant to rubidium, i.e. absorbed by a rubidium cell with high optical density, meaning that 96% of the transmitted pairs are indeed in a one-mode squeezed state.

For best efficiency, the diode laser must work at ω_0, the maximum transmission frequency of the FADOF, where there is no atomic line to take as a reference. Hence, we use an electro-optic modulator (EOM - Photline NIR-MPX800-LN05) in order to apply 960 MHz sidebands to a portion of the DL output, and lock the laser frequency to the lower sideband of the crossover line of the $F = 2 \rightarrow F'$ transition of the D_1 line of ^{85}Rb using saturated absorption spectroscopy.

4.2.3 *Time-of-flight counter*

Each filtered beam is coupled into a balanced fibre beam splitter that leads the photons to the single-photon detectors. These are connected to a digital time-of-flight counter (TOFC - FAST ComTec P7888) that records the photon arrival times for each detector with 2 ns resolution (1 ns if

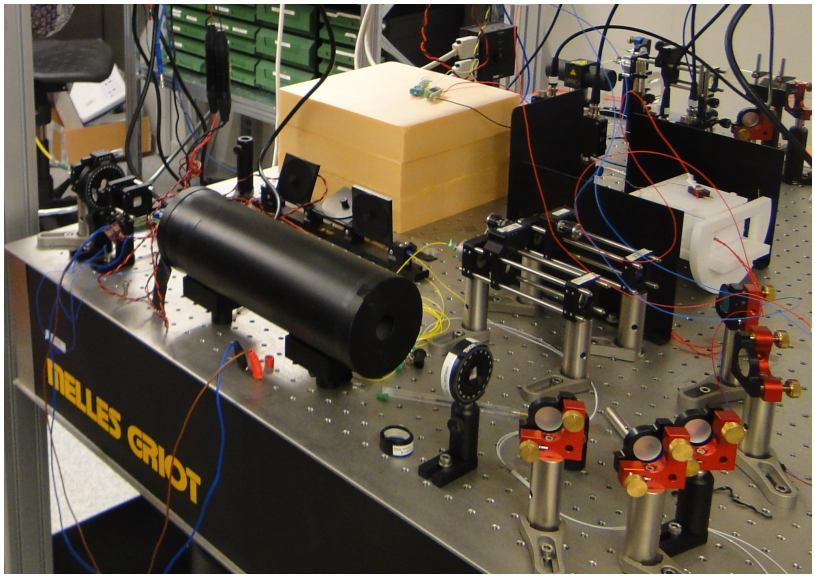

Figure 4.7: Photo of the final configuration of the FADOF setup.

only two detectors are used) and then saves them to a file. The memory buffer of the digital counter has a limited size, which means that the time stamps in each file correspond to a total of some hundreds of milliseconds for the photon rates used during the experiment. The overhead time that the digital counter needs to empty its memory buffer and save its content in a file, before starting again to collect data, takes about one second, meaning that data are acquired with a duty cycle of roughly 30%. As a consequence, we need hour-long measurements to collect sufficient statistics, despite having coincidence rates on the order of 10 pairs/s with a coincidence window of 4 ns.

4.2.4 *Polarisation maintaining fiber*

In the experiment, the polarising beam splitter in Fig. 4.4 is replaced by a polarisation maintaining fibre (PMF). We measured the extinction ratio of the PMF fiber: the low value (-53 dB) that we found ensures that the crosstalk between orthogonal polarisation modes in the fibre does not affect our measurements. We also calibrate the waveplates with reference to the PMF axes, so that their rotation angle is zero when the H polarisation matches the direction of the fast axis of the PMF.

4.3 STABILISATION

Both the wavefunction reconstruction technique and the entanglement detection in the polarisation squeezing rely on the two-photon interference between the two orthogonal polarisation components. It is crucial, then, from an experimental point of view, that the optical phase between the H- and V-

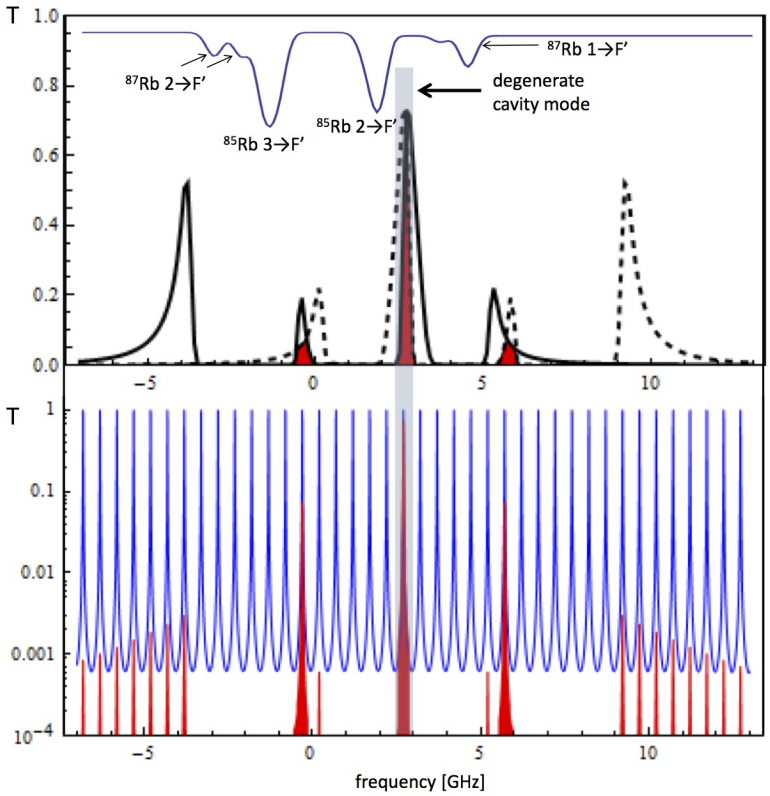

Figure 4.8: Upper plot: filter spectrum (black) and a mirrored filter spectrum with respect to the degenerate cavity mode (black dashed). Red shaded regions indicate transmission of correlated photon pairs. The blue line on the top represents the Rubidium absorption spectrum for comparison. Lower plot: cavity output spectrum (blue) and FADOF-filtered cavity spectrum (red). The degenerate cavity mode coincides with the FADOF peak. Both figures have the same frequency scale. Picture by Joanna Zielińska.

polarised beams is kept constant while measuring. Here we present the two methods we developed to stabilise the optical phase.

4.3.1 *Quantum noise lock*

For a polarisation squeezed state, the simplest way to monitor the phase between its polarisation components is to measure the variance of the squeezed Stokes operator, $(\Delta S_y)^2$, that varies depending on the relative phase $\varphi \equiv 2\varphi_{CS} - \varphi_p$ between the coherent (CS) state and the OPO pump (p) [PZCM08], so that it can be used as an error signal for a PID-type feedback [MMG+05].

We measure the Stokes operator with a setup like the one in Fig. 4.9: a half-wave plate set at 22.5° followed by a polarising beam splitter splits the state into two equally intense beams, which are focused on the photodiodes of a balanced detector (Thorlabs PDB150A), whose output current I_- is proportional to the difference of the currents of the two photodiodes and thus to the Stokes operator S_y [KLL+02]. We adjust finely the rotation angle of the waveplate, so that the polarisation squeezed state is equally split between the two detectors, so that $\langle I_- \rangle \propto \langle S_y \rangle = 0$. A multiplier circuit squares the differential signal giving I_-^2, so that — after passing through a low-pass filter — the resulting electronic signal is proportional to $\langle I_-^2 \rangle \propto (\Delta S_y)^2 = \langle S_y^2 \rangle - \langle S_y \rangle^2 \propto A + B\cos(\varphi)$ (see Eq. (A.8)) and can be used as an error signal for the active stabilisation of the phase φ.

We design an electronic system composed of frequency filters and amplifiers to clean and amplify the error signal (see Fig. 4.9). First of all, we set the balanced detector gain to the maximum gain setting that allows for shot-noise-limited measurements, i.e. 10^6 gain, corresponding to a 300 kHz bandwidth. In this way, we do not measure the whole squeezing spectrum, whose bandwidth is set by the width of the OPO peaks (8.4 MHz): however, the limited bandwidth of the detector has just the effect to discard the high frequency range, which is associated to lower squeezing, as shown in Fig. A.1. The selected bandwidth is reduced from the other side by a RC high-pass filter (390 kHz cutoff frequency), that removes the 1/f noise from the signal coming from the detector. The final signal has a very narrow bandwidth around a center frequency that is approximately 400 kHz. A low-noise amplifier (Femto DHPVA) with 60 dB gain and 10 MHz bandwidth amplifies the signal before the multiplier circuit. The multiplier circuit is a homemade circuit based on a Analog Devices AD835, with low-pass filters at the input and at the output with cutoff frequencies of 10 MHz and 30 MHz, respectively. We use a low pass filter with 1 MHz cutoff frequency (the DC port of a Mini-Circuits ZFBT-4R2GW+ Bias-Tee) to eliminate high frequency noise at the output of the multiplier. The phase drifts in the system are slow, on the scale of some seconds, so we add a 3 Hz cutoff low-pass filter with a low-noise preamplifier (SRS SR560) that provides additional gain. The offset given by the homemade multiplier circuit is compensated by subtracting from it a constant voltage signal (adjusted with a voltage divider) at the input of the pre-amplifier.

The electronic system described above mimics the behaviour of a spectrum analyser, which is the usual instrument to measure squeezing, as in [WCB+10]. Our experiments require a low level of squeezing (<0.5 dB) in order to maximise the two-photon contributions; for the same reason, the power of the coherent beam, which plays the role of the local oscillator in a homodyne detection, is

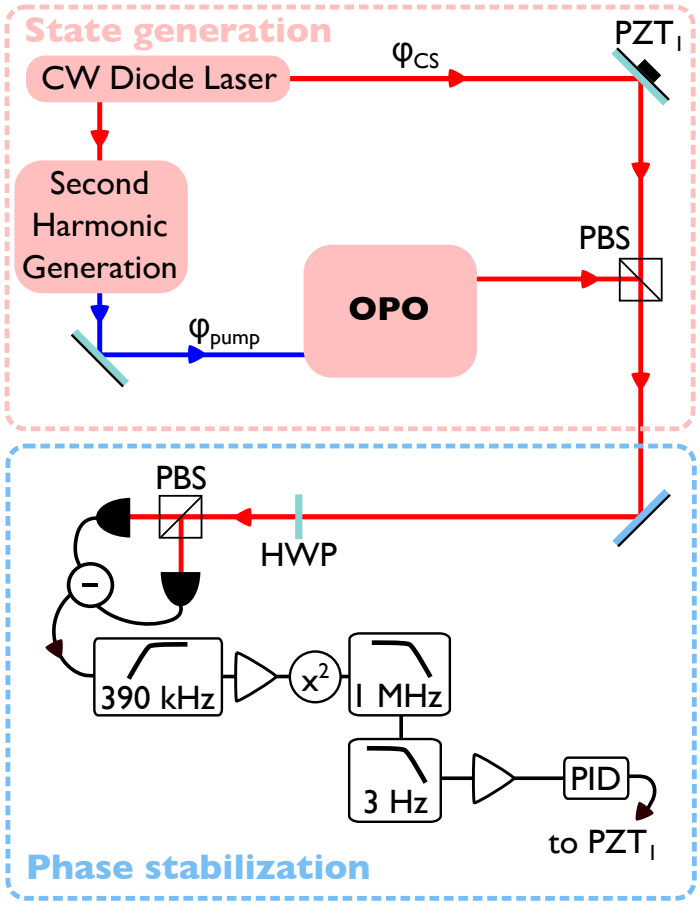

Figure 4.9: Quantum noise lock schematic setup. PID: Proportional-Integral-Derivative controller for feedback loop.

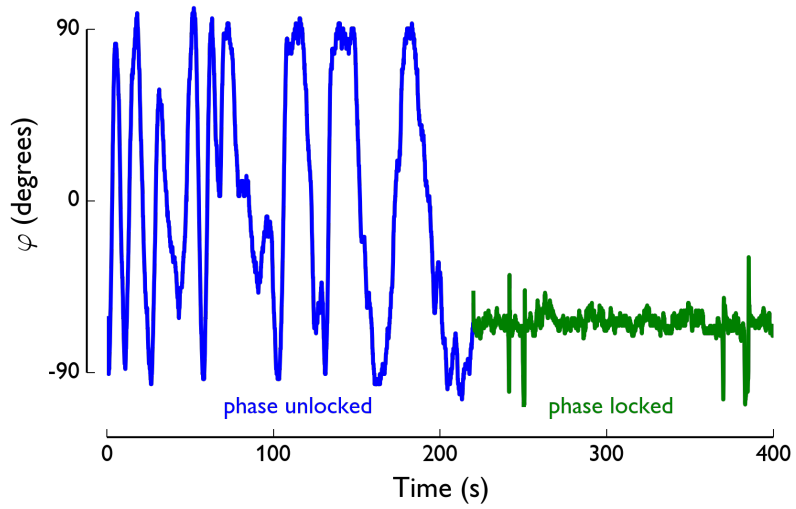

Figure 4.10: Error signal for the quantum noise lock. We record the error signal without acting on the PZT (blue line) and while locking the phase (green line).

limited to be at maximum some mW. This explains why we need to opt for larger gain instead of larger bandwidth in the balanced detector settings: the 5 MHz bandwidth option combined with the associated gain is not shot-noise limited with this CS power.

We check that the electronic setup described above gives a signal that varies with the phase φ: we change the relative optical phase by moving a mirror in the CS beam path mounted on a piezoelectric actuator (PZT_1) driven with a periodical slow signal (a few Hz). We obtain an oscillatory signal that is present only when the OPO pump is on and whose period changes as we change the driving frequency of PZT_1, proving that the error signal we obtain is actually depending on φ.

We record the error signal without acting on PZT_1 (blue line in Fig. 4.10), confirming the temporal scale of phase fluctuations. From the root mean square of this signal, we can estimate the amplitude of the free oscillations. This measurement is also a calibration that allows us to transform voltage variation in the error signal to phase changes: we know that $\langle I_-^2 \rangle \propto A + B\cos(\varphi)$, so that the amplitude of the oscillations corresponds to a change of 90°. The experiments require a constant phase, but its exact value is not important, so we can apply a side-of-fringe locking to our error signal. We use a FPGA-based PID controller that applies a feedback on PZT_1 to maintain the phase stable for hours with a root mean square deviation of 8°, as in the green line of Fig. 4.10.

This noise lock setup was used to stabilise the phase in the experiments presented in Chapters 5 and 6.

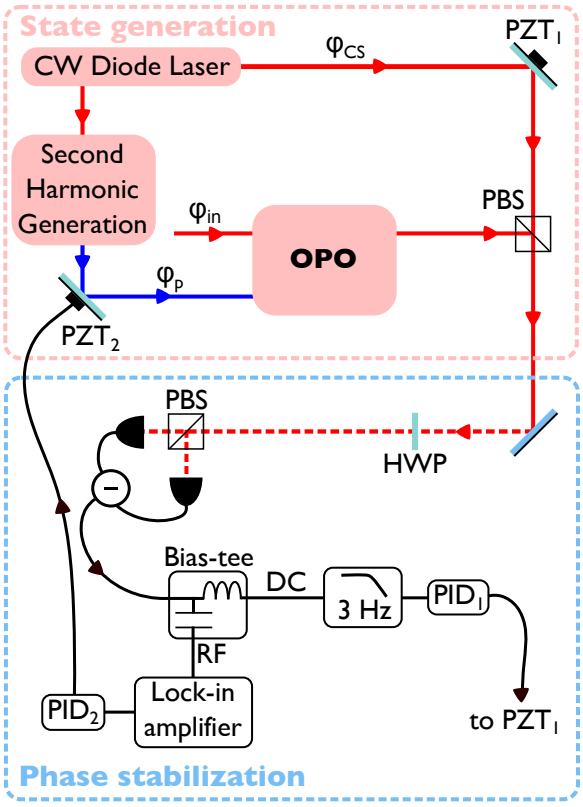

Figure 4.11: Classical noise lock schematic setup.

4.3.2 *Classical phase lock*

We designed an alternative phase locking technique based on the one used in [BLB+01], shown in Fig. 4.11. It is apparently more complicated from the technical point of view, as it requires an additional beam and a two feedback loops, but it has the large advantage of dealing with classical signals, which are larger and thus less sensitive to the noise in the system.

For the detection part, we use the same optical setup that we described in the previous section: the half-wave plate at 22.5° and the polarising beam splitter act as a balanced beam splitter so that the amplitude of the field hitting detector 1 or 2 is

$$\alpha_1 = \frac{1}{\sqrt{2}}(\alpha_{CS} + \alpha_{out}), \qquad \alpha_2 = \frac{1}{\sqrt{2}}(\alpha_{CS} - \alpha_{out}), \tag{4.1}$$

where α_{CS} and α_{out} are the field amplitudes of the coherent state and of the OPO output. The signal of the balanced detector is then proportional to

$$I_- \propto \alpha_1^*\alpha_1 - \alpha_2^*\alpha_2 = 2\mathrm{Re}\,[\alpha_{CS}\alpha_{out}^*] = 2\,[x_{CS}x_{out} + p_{CS}p_{out}], \tag{4.2}$$

where $x_j \equiv \mathrm{Re}[\alpha_j]$ and $p_j \equiv \mathrm{Im}[\alpha_j]$. Classical nonlinear optics describes the OPO output when we feed it with an input beam at 795 nm, together with the already mentioned 397 nm pump. The additional beam $\alpha_{in} = |\alpha_{in}|e^{i\varphi_{in}}$ acts as a seed for the nonlinear interaction in the crystal, so that the OPO output is proportional to:

$$\alpha_{out} \propto |\alpha_{in}| \left[e^{i\varphi_{in}} + |\mu| e^{i(\varphi_p - \varphi_{in})} \right], \tag{4.3}$$

where φ_p is the optical phase of the pump beam and $\mu = |\mu|e^{i\varphi_p}$ as in Section 3.3. This expression and its derivation can be found in Appendix B.3 in [Pre09], for example.

The difference current thus takes the form

$$I_- \propto 2\,|\alpha_{CS}\alpha_{in}|\,[\cos(\varphi_{CS} - \varphi_{in}) + |\mu|\cos(\varphi_{CS} - \varphi_p + \varphi_{in})]\,. \tag{4.4}$$

The pump power P_p that we use for the experiments is the 0.4% of the power threshold P_{th} for our OPO, so that $|\mu| = (P_p/P_{th})^{1/2} = 0.07$. As the second term in Eq. (4.4) is negligible, we can assume that I_- varies just with $\varphi_{CS} - \varphi_{in}$, which is the phase of the seed beam relative to the coherent state, so that I_- can be used as an error signal to stabilise $\varphi_{CS} - \varphi_{in}$.

Once we fix $\varphi_{CS} - \varphi_{in} = k$, we modulate the pump phase by moving a mirror mounted on a piezo-electric actuator (PZT_2) in the pump path with a frequency Ω_p and demodulate the signal coming from the detector by multiplying it by a sinusoidal wave with frequency Ω_p, to obtain

$$I'_- = \frac{\partial I_-}{\partial \varphi_p} \propto -2|\mu\alpha_{CS}\alpha_{in}|\sin(\varphi_{CS} - \varphi_p + \varphi_{in}) \tag{4.5}$$

$$= -2|\mu\alpha_{CS}\alpha_{in}|\sin(2\varphi_{CS} - \varphi_p + k), \tag{4.6}$$

which can be used to keep the difference $2\varphi_{CS} - \varphi_p$ constant. The two stabilisation processes together keep the pump phase stable relative to the coherent beam one.

The same signal I_- is necessary to lock both $\varphi_{CS} - \varphi_{in}$ and $2\varphi_{CS} - \varphi_p$, but the information for the first lock is in the low-frequency (DC) part, while the second lock needs the high-frequency (RF) part. In order to separate them efficiently, we use a commercial bias-tee, a Mini-Circuits ZFBT-4R2GW+, that has 100 kHz cutoff frequency for the RF port. Such high cutoff frequency is useful to eliminate effectively the signal modulation at ≈ 100 Hz that we apply to synchronise data acquisition to the stabilisation, as we explain in the following Section. As the PZT we had already in the setup is designed to work at a few kHz, we choose the lowest value of Ω_p that can pass through the RF port of the bias tee and give a clear error signal, which in our case is $\Omega_p = 50$ kHz. As the phase drifts are on the seconds scale, we can erase the contribution of higher frequencies to the DC part by applying a low-pass filter (3 Hz cutoff frequency) and then amplify the resulting signal with a low-noise preamplifier (SRS SR560): the error signal thus obtained is used to apply active feedback on PZT_1. The lock-in amplifier (SRS SR830 DSP) both generates the Ω_p signal that drives PZT_2 to modulate the phase φ_p and demodulates, amplifies and integrates the RF part of the signal with a low-pass filter (100 ms time constant), giving the error signal for the second lock.

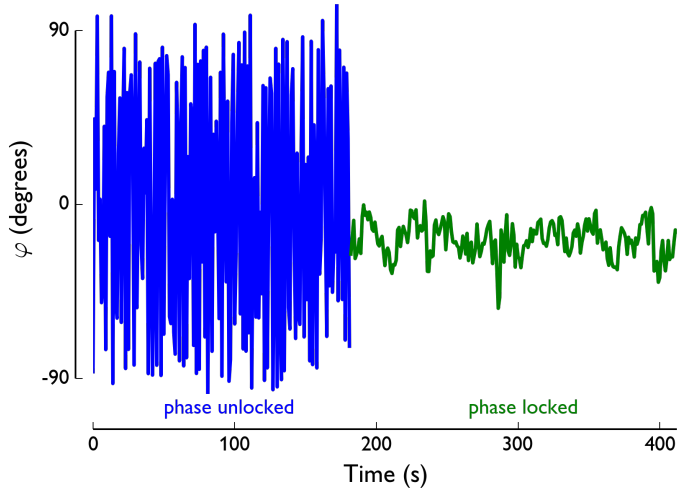

Figure 4.12: Error signal for the stabilisation of $\varphi = 2\varphi_{CS} - \varphi_p$ while $\varphi_{CS} - \varphi_{in}$ is kept stable. We record the error signal while driving PZT_2 with a regular oscillation (blue line) to calibrate the phase variations as described in Section 4.3.1. The green line is the same signal while we apply active feedback to the PZT_2 to stabilise $2\varphi_{CS} - \varphi_p$.

Another Mini-Circuits ZFBT-4R2GW+ Bias-Tee allows us to mix the (slow) feedback signal to the (fast) modulation, so that we can modulate φ_p while stabilising it relatively to φ_{CS}.

We check that the system responds to slow phase fluctuations in the system by slowly driving PZT_2 with a periodic oscillation and check if this appears in the error signal. This double classical lock relies on more intense signals than the quantum noise lock, so it is independent from any variation of the background noise levels in the system.

We use the same FPGA system we used for the quantum lock to implement the PID feedback loop and we use side-of-fringe locking to keep both phases stable. This stabilisation method keeps the relative phase between the polarisation components stable for hours with a RMS fluctuation of 6° (see Fig. 4.12), allowing us to perform the last experiment, presented in Chapter 7.

4.4 SYNCHRONISATION

Both lock techniques presented in the previous paragraphs need a beam with a coherent state in the H-polarised mode and the OPO output in the other, which is the same signal we need to measure with single photon detectors to prove the results of Chapters 2 and 3. If we used the quantum noise lock, we could not use a beam splitter to lock while measuring, because the vacuum entering through the empty port of the beam splitter would reduce the squeezing, preventing us from obtaining a clear error signal. On the other hand, for the classical phase lock, simultaneous phase lock and measurement is made impossible by the presence of the seed beam.

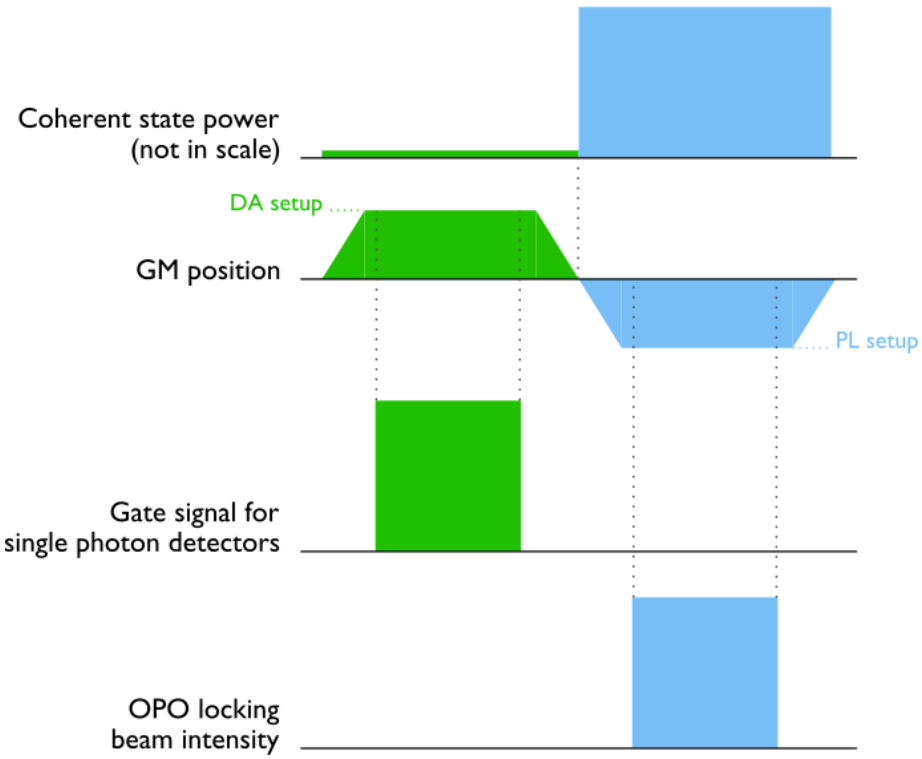

Figure 4.13: Schematic representation of the synchronisation of the various elements of the experiment.

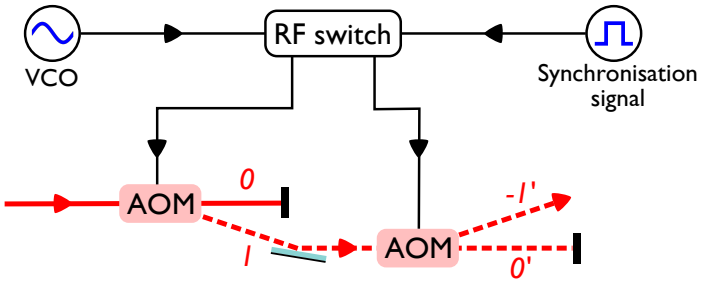

Figure 4.14: Double AOM setup for chopping the coherent state and seed beams. VCO: Voltage Controlled Oscillator.

Our solution to this problem is to use a galvanometer mirror (GM - Thorlabs GVS001) to send the beam alternately to the data acquisition (DA) setup and to the phase locking (PL) one. We synchronise all the elements in the system to the movements of the GM, as shown in Fig. 4.13.

During the DA, we need a low power CS beam, so that its rate of measured photon pairs is similar to the one of the squeezed vacuum state, to enhance the two-photon interference effects. At the same time, we need to switch off the seed beam and the counter-propagating beam that we use to lock the OPO length in order to reduce the background photons as much as possible. We chop them by turning on and off the RF signal that drives the acoustic wave in an AOM setup: RF switches (Mini-Circuits ZASWA-2-50DR+) control when the RF signals reach the AOMs. As we can see in Fig. 4.1, the OPO locking beam is chopped by using the same AOM that shifts its frequency. However, some photons from the OPO locking beam can reach the single photon detectors, contributing to the measurement background. For the seed beam and the coherent state we designed a setup with two AOMs (for more details, see Fig. 4.14 and [dIA15]) that chops the light without changing its frequency: the first-order output of the first AOM is shifted by 80 MHz and then fed into a similar AOM, so that its -1 order has the same frequency as the beam before the two AOMs. A fiber beam splitter splits the final beam, so that, during the PL, when the RF switch is on, we obtain a seed beam and a coherent state with the power required for the phase stabilisation (some mW). When the RF switch is off (DA), some pW of light manage to pass through the AOMs due to imperfections in the system. This is the right order of magnitude for the CS power to observe two-photon effects: the rotation of a half-wave plate followed by a polarising beam splitter tunes the CS power to match the rate of photon pairs coming from the CS to that recorded for the SV. During the DA, also the seed beam is very weak and has no observable effect, due to the very low transmission of the cavity mirror.

As we mentioned earlier, the OPO locking beam is absent during the DA, so that during that interval the OPO length cannot be locked. We drive the galvanometer mirror at the maximum frequency ($\approx$ 90 Hz) allowed for the large angle (12.5°) that it spans, so that the OPO length remains stable during the data acquisition.

As an additional measure against undesired background photons, we record the photon arrival times only during the DA phase by gating the electronic signal coming from the SPCM: we connect

the output of each detector with an AND logic circuit that selects only the events within the temporal gate synchronised with the movement of the galvanometer mirror.

5

TWO-PHOTON INTERFERENCE

Both the theoretical proposals presented in Chapters 2 and 3 require a stable phase between the two polarisation components. The observation of interference between the H- and V-polarised photons proves the phase stability and it is thus an important step forward towards the experimental verification of those theoretical results.

In this Chapter we explain how we observe two-photon interference by using the setup described in the previous Chapter and discuss our results, demonstrating the feasibility of the experiments proposed in the first two Chapters.

5.1 TWO-PHOTON INTERFERENCE

The effects of this two-photon interference are visible as oscillations in the coincident detection rate in a polarimeter setup like the one in Figure 2.1. The rate of pair detection for a polarisation squeezed state ρ_{PS} that is a product state of a H-polarised coherent state and of a V-polarised squeezed vacuum state is:

$$R^{(2)}_{PS}(\bar{\tau}) = \int_{\bar{\tau}-\Delta\tau/2}^{\bar{\tau}+\Delta\tau/2} \langle\, \hat{a}^{\dagger}_{A}(t)\hat{a}^{\dagger}_{B}(t+\tau)\hat{a}_{B}(t+\tau)\hat{a}_{A}(t)\,\rangle d\tau \tag{5.1}$$

By substituting the waveplates transformations (2.10) and (2.11) into the previous expression, we obtain:

$$\begin{aligned} R^{(2)}_{PS}(\bar{\tau}) = {} & \sin^2\theta\cos^2\theta\left[R^{(2)}_{HH,HH}(\bar{\tau}) + R^{(2)}_{VV,VV}(\bar{\tau})\right] \\ & - e^{-2i\phi}\sin^2\theta\cos^2\theta\left[R^{(2)}_{HH,VV}(\bar{\tau}) + R^{(2)}_{VV,HH}(\bar{\tau})\right] + \\ & + (\sin^4\theta + \cos^4\theta) R^{(1)}_{H,H}(0)\, R^{(1)}_{V,V}(0) + \\ & - \sin^2\theta\cos^2\theta\left[R^{(1)}_{H,H}(\bar{\tau})\, R^{(1)}_{V,V}(-\bar{\tau}) + R^{(1)}_{H,H}(-\bar{\tau})\, R^{(1)}_{V,V}(\bar{\tau})\right], \end{aligned} \tag{5.2}$$

where the terms of $R^{(2)}_{PS}(\bar{\tau})$ containing an odd number of V-polarised field operators vanish because the squeezed vacuum state is invariant with respect to the transformation (2.15). The last two lines of Eq. (5.2) cancel if we choose $\bar{\tau} = 0$, i.e. coincident photon detection, and $\theta = \pi/4$, which

corresponds to choosing a polarisation basis with vectors lying on the equator of the Poincaré sphere:

$$R^{(2)}_{PS}(0) = \frac{1}{4}\left[R^{(2)}_{HH,HH}(0) + R^{(2)}_{VV,VV}(0) - 2\left|R^{(2)}_{HH,VV}(0)\right|\cos 2(\varphi - \phi)\right], \tag{5.3}$$

with $R^{(2)}_{HH,VV}(\bar{\tau}) = \left|R^{(2)}_{HH,VV}(\bar{\tau})\right| e^{2i\varphi} = \left[R^{(2)}_{VV,HH}(\bar{\tau})\right]^*$, where φ is the relative optical phase between the two orthogonal polarisation modes. We can rewrite the previous equation in a more compact form

$$R^{(2)}_{PS}(0) \propto 1 - V\cos\left[2(\varphi - \phi)\right] \tag{5.4}$$

that depends on the visibility V of the two-photon interference pattern

$$V = \frac{2\left|R^{(2)}_{HH,VV}(0)\right|}{R^{(2)}_{HH,HH}(0) + R^{(2)}_{VV,VV}(0)}. \tag{5.5}$$

The visibility V is maximum when $R^{(2)}_{HH,HH}(0) = R^{(2)}_{VV,VV}(0) = R^{(2)}_{HH,VV}(0)$: this condition is satisfied by a maximally entangled two-photon ODM. Note that the condition for maximum visibility of two-photon interference is the optimal condition to retrieve the two-photon wavefunction of a squeezed vacuum state. At the same time, it defines the region with higher concurrence for the two-photon ODM of a polarisation squeezed state.

5.2 EXPERIMENTAL TWO-PHOTON INTERFERENCE

In order to observe the oscillation in the detection rate predicted by Eq. (5.4), we record photon arrivals for 8 settings of the waveplates (see Table 5.1). They correspond to 8 values of ϕ, while stabilising the phase $\varphi = \pi/2$ with the method described in 4.3.1.

We wrote a C++ program to transform the time stamps into a discrete correlation function $m^{(i,j)}_{\phi}(\bar{\tau})$ that gives, for each setting ϕ and pair of detectors (i,j), the number of photon pairs detected in the time bins centred around $\bar{\tau}$ and with width $\Delta\tau$. The bin width is an integer multiple of 2 ns, the minimum time resolution for the digital time-of-flight counter when using four detectors, as in our detection setup shown in Fig. 4.1.

The interference effect described in Eq. (5.4) is a sinusoidal variation of the number of detections for two photons with orthogonal polarisation, therefore we need to sum the histograms that correspond to detector pairs associated to different polarisations.

In order to combine correctly the histograms derived from different detector pairs, we try to equalise the optical path leading to each detector and the length of the cables that connect each detector to a channel in the time-of-flight counter (TOFC). However, any small difference is translated into a temporal offset between the different channels of the TOFC. We measure this offset by sending square pulses (300 ns FWHM) of H-polarised coherent light into the detection setup, setting the waveplates ($\theta_{HWP} = 22.5°$, $\theta_{QWP} = 0°$), so that the light is equally split on

Setting	ϕ (radians)	θ_{HWP} (degrees)	θ_{QWP} (degrees)
0	0	22.5	45
1	$\pi/8$	16.875	45
2	$\pi/4$	11.25	45
3	$3\pi/8$	5.625	45
4	$\pi/2$	0	45
5	$5\pi/8$	-5.625	45
6	$3\pi/4$	-11.25	45
7	$7\pi/8$	-16.875	45

Table 5.1: The angles at which the half- and quarter-wave plate are set, θ_{HWP} and θ_{QWP} respectively, determine the measurement phase ϕ. The waveplates are calibrated so that the H and V polarisations match the axes of the PMF when $\theta_{QWP} = \theta_{HWP} = 0$.

Detector pair (i,j)	$\text{off}_{(i,j)}$ (ns)
(1,2)	10
(1,3)	10
(1,4)	8
(2,3)	-6
(2,4)	-8
(3,4)	-6

Table 5.2: Time offsets associated to detector pairs.

each detector. The expected second order correlation function is symmetric with respect of $\bar{\tau} = 0$, where it has a maximum: the offset in the peak of the photon coincidence histogram is the delay between the different TOFC channels. The time offsets we measured are shown in Table 5.2.

Knowing these offsets, we can sum the histograms corresponding to the detection of two photons with different polarisations:

$$M_\phi(\bar{\tau}) = \sum_{(i,j)\in\mathcal{A}_\perp} \left[m_\phi^{(i,j)}(\bar{\tau}) - \text{off}_{i,j} \right], \tag{5.6}$$

where $\mathcal{A}_\perp = \{(1,3),(1,4),(2,3),(2,4)\}$.

We choose a low OPO pump power, 1 mW approximately, that corresponds to the 0.4% of the OPO threshold, because it is the optimal power for the experiment that we will describe in the following Chapters. In fact, given that low squeezing leads to high ODM concurrence, this is the lowest pump power for which we can lock the phase φ. As observed in the previous Section, maximum visibility is reached for $R^{(2)}_{HH,HH}(0) = R^{(2)}_{VV,VV}(0) = R^{(2)}_{HH,VV}(0)$. Consequently, we tune the power of the coherent beam to achieve $m_0^{(1,2)}(0) \approx m_0^{(3,4)}(0)$ when the waveplates are

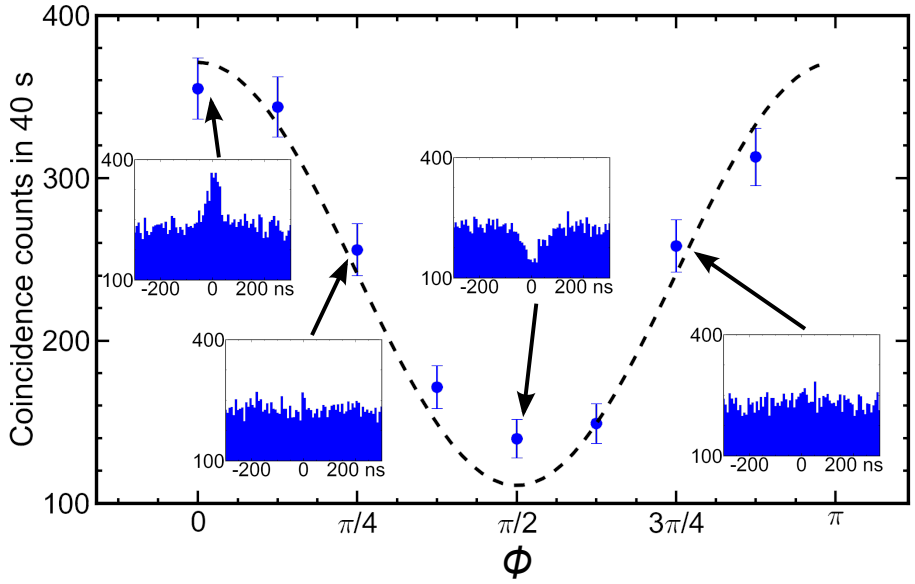

Figure 5.1: Arrival-time distributions showing interference of two-photon amplitudes. Main graph shows the measured coincidence histogram $M_\phi(0)$ (circles) for delay $\bar{\tau} = 0$ versus analysis phase ϕ for a coincidence windows of $\Delta\tau = 8$ ns. The dashed line is $A(1 + V\cos(2\phi))$, where $V = 0.54$ is the expected visibility, while A comes from a fit to the data. The sinusoidal behaviour in good agreement with the data reveals two-photon interference as predicted by (5.4). Insets show $M_\phi(\bar{\tau})$ for the values of ϕ indicated by the arrows. These clearly show the passage from constructive interference at $\phi = 0$, where a peak is visible, to destructive interference at $\phi = \pi/2$, where a dip appears. Error bars show $\pm 1\sigma$ (standard deviation) statistical uncertainty.

set to $\theta_{HWP} = \theta_{QWP} = 0$, so that the V-polarised light reaches the detectors 1 and 2 and the H-polarised light goes to detectors 3 and 4.

The results of the measurement are shown in Fig. 5.1. We observe both constructive and destructive interference, for $\phi = 0$ and $\phi = \pi/2$, respectively, as predicted by Eq. (5.4). The $M_{\pi/2}$ histogram is particularly interesting, because its dip is clear evidence of interference. In fact, the coherent state has a flat second order correlation function as in Eq. (3.22a), while squeezed vacuum has one peaked around $\bar{\tau} = 0$, see Eq. (3.22e). For $|\bar{\tau}| > 100$ ns, both correlation functions are constant, and so is the global $R^{(2)}_{PS}$. The dip that appears in the $|\bar{\tau}| < 100$ ns region of the $R^{(2)}_{PS}$ when $\phi = \pi/2$ has the same width as the correlation function of the squeezed vacuum and can only be explained as an effect of interference between the two polarisation components.

5.2.1 *Visibility*

The points in Fig. 5.1 represent the experimental values of $R^{(2)}_{PS}(0)$ for different values of ϕ: they follow a sinusoidal pattern as predicted by Eq. (5.4). We can compute the visibility of that oscillation starting from Eq. (5.5) and correcting it taking into account the contribution of the background to obtain a value that matches the experimental results.

We obtain $R^{(2)}_{HH,HH}(0)$ and $R^{(2)}_{VV,VV}(0)$ directly from the data: they correspond to $m_0^{(1,2)}(0) = 68$ counts and to $m_0^{(3,4)}(0) = 366$ counts, respectively, in a coincidence windows of 8 ns for an acquisition time of 19 s. $|R^{(2)}_{HH,VV}(0)|$ cannot be measured directly, but can be estimated from the previous measurements. In fact, Eq. (2.6) for a realistic photodetector with finite time resolution $\Delta\tau$ can be approximated by

$$R^{(2)}_{ij,mn}(\bar{\tau}) \approx \Delta\tau\, G^{(2)}(\bar{\tau}), \tag{5.7}$$

so that $|R^{(2)}_{HH,VV}(0)|$ can be written as

$$\left|R^{(2)}_{HH,VV}(0)\right| \approx \Delta\tau \left|\langle\, \hat{a}^\dagger_H(t)\hat{a}^\dagger_H(t)\hat{a}_V(t)\hat{a}_V(t)\,\rangle\right|. \tag{5.8}$$

If both the H- and V-polarised states contain no more than two photons each, we can express the previous equation in function of the two-photon temporal wave-functions of the two polarisation components:

$$\begin{aligned}\left|R^{(2)}_{HH,VV}(0)\right| &\approx \Delta\tau \left|\langle\, \hat{a}^\dagger_H(t)\hat{a}^\dagger_H(t)|0\rangle\langle 0|\hat{a}_V(t)\hat{a}_V(t)\,\rangle\right| = \\ &= \Delta\tau \left|\psi^*_{H,H}(0)\psi_{V,V}(0)\right|.\end{aligned} \tag{5.9}$$

Similarly, we can write

$$R^{(2)}_{HH,HH}(0) \approx |\psi_{H,H}(0)|^2\, \Delta\tau, \tag{5.10}$$

$$R^{(2)}_{VV,VV}(0) \approx |\psi_{V,V}(0)|^2\, \Delta\tau, \tag{5.11}$$

resulting in

$$V \approx \frac{2\Delta\tau \left|\psi^*_{H,H}(0)\psi_{V,V}(0)\right|}{|\psi_{H,H}(0)|^2 \Delta\tau + |\psi_{V,V}(0)|^2 \Delta\tau} = \frac{\sqrt{m_0^{(1,2)}(0) m_0^{(3,4)}(0)}}{m_0^{(1,2)}(0) + m_0^{(3,4)}(0)}. \tag{5.12}$$

The above equation is derived assuming that all the light we collect belongs to the polarisation squeezed state. However, in order to predict correctly the outcome of the experiment, we have to take into account also the accidental counts due to the detection of a photon coming from the polarisation squeezed state and a background photon. We can estimate them from the single photon counts $\beta_{0^\circ}^{(i)}$ that are recorded by detector i when we set the waveplates to $\theta_{HWP} = \theta_{QWP} = 0$. We then block the OPO pump and the coherent beam to measure the background counts b_i. The accidental counts (including the negligible contribution of the coincident detection of two photons from the background) can be estimated by $acc_{(i,j)} = [\beta_{0^\circ}^{(i)} \beta_{0^\circ}^{(j)} - (\beta_{0^\circ}^{(i)} - b_i)(\beta_{0^\circ}^{j} - b_j)]\Delta\tau$, where i, j are the indices of the detectors involved in the measurement. If we compute the visibility by subtracting the accidental counts contribution to the observed coincidences, we obtain the value

$$V = \frac{\sqrt{(m_0^{(1,2)}(0) - acc_{(1,2)})(m_0^{(3,4)}(0) - acc_{(3,4)})}}{m_0^{(1,2)}(0) - acc_{(1,2)} + m_0^{(3,4)}(0) - acc_{(3,4)}} = 0.54, \tag{5.13}$$

that agrees with data and that it is used to plot the dashed line in Fig. 5.1, where only the constant of proportionality is obtained from a fit.

5.2.2 *Discussion*

We analyse the interference between the two-photon components of two different states with orthogonal polarisation, namely a coherent state and a squeezed vacuum state. We predict that its effect can be observed as oscillations in the value of the second order correlation function depending on the phase between the two input states. With the experimental setup described in the previous Chapter we are able to observe a clear interference pattern shown in Fig. 5.1. This demonstrates our ability to generate a coherent superposition of two-photon states orthogonally polarised: this is an important requirement for both obtaining the two-photon temporal wavefunction and generating multipartite entanglement, as we show in the following Chapters.

6

COMPLETE TWO-PHOTON WAVEFUNCTION CHARACTERISATION

The interference between photon pairs belonging to different polarisation modes that we demonstrated in the previous Chapter is the phenomenon that is at the basis of the wavefunction reconstruction technique that we developed in Chapter 2. In this Chapter, we use the same experimental setup to reconstruct the temporal two-photon wavefunction of a squeezed vacuum state, obtaining results that agree with the theoretical model and that are published in [BZL+14].

6.1 MEASUREMENT SETTINGS

As for the two-photon interference, we need to measure the arrival time of two photons with orthogonal polarisation to obtain the temporal two-photon wave function. According to Eq. (2.19), we only need the second order correlation functions that correspond to three different polarisation bases: the waveplates settings for each polarisation basis are shown in Table 6.1.

With the phase locked between the two polarisation components by the quantum noise lock described in Section 4.3.1, we record the photon arrival time for each detector and each setting. The experimental data are analysed as in Section 5.2, obtaining the discrete functions $M_\phi(\bar{\tau})$ corresponding to the second order correlation functions as in Eq. (5.6). We choose a bin width $\Delta\tau = 4$ ns as a tradeoff between time resolution of the reconstructed wavefunction and statistical significance of the values of $M_\phi(\bar{\tau})$. The results are shown in Fig. 6.1.

Setting	ϕ (radians)	θ_{HWP} (degrees)	θ_{QWP} (degrees)
0	0	22.5	45
1	$\pi/3$	7.5	45
2	$2\pi/3$	-7.5	45

Table 6.1: The angles at which the half- and quarter-wave plate are set, θ_{HWP} and θ_{QWP} respectively, determine the measurement phase ϕ.

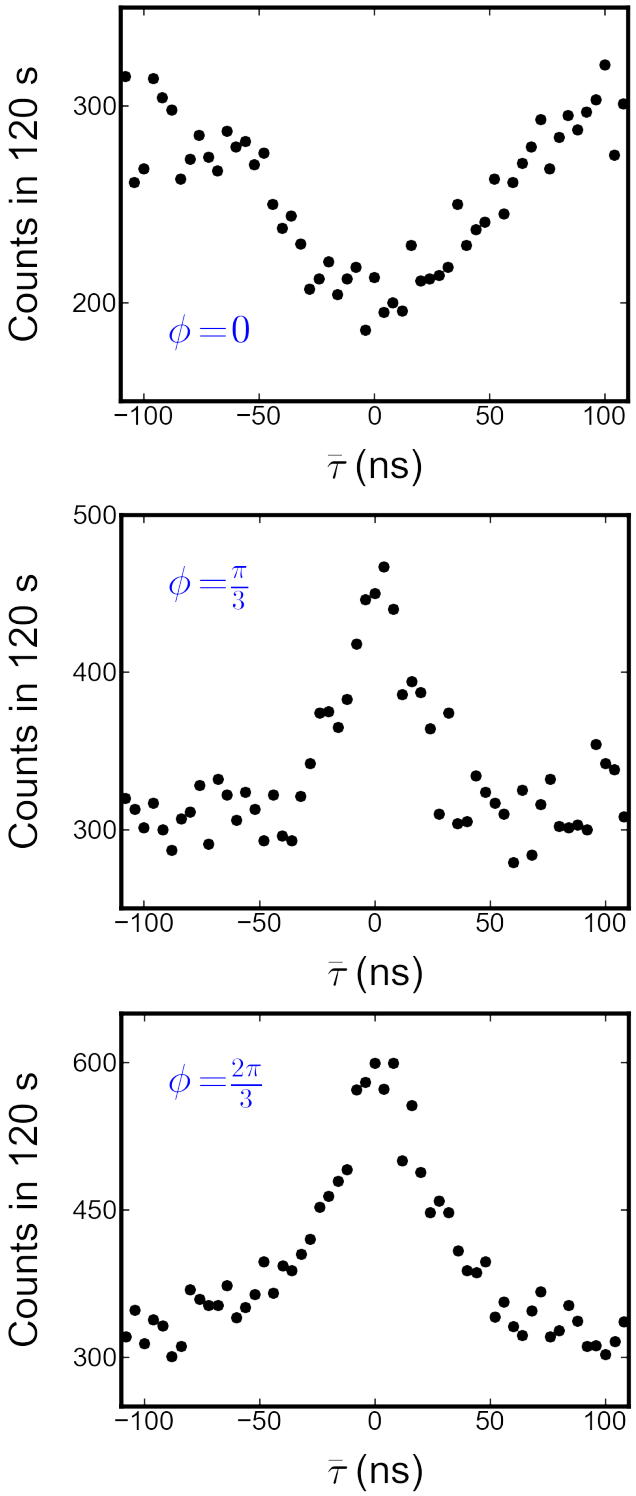

Figure 6.1: Experimental histograms $M_{\phi}^{(2)}(\bar{\tau})$ with 4 ns bins for each phase ϕ necessary for the wavefunction reconstruction. The dip in the $\phi = 0$ histogram is an evidence of the interference between the two orthogonal components.

As in the previous Chapter, we choose low OPO pump power ($\sim$ 1 mW) and we tune the power of the coherent state so that the rate of CS pairs and SV pairs are approximately equal, i.e., so that $m_0^{(1,2)}(0) \approx m_0^{(3,4)}(0)$ when the waveplates are set to $\theta_{QWP} = \theta_{HWP} = 0$.

6.2 RESULTS AND DISCUSSION

The histograms of Fig. 6.1 contain all the information necessary for the reconstruction the two-photon temporal wavefunction: we take $y_j = M^{(2)}_{j\pi/3}(\bar{\tau})$, with $j \in 1, 2, 3$, and substitute it in Eqs. (2.19) and (2.21) for every $\bar{\tau}$ to obtain $\psi^{(SV)}_{V,V} = |\psi^{(SV)}_{V,V}|e^{i\chi}$. Unlike the two-photon interference experiment, here there is no need to subtract the contribution of accidental counts due to the background. In fact, they cancel in Eq. (2.20). They only cause an overestimation of the value of γ, which does not alter the shape of the wavefunction. Fig. 6.2 shows the squared amplitude and the complex phase of $\psi^{(SV)}_{V,V}$. We assume Poissonian statistics for each value of y_j and we propagate the error through the analytical formulae to obtain the errors associated to the reconstructed values shown in Fig. 6.2.

We observe that the experimental wavefunction agrees within statistical uncertainties with the theoretical prediction: as $|\psi^{(SV)}_{V,V}|^2 \propto G^{(2)}_{VV,VV}$, we fit the experimental data with Eq. (3.22e), using the multiplicative constant as a free parameter and the measured parameters $\mu^2 = 0.4\%$ and $\delta\nu = 8.4\pi$ MHz. The complex phase of the wavefunction

$$\chi = \arctan\left[\frac{\mathrm{Im}(\psi^{(SV)}_{V,V})}{\mathrm{Re}(\psi^{(SV)}_{V,V})}\right] \tag{6.1}$$

is consistent with a constant value, as expected for an ideal OPO. Defects in the cavity may result in a different phase pattern [KWKT08, OU09], meaning that this technique could be a useful diagnostic tool for photon pair sources. The value of the phase offset depends on the phase lock and can be tuned by changing the phase difference φ between the horizontal and the vertical components.

The squeezed vacuum we use in the experiment has a finite bandwidth, which gives a limited temporal extension of the wave function: in particular, the predicted FWHM is 26 ns. The effects of the interference between the squeezed vacuum and the coherent reference are larger near the center of the wavefunction ($\bar{\tau} = 0$) and become smaller for increasing $\bar{\tau}$, until only the contribution of incoherent pairs is relevant. This explains why for $|\bar{\tau}| > 30$ ns we obtain larger error bars and a more irregular distribution of the data. If one considers only the time interval in which the interference effects can be distinguished from the background ($|\bar{\tau}| < 30$ ns), the reconstructed values of the phase have rms uncertainties of about 10 degrees.

6.2.1 *Purity*

The procedure we describe assumes a pure state. The output of an ideal OPO, i.e. a one-mode squeezed state, is indeed a pure state if we consider its two-photon component. Nevertheless,

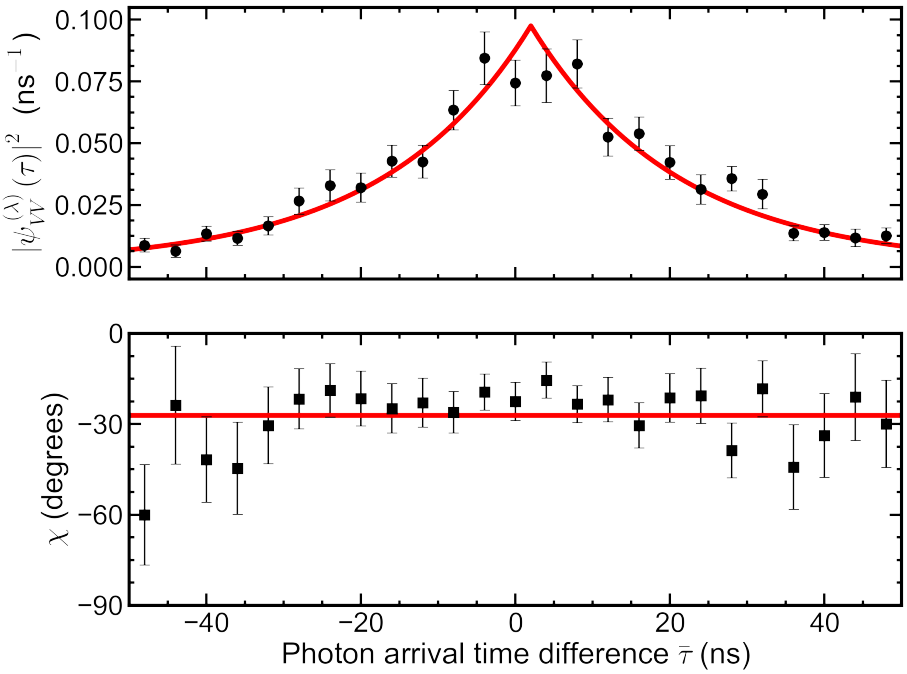

Figure 6.2: Squared amplitude (above) and phase (below) of the reconstructed two-photon wave function for the squeezed vacuum state. The solid line shows the predicted squared amplitude describing an ideal squeezed vacuum state from our OPO with an independently-measured 8.4 MHz bandwidth, with the overall multiplicative factor fitted to the data. Error bars show $\pm 1\sigma$ statistical uncertainty assuming Poisson statistics and using propagation of error through Eqs.(2.19), (2.20) and (2.21).

in our experimental implementation, some entropy will be added due to phase and amplitude fluctuations of the pump laser, which are transferred onto the output, creating some mixing. Based on measurements of the fluctuations of the phase stabilisation system and of the laser power fluctuations, we estimate these to be at the 10° and 1% power levels, respectively. As we show now, these variations will make an error in reconstruction smaller than the statistical uncertainties. For this reason, we believe the pure-state approximation is reasonable for this work.

If we use our procedure to analyse a mixed state, the result does not give $\psi^{(\lambda)}_{V,V}$, but rather a good approximation to its statistical average. To see this, consider a vertically-polarised mixed state $\sum_{n=1}^{N} p_n|\lambda_n\rangle\langle\lambda_n|$ interfered against a horizontally-polarised coherent state $|\alpha\rangle$. We measure the second order correlation of the the global state $|\kappa\rangle\langle\kappa| = \sum_{n=1}^{N} p_n|\kappa_n\rangle\langle\kappa_n| = \sum_{n=1}^{N} p_n|\lambda_n\rangle\langle\lambda_n| \otimes |\alpha\rangle\langle\alpha|$:

$$\begin{aligned} G^{(2)}_{\kappa}(t_1,t_2) &= |\tilde{\psi}^{(\kappa)}_{AB}(t_1,t_2)|^2 \\ &= \langle 0|\hat{a}_A(t_1)\hat{a}_B(t_2)|\kappa\rangle\langle\kappa|\hat{a}^{\dagger}_B(t_2)\hat{a}^{\dagger}_A(t_1)|0\rangle \\ &= \sum_n p_n|\tilde{\psi}^{(\kappa_n)}_{AB}(t_1,t_2)|^2 \\ &\propto \sum_n p_n|\gamma_n e^{-2i\phi} - \psi^{(\lambda_n)}_{V,V}(t_1,t_2)|^2\,, \end{aligned}$$

where $\gamma_n = \psi^{(\alpha)}_{H,H}\langle 0|\lambda_n\rangle\langle 0|\alpha\rangle^{-1}$. Remembering our shorthand $y_k \propto G^{(2)}_{\kappa}(t_1,t_2)$ with $\phi = k\pi/3$, and the definition of $\mathring{y}$ in (2.20), we find

$$\begin{aligned} \mathring{y} &\equiv -\frac{1}{3}\sum_{k=0}^{2} e^{-ik2\pi/3}\sum_n p_n|\gamma_n e^{-ik2\pi/3} - \psi^{(\lambda_n)}|^2 \\ &= -\frac{1}{3}\sum_{k=0}^{2} e^{-ik2\pi/3}\sum_n p_n\left(|\gamma_n|^2 - \gamma_n e^{-ik2\pi/3}(\psi^{(\lambda_n)})^* - \gamma_n e^{ik2\pi/3}\psi^{(\lambda_n)} + |\psi^{(\lambda_n)}|^2\right) \\ &= \sum_n p_n\gamma_n\psi^{(\lambda_n)} \end{aligned} \tag{6.2}$$

The terms $|\gamma_n|^2$, $\gamma_n e^{-2ik\pi/3}(\psi^{(\lambda_n)})^*$, and $|\psi^{(\lambda_n)}|^2$ give no contribution, because they are orthogonal to the factor $\exp[-ik2\pi/3]$, in the sense that when multiplied and summed over k they give zero. This shows that, in case the state is mixed, the reconstruction is not perfect. However, in the low-brightness limit $\langle 0|\alpha\rangle \approx \langle 0|\psi^{(\lambda_n)}\rangle \approx 1$, γ_n is independent of n so that the reconstructed wavefunction approximates well the statistical average of the wavefunctions associated to the different components of the mixed state.

The data shown in Fig. 6.2 are taken in the power regime where, according to the calculations above, the reconstructed state should approximate well the statistical average of the mixed state wavefunctions. To check this, we simulate the reconstruction of a mixed state with ten components $\psi^{(\lambda_n)}$, chosen with a 1% rms amplitude deviation and 8° rms phase deviation, that corresponds to the measured rms phase fluctuations of our quantum noise lock system. The reconstructed ψ

agrees exactly with $\sum_n p_n \psi^{(\lambda_n)}$ in phase, and differs in amplitude by about 6%. This is smaller, but of the same order of magnitude, than the statistical uncertainties shown in Fig. 6.2. This means that in our case we can treat our squeezed vacuum state as pure and apply our reconstruction technique. On the other hand, it implies that in order to improve the accuracy of the measurement of the wavefunction, one has to increase not only the data acquisition time to reduce statistical uncertainties, but also to reduce phase and amplitude fluctuations to increase the purity of the detected state.

Here we propose a new technique to recover complete information about the temporal wavefunction of a two-photon pure state by means of an ancillary coherent state. Since this is an effect of the two-photon interference demonstrated in the previous Chapter, it is fundamental to keep a constant phase between the unknown and the ancillary state. Only a few measurements with different values of this phase are required to reconstruct the complex temporal wavefunction.

This technique allows us to obtain the two-photon wavefunction of a squeezed vacuum state generated with a sub-threshold OPO with good agreement with the expected behaviour. Furthermore, we check the validity of our result, making sure that the state we generate can be considered pure despite the experimental imperfections in our setup.

7

DIRECT OBSERVATION OF MICROSCOPIC PAIRWISE ENTANGLEMENT IN POLARISATION SQUEEZING

The observation of two-photon interference in Chapter 5 shows that we can stabilise the phase between the two orthogonal polarisation components of the polarisation squeezed state generated by the setup detailed in Chapter 4. This is not only the basic ingredient of the complete reconstruction of the wavefunction of the squeezed vacuum state presented in the previous Chapter, but it is also a fundamental step towards the observation of what we predicted in Chapter 3, i.e. that any two photons in a polarisation squeezed state are entangled.

The experimental results reported in this Chapter and in [BZL+15] confirm the predictions of Chapter 3: we reconstruct the state of photon pairs belonging to different polarisation squeezed states, finding that they are all entangled. Here we relate the details of the reconstruction process and discuss the experimental results in relation with the theoretical predictions.

7.1 STATE RECONSTRUCTION

In Chapter 3 we computed the two-photon density matrix that describes the polarisation state of photon pairs in a polarisation squeezed state. This is a complex quantity that cannot be measured directly with a single measurement. However, one can combine multiple measurements to obtain complete information about the state, thanks to quantum tomography. This same strategy has already been used to detect pairwise entanglement in multiphoton states, as in [CDMP+06], for example.

In our case, we have to reconstruct the state ρ of polarisation qubits, so we use a polarimeter setup like the one sketched in Fig. 4.4 to collect the number of photon pairs M_n for the polarisation basis labeled by n. The tomographic reconstruction is a procedure that recovers the density matrix ρ from the collection of $\{M_n\}$. Strictly speaking, it indicates the inversion of the operation that maps $\rho \to \{M_n\}$. However, this often leads to nonphysical results, e.g. negative matrices [JKMW01].

We thus choose to recover the density matrix via a maximum likelihood estimation (MLE) approach [JKMW01]. First, we define a matrix ρ that satisfies the characteristics of a density matrix, i.e. Hermitian, positive and with unit trace. We can thus predict the outcome $\mu_n(\rho)$ of the n-th measurement and compare it to the experimental outcome M_n with a likelihood function

$\mathcal{L}(\mu_n, M_n)$, that quantifies how similar they are. With standard optimisation algorithms, we can then obtain the ρ that minimises $\mathcal{L}$ and thus best matches the experimental outcomes $\{M_n\}$.

Before detailing the reconstruction procedure, we explain how we obtain the number of photon pairs from both the theory and the experiment.

7.1.1 *Photon pairs from the theory*

Each measurement can be associated to a positive-operator valued measure (POVM) operator Π_n, so that ideally the experimental outcome M_n can be predicted by computing

$$\mu_n = \mathrm{Tr}\left[\Pi_n \rho\right]. \tag{7.1}$$

A generic two-qubit state can be described by a 4x4 density matrix: this implies that we need a tomographically-complete set of 16 measurements in order to reconstruct each element of the matrix via discrete quantum tomography [JKMW01]. However, in our case we can take advantage of the permutational symmetry of the two-photon state (3.13) to reduce the number of measurements to 10, using the permutationally-invariant (PI) state reconstruction developed by Adamson and coworkers [ASMS07]. In fact, the polarisation density matrix describing the arrival of one photon at time t and of another one at time $t+\tau$ must be invariant under permutation of the time indices, because the SV and CS contributions to the state are continuous-wave, and because no subsequent optical elements couple arrival time to polarisation.

Using the triplet-singlet basis $\{HH, \psi^+, VV, \psi^-\}$, where $\psi^\pm \equiv (HV \pm VH)/\sqrt{2}$, we write a general PI state as $\rho_{PI} = L^\dagger L$, where

$$L \equiv \begin{pmatrix} p_1 & 0 & 0 & 0 \\ p_5 + ip_6 & p_2 & 0 & 0 \\ p_7 + ip_8 & p_9 + ip_{10} & p_3 & 0 \\ 0 & 0 & 0 & p_4 \end{pmatrix} \tag{7.2}$$

and the elements of $\mathbf{p} \equiv [p_1 \ldots p_{10}]$ are real parameters. We convert ρ_{PI} in the computational basis $\{HH, HV, VH, VV\}$ to obtain the density matrix $\rho(\mathbf{p})$ that is used in Eq. (7.1).

For each measurement setting n, there is an associated positive operator-valued measure (POVM) in the computational basis

$$\Pi_n \equiv (U_{HWP}^{(n)} U_{QWP}^{(n)})^{\otimes 2} P_n (U_{QWP}^{\dagger(n)} U_{HWP}^{\dagger(n)})^{\otimes 2}, \tag{7.3}$$

where

$$U_{HWP} \equiv \begin{pmatrix} \cos 2\theta_{HWP} & \cos 2\theta_{HWP} \\ \sin 2\theta_{HWP} & -\cos 2\theta_{HWP} \end{pmatrix}, \tag{7.4}$$

$$U_{QWP} \equiv \begin{pmatrix} \cos^2\theta_{QWP} + i\sin^2\theta_{QWP} & (1-i)\sin\theta_{QWP}\cos\theta_{QWP} \\ (1-i)\sin\theta_{QWP}\cos\theta_{QWP} & i\cos^2\theta_{QWP} + \sin^2\theta_{QWP} \end{pmatrix} \tag{7.5}$$

are the Jones matrices associated to the quarter- and half-wave plate, respectively, and P_n are projectors associated to the detection of photon pairs with a specific polarization, i.e. $P_1 = |HH\rangle\langle HH|$, $P_2 = |VV\rangle\langle VV|$ and $P_3 = |HV\rangle\langle HV| + |VH\rangle\langle VH|$.

Ideally, one can use Eq. (7.1) to estimate the pair counts for each measurement settings. However, in a real experiment, Eq. (7.1) must be corrected to take into account experimental imperfections.

It is important in our case to take into account the effect of background photons during the tomographic reconstruction: while the probability of detecting two background photons within the coincidence window $\Delta\tau$ is negligible, coincidences between one signal and one background photon are relevant, given the high fluxes of squeezed and coherent photons. To estimate the number of accidental pair counts, we use the number of photons $\beta_n^{(i)}$ that reach detector i during the n-th measurement. We also need to measure the number of background photons $b_n^{(i)}$ on channel i for the n setting, obtained by blocking the OPO pump and the CS beam: these are mainly due to the residual OPO locking beam and to non-degenerate modes passing through the FADOF [ZBLM14]. We can thus compute

$$\mathrm{acc}_n^{(i,j)} = [\beta_n^{(i)}\beta_n^{(j)} - (\beta_n^{(i)} - b_n^{(i)})(\beta_n^{(j)} - b_n^{(j)})]\Delta\tau, \tag{7.6}$$

where i, j are the indices of the detectors involved in the n-th measurement:

$$\mathrm{acc}_n = \begin{cases} \mathrm{acc}_n^{(1,2)} & \text{for } n = 1,4,5,8,9 \\ \mathrm{acc}_n^{(3,4)} & \text{for } n = 2 \\ \sum_{i=1}^{2}\sum_{j=3}^{4}\mathrm{acc}_n^{(i,j)} & \text{for } n = 3,6,7,10 \end{cases} \tag{7.7}$$

We also take into account that each detection channel, which in principle should be identical to the others, has in practice a different efficiency from the others. To measure this, we first send a continuous coherent beam to the detection setup with the waveplates set to $\theta_{QWP} = 0°$ and $\theta_{HWP} = 22.5°$, so that the light is equally split among all detectors. We then record the number of photons $\beta_{45°}^{(i)}$ that reach detector i when the polarimeter measures the polarisation in the basis -45°/45°. We compute the normalised path-and-detector efficiency $\gamma_i = \beta_{45°}^{(i)} / \sum_j \beta_{45°}^{(j)}$.

In this detection system any given SPAD cannot distinguish between one or more photons arriving: the signal we obtain is the same as if only one photon was detected. For this reason, when the fibre beam splitter splits equally the light between two SPADs, half of their pair detections are lost. We take into account this by multiplying by 2 the efficiency factor η_n for n-th outcome:

$$\eta_n = \begin{cases} 2\gamma_1\gamma_2 & \text{for } n = 1,4,5,8,9 \\ 2\gamma_3\gamma_4 & \text{for } n = 2 \\ (\gamma_1+\gamma_2)(\gamma_3+\gamma_4) & \text{for } n = 3,6,7,10. \end{cases} \tag{7.8}$$

The probability of three or more photons arriving to the same detector is negligible, as the optimal condition for high concurrence requires low photon rates.

n	θ_{HWP}	θ_{QWP}	P	Detectors
1	0	0	P_1	D_1D_2
2	0	0	P_2	D_3D_4
3	0	0	P_3	$\sum_{i=1}^{2}\sum_{j=3}^{4} D_iD_j$
4	$\pi/16$	0	P_1	D_1D_2
5	$\pi/8$	0	P_1	D_1D_2
6	$\pi/8$	0	P_3	$\sum_{i=1}^{2}\sum_{j=3}^{4} D_iD_j$
7	$\pi/8$	$\pi/4$	P_3	$\sum_{i=1}^{2}\sum_{j=3}^{4} D_iD_j$
8	$\pi/8$	$\pi/8$	P_1	D_1D_2
9	$\pi/4$	$\pi/8$	P_1	D_1D_2
10	0	$\pi/8$	P_3	$\sum_{i=1}^{2}\sum_{j=3}^{4} D_iD_j$

Table 7.1: Projector operators (P) and detector pairs associated to the experimental result $n_{exp,m}$, corresponding to the waveplates setting $\{\theta_{HWP}, \theta_{QWP}\}$.

Each M_n is obtained from a measurement that lasts approximately half an hour. It is then plausible that the brightness of the source can vary significantly on such a long time scale. We thus define $\alpha_n \equiv \sum_i \beta_n^{(i)}/\gamma_i$, the total brightness of the input state during measurement n, to account for drifts in the brightness of the source during long acquisitions.

The corrected version of Eq. (7.1) takes the form

$$\mu_n(\mathbf{p}) = \mathrm{Tr}[\Pi_n \rho(\mathbf{p})]\eta_n \alpha_n + \mathrm{acc}_n. \tag{7.9}$$

to predict the photon pair count in our experimental conditions.

7.1.2 *Photon pairs counts from the experiment*

The quantum tomography experiment requires measuring the arrival time of photon pairs in the same way we did for the experiments described in Chapters 5 and 6, but with different waveplates settings, which are reported in Table 7.1. As we did for the previous experiments, we obtained a discrete version of the second order correlation function $m_n^{(i,j)}(\bar{\tau})$ by analysing the time stamps of a pair of detectors (i, j) and waveplate setting labeled by the parameter n in Table 7.1 to obtain the number of photon pairs that were detected with time separation $\bar{\tau}$ within the coincidence window $\Delta\tau$. Thanks to the four SPADs configuration, we can obtain the 10 experimental results M_n ($n = 1 \ldots 10$) with just the 7 waveplates settings shown in Table 7.1, reducing significantly the total acquisition time.

We correct the $m_n^{(i,j)}(\bar{\tau})$ for the delay among the different channels, as in Section 5.2, obtaining

$$M_n(\bar{\tau}) = \begin{cases} m_n^{(1,2)}(\bar{\tau}) - \text{off}_{1,2} & \text{if } n = 1,3,5,8,9 \\ m_n^{(3,4)}(\bar{\tau}) - \text{off}_{3,4} & \text{if } n = 2 \\ \sum_{(i,j)\in\mathcal{A}_\perp} (m_\phi^{(i,j)}(\bar{\tau}) - \text{off}_{i,j}), & \text{if } n = 3,6,7,10 \end{cases} \tag{7.10}$$

where = $\mathcal{A}_\perp = \{(1,3),(1,4),(2,3),(2,4)\}$.

The theory developed in Chapter 3 predicts higher pairwise entanglement for lower squeezing: we thus set the OPO pump power at different values around 1 mW, that is the lowest power at which we were able to lock the phase between the two polarisation components with the technique described in Section 4.3.2. The other condition for high concurrence is $m_0^{(1,2)}(0) \approx m_0^{(3,4)}(0)$, so we tune the CS beam power to satisfy this condition. Note that the optimal conditions for this experiment coincides with the ones that gave better results for the experiments described in the previous Chapters.

7.1.3 *Maximum Likelihood Estimation*

The coincidence counts M_n follow a Poisson distribution that can be approximated by a Gaussian distribution for large numbers. We can thus write, as in [JKMW01], the probability that the collection of measurements $\{M_n\}$ can come from the density matrix ρ as

$$P_{MLE} \propto \Pi_{n=1}^{10} \exp\left\{-\frac{[\mu_n - M_n]^2}{2\sigma_n^2}\right\}, \tag{7.11}$$

where $\sigma_n = \sqrt{M_n}$. For simplicity, we use the logarithm of the previous expression as the likelihood function $\mathcal{L}$ [JKMW01]

$$\mathcal{L}(\mathbf{p}) \equiv \sum_{n=1}^{10} \frac{[\mu_n(\mathbf{p}) - M_n]^2}{2M_n}, \tag{7.12}$$

whose minimum corresponds to the maximum probability that the matrix generated with $\mathbf{p}$ generates the experimental outcomes $\{M_n\}$. We find the value of $\mathbf{p}$ that minimises Eq. (7.12) with the BFGS minimisation function (`scipy.optimize.fmin_bfgs`) from the SciPy library.

We used a bootstrapping technique to estimate the error on the density matrices derived with this method. We first generate 100 10-element lists, whose n-th elements are chosen randomly from a Poissonian distribution with mean corresponding to the 10 experimental values M_n with $n = 1 \ldots 10$. Then we apply our MLE algorithm to these lists, obtaining 100 density matrices. The distribution of their concurrence shows the effects of statistical errors on the entanglement, showing that even if the number of collected photons was relatively low (on the order of hundreds of counts), it is sufficient to demonstrate that the concurrence is different from 0 with some standard deviations. The error bars shown in the graphs are centred around the average of the distribution of concurrence and they are ± 1 standard deviations long.

We apply this reconstruction technique to different sets of measurements, associated to different values of the photon fluxes, to obtain the density matrices ρ shown in Fig. 7.1. These show the predicted "X" shape, apart from small but nonzero coherences off of the two diagonals, e.g. $\rho_{VV,VH}$. These are most probably generated by experimental imperfections, such as leakage of CS light into the SV polarization, e.g. by defects in the combining PBS or FBS. The density matrices show strong $\rho_{HH,VV}$ coherences, giving a good fidelity with a "NooN"-like state of the form $\cos\theta|HH\rangle + \sin\theta|VV\rangle$.

For each density matrix, we measure the entanglement by computing the concurrence as in Eq. (3.27), obtaining in all cases a statistically significant entanglement.

7.2 COMPARISON WITH THE THEORY

We compare the experimental density matrices shown in Fig. 7.1 with the calculations of Chapter 3.

7.2.1 *Theoretical density matrices*

The ODM of a polarisation squeezed state can be derived with the expressions in Eq. (3.22), that depend on a few experimental parameters. We measure the OPO bandwidth by comparing its transmission spectrum to the rubidium absorption spectrum, obtaining $\delta\nu = 8.4\pi$ MHz. We take the value of $\eta = 0.93$ from [Pre09].

In order to obtain the photon fluxes Φ_C and Φ_S, we use the single photon counts $\beta_1^{(i)}$ for the channel i when the polarisation squeezed state is measured with the H/V basis. This means that the light hitting detectors 1 and 2 belongs to the squeezed vacuum, while the CS beam gets to detectors 3 and 4. We correct these measurements for the background photons $b_1^{(i)}$ and the total efficiency, given by the product of the path-to-detector efficiency γ_i and the global efficiency η_G.

In order to estimate η_G, we set the waveplates ($\theta_{HWP} = \theta_{QWP} = 0°$) so that H and V polarisations are aligned to the fast and slow axis of the PMF, respectively. We then measure the power of a H-polarised coherent beam P_0 with a powermeter right after the PBS. We repeat the same measurement at both outputs of the FBS that leads to detector 3 and 4, obtaining P_3 and P_4, respectively. We define the global efficiency coefficient as the ratio $\eta_G = \eta_{det}(P_3 + P_4)/P_0$, where $\eta_{det} = 0.5$ is the quantum efficiency of the detectors for 795 nm, according to their data sheet.

We can then compute Φ_C and Φ_S with

$$\Phi_S = \frac{1}{T\,\eta_G}\left[\frac{\beta_{0°}^{(1)} - b_1^{(1)}}{\gamma_1} + \frac{\beta_{0°}^{(2)} - b_1^{(2)}}{\gamma_2}\right], \tag{7.13}$$

$$\Phi_C = \frac{1}{T\,\eta_G}\left[\frac{\beta_{0°}^{(3)} - b_1^{(3)}}{\gamma_3} + \frac{\beta_{0°}^{(4)} - b_1^{(4)}}{\gamma_4}\right], \tag{7.14}$$

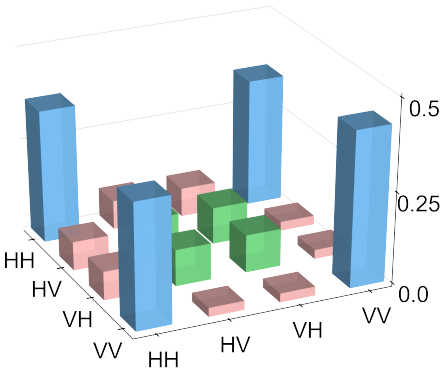

a) $\mathcal{C} = 0.54 \pm 0.01$
$\Phi_C = 2.54 \times 10^6$ photons/s
$\Phi_S = 7.42 \times 10^5$ photons/s

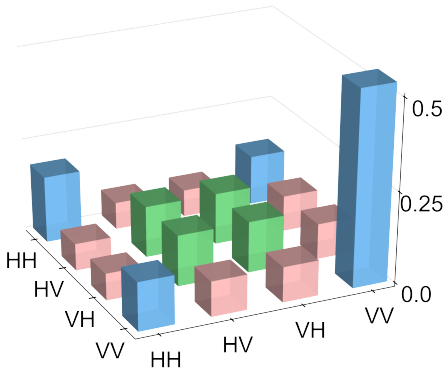

b) $\mathcal{C} = 0.07 \pm 0.05$
$\Phi_C = 9.44 \times 10^5$ photons/s
$\Phi_S = 7.66 \times 10^5$ photons/s

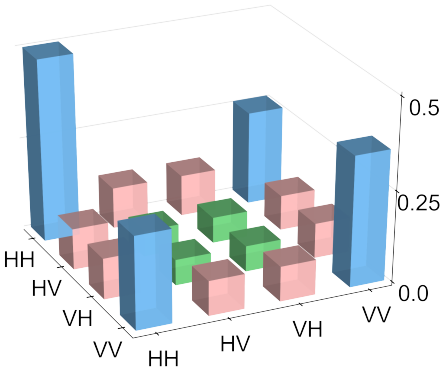

c) $\mathcal{C} = 0.49 \pm 0.04$
$\Phi_C = 4.18 \times 10^6$ photons/s
$\Phi_S = 6.12 \times 10^5$ photons/s

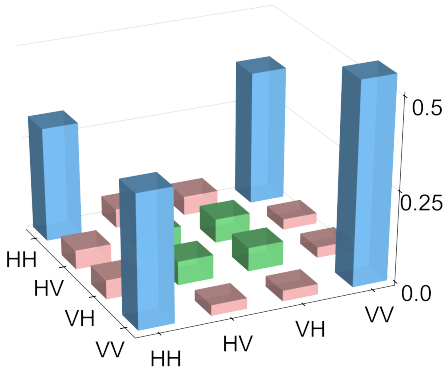

d) $\mathcal{C} = 0.65 \pm 0.05$
$\Phi_C = 9.61 \times 10^5$ photons/s
$\Phi_S = 1.94 \times 10^5$ photons/s

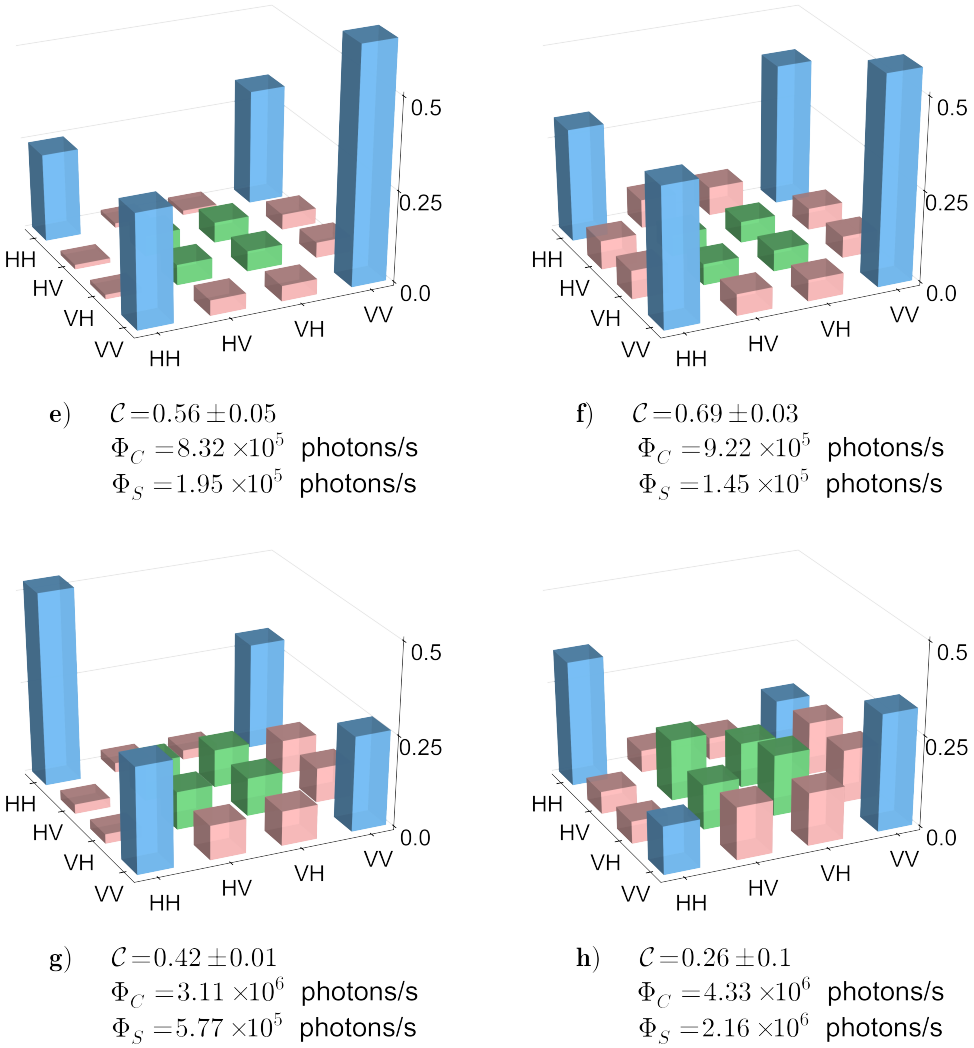

e) $\mathcal{C} = 0.56 \pm 0.05$
$\Phi_C = 8.32 \times 10^5$ photons/s
$\Phi_S = 1.95 \times 10^5$ photons/s

f) $\mathcal{C} = 0.69 \pm 0.03$
$\Phi_C = 9.22 \times 10^5$ photons/s
$\Phi_S = 1.45 \times 10^5$ photons/s

g) $\mathcal{C} = 0.42 \pm 0.01$
$\Phi_C = 3.11 \times 10^6$ photons/s
$\Phi_S = 5.77 \times 10^5$ photons/s

h) $\mathcal{C} = 0.26 \pm 0.1$
$\Phi_C = 4.33 \times 10^6$ photons/s
$\Phi_S = 2.16 \times 10^6$ photons/s

Figure 7.1: Experimental density matrices (magnitudes only) for a detection windows $\Delta\tau = 26$ ns centred on $\bar{\tau} = 0$. For each state we report the concurrence $\mathcal{C}$ and the photon fluxes of the CS and SV components (Φ_C and Φ_S, respectively) computed with Eqs. (7.14) and (7.13). Blue bars indicate the "NooN" portion of the state, a superposition of $|HH\rangle$ and $|VV\rangle$, green bars indicate the "W" portion of the state, $\propto |HV\rangle + |VH\rangle$, and pink bars indicate anomalous coherences.

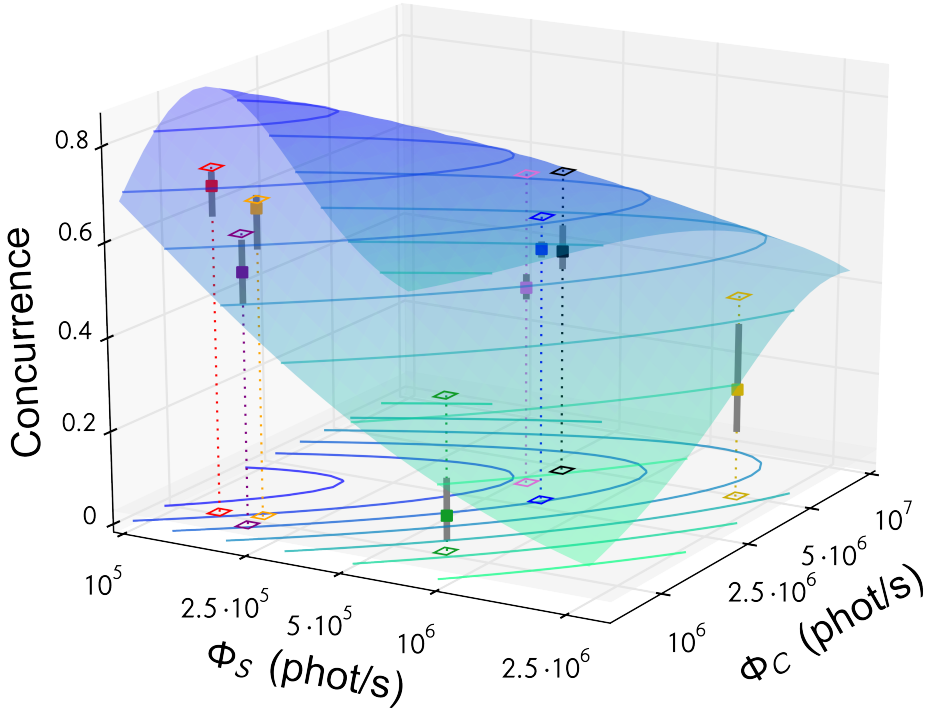

Figure 7.2: Comparison between the theoretical concurrence (surface) and the experimental observations (filled squares) for a coincidence time window of 26 ns centred on $\bar{\tau} = 0$. The contour plot and the empty squares on the bottom plane are the projection of the theoretical surface and of the experimental data on the space of SV and CS photon fluxes, Φ_S and Φ_C, respectively. The upper empty squares lie on the surface and represent the expected concurrence for the measured density matrices. Grey bars indicate $\pm 1\sigma$ statistical errors calculated by bootstrapping. For all cases, we obtain theoretical predictions by integrating the elements of the expected density matrix ρ over the time window considered.

where $T = t_{file} N_{file} D$ is the measurement time. As we explained in Section 4.2, the TOFC saves the time stamps in N_{file} files that each correspond to an acquisition time t_{file}. We need to take into account also the duty cycle ($D = 0.3$) of the synchronisation cycle explained in section 4.4, i.e. the ratio between the time spent on the data acquisition (DA) phase and the total time spent by the galvanometer mirror to complete a cycle. In fact, the gate system we built allows the signal from the detectors to arrive to the TOFC only during the DA phase, i.e. 30% of the time.

The measurement time T for each waveplate setting associated to the density matrices shown in Figure 7.1 varies from 1 s to 30 s. As we explained in Section 4.2.3, the overhead time of the TOFC makes the actual measurement time a lot longer, between 30 and 60 minutes. The values of T we chose are then a tradeoff between collecting photon statistics and actual measurement time: this is the reason why we chose smaller values of T for the measurements taken with higher photon rates. However, choosing to collect data during a reduced amount of time does not affect significantly the result of our experiment: in fact, the value of T only affects the size of the error bars derived with the bootstrapping analysis described in Section 7.1.3. A longer measurement time would imply smaller error bars, but the extra effort required is not necessary, since Figure 7.2 shows that the measured concurrence is well above 0 with more than 1 standard deviation for all the density matrices.

The value of $|\mu|$ can be easily obtained by inverting the definition of Φ_S given in Eq.(3.24):

$$|\mu|^2 = \frac{\Phi_S}{\eta\delta\nu + \Phi_S}. \tag{7.15}$$

For each measurement, we derive an experimental value of Φ_S and Φ_C from Eqs. (7.13) and (7.14). Then we substitute them into Eqs. (3.22) and we integrate on the detection window to get the theoretical ODM $\rho^{(th)}$ corresponding to the observed photon fluxes:

$$\rho^{(th)}_{ij,mn} \propto \int_{\bar{\tau}-\Delta\tau/2}^{\bar{\tau}+\Delta\tau/2} G^{(2)}_{ij,mn}(\tau)d\tau, \tag{7.16}$$

where we assume $\varphi_p - 2\varphi_{CS} = 0$ for simplicity, as the concurrence for an ODM of the form (3.21) is independent of the phase of the element c of the ODM.

7.2.2 *Discussion*

We compute the concurrence of $\rho^{(th)}$ with Eq. (3.27) and compare it with the experimental results, with the comparison shown graphically in Fig. 7.2. In general, the experimental values for the concurrence are lower than the theoretical ones. In fact, experimental imperfections, e.g. noise in the phase stabilisation on the time-scale of the acquisition, introduce decoherence in the state, which can only reduce the entanglement in the experimental realisations. Nonetheless, all the density matrices we obtained are entangled and for most of them the concurrence is within a few standard deviations of its theoretical value, confirming the presence of microscopic entanglement in a polarisation squeezed state.

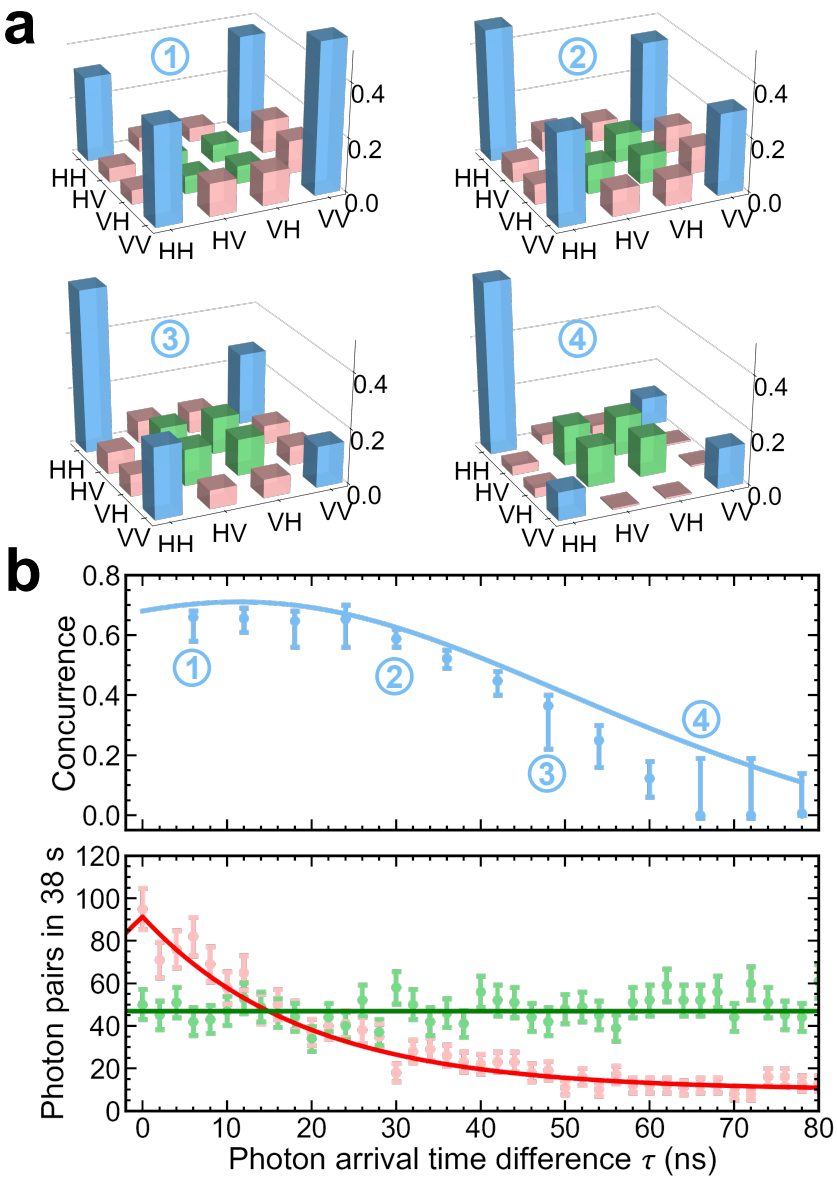

Figure 7.3: **(a)** Reconstructed density matrices (magnitudes only) of photons extracted from a PS state with $\Phi_C = 9.6 \times 10^5$ ph/s and $\Phi_S = 1.9 \times 10^5$ ph/s (orange square in Fig. 7.2) for mean arrival time differences $|\bar{\tau}| = 6, 30, 48$ and 66 ns. We include all events within the coincidence window $\Delta\tau = 12$ ns. **(b)** (upper) Concurrence of the two photon density matrices versus $|\bar{\tau}|$ under the same conditions. Error bars indicate $\pm 1\sigma$ statistical error estimated by a bootstrapping procedure. Results show entanglement for photons separated by up to 60 ns, as predicted by the theory (solid line). (lower) SV (red) and CS (green) contributions to the PS state. Shown are photon pair detection rates as a function of delay time for one or the other contribution, indicating a cross-over in source brightness at $\bar{\tau} = 15$ ns, which corresponds to balanced $|HH\rangle$, $|VV\rangle$ amplitudes and maximum concurrence.

Fig. 7.2 shows that the density matrices with higher concurrence are the ones with less squeezing, in agreement with the predictions of Chapter 3. We showed in [MB14] that this happens because larger squeezing is associated to a larger entanglement depth, meaning that large groups of photons are entangled. Entanglement monogamy [CKW00] prevents a particle to have maximum concurrence with another one if it is entangled with other particles, so that, as the entanglement depth grows, the concurrence has to decrease.

We also observe that the concurrence is maximum when the conditions for two-photon interference are optimal, i.e. when the pairs from the coherent state are equal to the ones from the squeezed vacuum. Fig. 7.3b shows that the concurrence is maximum when the number of measured pairs in the CS beam equals the contribution of the SV beam. As the time separation τ between the photons increases, the SV pairs decrease exponentially as expected, till the coherent contribution prevails. We can see in Fig.7.3a that this makes the density matrices lose their NOON-like character for increasing values of τ, becoming less and less entangled.

CONCLUSIONS AND OUTLOOK

This manuscript resumes the core of my activity, both theoretical and experimental, during my PhD studies and it describes two lines of research: a new technique for the reconstruction of complete information about the temporal wavefunction of a two-photon state and the demonstration of the presence of pairwise polarisation entanglement in polarisation squeezed states.

First, we have derived an analytical expression that relates the average photon pair rate, a quantity experimentally accessible, to the complex two-photon wavefunction. In fact, the interference of the two-photon state we want to measure with a coherent ancillary state makes the arrival-time distribution phase-sensitive. In contrast to most tomographic procedures [ASMS07, SBRF93], only three measurement settings are required to find the real and imaginary parts of the wave function. We use this technique to obtain the two-photon wavefunction of a squeezed vacuum state, i.e. the output of a narrow-band, atom-resonant OPO operating at 795 nm, and find results in good agreement with theory. The technique could be used to detect and correct errors in quantum light sources for quantum information processing [WXC$^+$08] and quantum metrology [WVB$^+$13], or to match the output of multiple sources for quantum communications [FRCdR13].

The coherent superposition of photon pairs belonging to the squeezed vacuum with the ones coming from the ancillary coherent state are at the basis of this technique. For this reason, the stabilisation of the phase between the two polarisation components is critical for the success of the experiment. To achieve this, as we could not reduce the natural phase drifts of the system with passive methods, we had to design an electronic system to keep the phase actively constant during the hour-long measurements required for the experiment. As a consequence, we had to develop a synchronisation system, because data acquisition and phase stabilisation required different power regimes.

This same experimental setup allowed us to demonstrate experimentally that polarisation squeezing, being a collective state, implies pairwise entanglement among all its photons, in analogy with atomic spin squeezing. More precisely, we have derived an inequality for photons, analogous to the result of Wang and Sanders [WS03], for spins in symmetric states. The result shows that nonclassical macroscopic polarisation correlations imply microscopic entanglement of the photons in the beam. Furthermore, we compute the entanglement associated to a particular implementation of a polarisation squeezed state, that is a combination of a squeezed vacuum state and a coherent state in orthogonal polarisation modes, just like the system we used for the demonstration of the wavefunction reconstruction. We found that any pair extracted from such a state is entangled, and that the amount of entanglement, calculated with the concurrence, is larger for the states that show large visibility for the same kind of two-photon interference that allowed the wavefunction reconstruction. As a consequence, a polarisation squeezed state can be considered as a source of

polarization-entangled photons that is robust against losses, making it of considerable interest for quantum networking applications.

Phase stabilisation between polarisation components is critical also in this case to observe the quantum coherences in the density matrices: without them, it wouldn't be possible to observe any entanglement. We are thus able to report the first particle-by-particle measurements on a macroscopic quantum state. Similarly to the first experiment, we analyse the joint polarisation state of photon pairs extracted randomly from a beam of polarization-squeezed light. We confirm several predictions of our theory, including strong entanglement, with concurrence up to 0.7, among all pairs of photons arriving within the squeezing coherence time, NooN-type entanglement, and concurrence that decreases with photon flux as required by entanglement monogamy.

It is possible to expand the same procedure to measure the density matrix describing larger groups of photons, and thus to detect the presence of multi-partite entanglement. The reconstruction of a larger observable density matrix requires the collection of a statistically significant collection of multiple photon detection events, which are rarer than pair detections: this means we need more single photon detectors and longer measurement times to detect multi-partite entanglement with this strategy, making it very unpractical as the size of the observable density matrices grows.

Hence, given the large entanglement depth predicted for this kind of states, it could be more convenient to use the same experimental setup to infer the number of entangled particles from the polarisation squeezing, as proposed in [MB14].

Our particle-by-particle analysis could also be applied to study the entanglement in interacting and/or computationally intractable bosonic systems, e.g., photon BECs [KSVW10], exciton polaritons [AAS+13], and Rydberg-blockade-bound photon gases [FPL+13].

LIST OF PUBLICATIONS

TWO-PHOTON WAVEFUNCTION RECONSTRUCTION:

F. A. Beduini, J. A. Zielińska, V. G. Lucivero, Y. A. de Icaza Astiz and M. W. Mitchell, *Interferometric Measurement of the Biphoton Wave Function*, Physical Review Letters **113**, 183602 (2014).

POLARISATION SQUEEZING AND ENTANGLEMENT:

F. A. Beduini and M. W. Mitchell, *Optical Spin Squeezing: Bright Beams as High-Flux Entangled Photon Sources*, Physical Review Letters **111**, 143601 (2013).

M. W. Mitchell and F. A. Beduini, *Extreme spin squeezing for photons*, New Journal of Physics **16**, 073027 (2014).

F. A. Beduini, J. A. Zielińska, V. G. Lucivero, Y. A. de Icaza Astiz and M. W. Mitchell, *Macroscopic Quantum State Analyzed Particle by Particle*, Physical Review Letters **114**, 120402 (2015).

OTHER TOPICS:

F. Wolfgramm, A. Cere, F. A. Beduini, A. Predojevic, M. Koschorreck and M. W. Mitchell, *Squeezed-Light Optical Magnetometry*, Physical Review Letters **105**, 053601 (2010).

F. Wolfgramm, Y. A. de Icaza Astiz, F. A. Beduini, A. Cere and M. W. Mitchell, *Atom-resonant heralded single photons by interaction-free measurement*, Physical Review Letters **106**, 053602 (2011).

J. A. Zielińska, F. A. Beduini, N. Godbout and M. W. Mitchell, *Ultra-Narrow Faraday Rotation Filter at the Rb D1 Line*, Optics Letters **37**, 524 (2012).

F. Wolfgramm, C. Vitelli, F. A. Beduini, N. Godbout and M. W. Mitchell, *Entanglement-enhanced probing of a delicate material system*, Nature Photonics **7**, 28 (2013).

J. A. Zielińska, F. A. Beduini, V. G. Lucivero and M. W. Mitchell,*Atomic filtering for hybrid continuous-variable/discrete-variable quantum optics*, New Journal of Physics **16**, 073027 (2014).

Appendix

A

OBSERVABLE TWO-PHOTON DENSITY MATRIX FOR A POLARISATION SQUEEZED STATE

As explained in Section 2.2, the observable density matrix (ODM) is a tool that connects the theoretical predictions about the two-photon polarisation state of a macroscopic state to the second-order correlation functions $\mathbf{G}^{(2)}$, that are directly related to the photon pair rates that can be measured experimentally. Here we explain in detail how we derived the ODM for a polarisation squeezed state obtained by combining the output of a V-polarised sub-threshold OPO (squeezed vacuum state) and a coherent state with orthogonal polarisation. We consider only stationary fields.

A.1 FIRST ORDER CORRELATION FUNCTION

We consider a monochromatic coherent state $|\alpha\rangle$ with amplitude $\alpha \equiv e^{i\varphi_{CS}}\sqrt{\Phi_C}$. It is easy to show that the first order correlation function is equal to

$$G^{(1)}_{H,H}(\tau) = \Phi_C, \tag{A.1}$$

where Φ_C is the photon rate corresponding to the coherent state.

For a squeezed vacuum state generated by a sub-threshold OPO, we must rewrite each field operators according the Bogoliubov transformation [CG84]:

$$\hat{a}_V(\omega) = f_1(\omega)\,\hat{a}_1(\omega) + f_2(\omega)\,\hat{a}_1^\dagger(-\omega) + f_3(\omega)\,\hat{a}_2(\omega) + f_4(\omega)\hat{a}_2^\dagger(-\omega) \tag{A.2}$$

where $\hat{a}_1$ is the operator related to the vacuum field entering the OPO cavity due to the output coupler, whereas $\hat{a}_2$ is associated to intracavity losses. The coefficients in the previous expression can be written as

$$f_1(\omega) = \frac{1}{A(\omega)}\left[\eta^2 - \left(1-\eta-i\frac{\omega}{\delta\nu}\right)^2 + |\mu|^2\right] \tag{A.3}$$

$$f_2(\omega) = \frac{2\eta\mu}{A(\omega)} \tag{A.4}$$

$$f_3(\omega) = \frac{2\sqrt{\eta(1-\eta)}}{A(\omega)}\left(1-i\frac{\omega}{\delta\nu}\right) \tag{A.5}$$

$$f_4(\omega) = \frac{2\mu\sqrt{\eta(1-\eta)}}{A(\omega)} \tag{A.6}$$

$$A(\omega) = \left(1-i\frac{\omega}{\delta\nu}\right)^2 - |\mu|^2 \tag{A.7}$$

where η is the cavity escape efficiency, the cavity FWHM bandwidth $\Gamma = \delta\nu/\pi$, $\mu = |\mu|e^{i\varphi_p}$, $|\mu|^2 = P_p/P_{th}$ is the ratio between the pump power P_p and the power P_{th} necessary to reach the threshold of the OPO.

These same parameters define the characteristics of the squeezed vacuum spectrum measured with homodyne detection (see the PhD thesis of Ana Predojević [Pre09] for further details):

$$S_{SV}(\omega) = 1 + \frac{4\eta_{det}|\mu|\eta\left[2|\mu| + \left(1+\omega^2\delta\nu^{-2}+|\mu|^2\right)\cos(2\varphi_{CS}-\varphi_p)\right]}{|A(\omega)|^2}, \tag{A.8}$$

where η_{det} is the detection efficiency, φ_{CS} and φ_p are the optical phases of the coherent state and the OPO pump, respectively. Figure A.1 shows the squeezing spectrum for realistic OPO parameters $\eta_{det} = 0.95$, $\eta = 0.93$, $\delta\nu = 8.4\pi$ MHz. We choose a pump power similar to the one we used in the experiments described in this thesis, so that $\mu = 0.09$.

Fourier transforms allow us to connect Eq. (A.2), which is in the frequency domain, to the correlation functions, which are expressed as function of time:

$$G^{(1)}_{V,V}(\tau) = \frac{1}{2\pi}\int d\omega_1 d\omega_2 \langle \hat{a}^\dagger_{\omega_1}\hat{a}_{\omega_2}\rangle e^{-i[\omega_1 t+\omega_2(t+\tau)]}, \tag{A.9}$$

where $\hat{a}_{\omega_i} = \hat{a}_V(\omega_i)$. Remembering that the fields associated to $\hat{a}_1$ and $\hat{a}_2$ are in the vacuum state, most of the terms that appear when we substitute (A.2) into (A.9) are equal to zero, so that we obtain

$$G^{(1)}_{V,V}(\tau) = \frac{1}{2\pi}\int d\omega \left[|f_2(\omega)|^2 + |f_4(\omega)|^2\right] e^{i\omega\tau}. \tag{A.10}$$

We compute

$$\int d\omega \frac{1}{|A(\omega)|^2} e^{i\omega\tau} = \frac{\pi\delta\nu}{2|\mu|(1-|\mu|^2)} e^{-\delta\nu|\tau|}\left[\sinh(\delta\nu|\mu\tau|) + |\mu|\cosh(\delta\nu|\mu\tau|)\right], \tag{A.11}$$

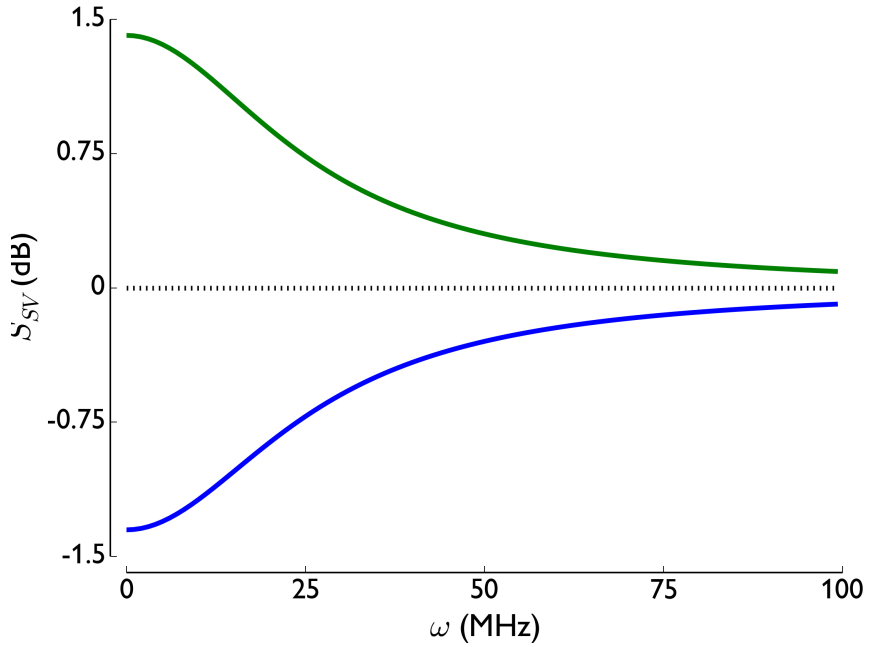

Figure A.1: Theoretical frequency spectrum of an OPO-generated squeezed vacuum state. The black dotted line represents the shot noise level, while the green and blue line are the anti-squeezed spectrum ($2\varphi_{CS} - \varphi_p = 0$) and squeezed spectrum ($2\varphi_{CS} - \varphi_p = \pi$), respectively. We take realistic values of the parameters: $\eta_{det} = 0.95$, $\eta = 0.93$, $\delta\nu = 8.4\pi$ MHz, $\mu = 0.09$.

so that the first order correlation function for the squeezed vacuum becomes:

$$\begin{aligned} G^{(1)}_{V,V}(\tau) &= \frac{\delta\nu\,|\mu|\,\eta}{1-|\mu|^2} e^{-\delta\nu|\tau|}\left[\sinh(\delta\nu|\mu\,\tau|) + |\mu|\cosh(\delta\nu|\mu\,\tau|)\right] \\ &= \Phi_S e^{-x}\left[\frac{1}{|\mu|}\sinh(|\mu|x) + \cosh(|\mu|x)\right], \end{aligned} \tag{A.12}$$

where $x \equiv \delta\nu\,|\tau|$ and Φ_S is the photon rate for the squeezed vacuum state:

$$\Phi_S \equiv G^{(1)}_{V,V}(0) = \frac{\delta\nu\,\eta\,|\mu|^2}{1-|\mu|^2}. \tag{A.13}$$

A.2 SECOND ORDER CORRELATION FUNCTION

Some second order correlation functions can easily be expressed as functions of the first order correlation functions:

$$G^{(2)}_{HV,HV}(\tau) = \langle\, \hat{a}^\dagger_H(t)\hat{a}^\dagger_V(t+\tau)\hat{a}_V(t+\tau)\hat{a}_H(t)\,\rangle \tag{A.14}$$

$$= G^{(2)}_{VH,VH}(-\tau) = G^{(1)}_{H,H}(0)G^{(1)}_{V,V}(0)\,, \tag{A.15}$$

$$G^{(2)}_{HV,VH}(\tau) = \langle\, \hat{a}^\dagger_H(t)\hat{a}^\dagger_{VV}(t+\tau)\hat{a}_H(t+\tau)\hat{a}_V(t)\,\rangle \tag{A.16}$$

$$= \left[G^{(2)}_{VH,HV}(\tau)\right]^* = G^{(1)}_{H,H}(\tau)G^{(1)}_{V,V}(-\tau)\,. \tag{A.17}$$

A.2.1 $G^{(2)}_{HH,HH}$

The rate of detection for coincident photons from the H-polarised coherent state is simply

$$G^{(2)}_{HH,HH} = {\Phi_C}^2\,. \tag{A.18}$$

A.2.2 $G^{(2)}_{HH,VV}$

We can factorise the terms corresponding to independent polarisation modes:

$$G^{(2)}_{HH,VV}(\tau) = \langle\, \hat{a}^\dagger_H(t)\,\hat{a}^\dagger_H(t+\tau)\,\rangle\,\langle\,\hat{a}_V(t+\tau)\,\hat{a}_V(t)\,\rangle\,. \tag{A.19}$$

The first factor is easy to compute:

$$\langle\, \hat{a}^\dagger_H(t)\,\hat{a}^\dagger_H(t+\tau)\,\rangle = \Phi_C e^{-2i\varphi_{CS}}. \tag{A.20}$$

As we did for the first-order correlation function, we use the Fourier transform on the second factor to get to the time domain, obtaining

$$\langle\,\hat{a}_V(t+\tau)\,\hat{a}_V(t)\,\rangle = \frac{1}{2\pi}\int d\omega_1 d\omega_2\,\langle\,\hat{a}_{\omega_1}\hat{a}_{\omega_2}\,\rangle e^{-i[\omega_1 t+\omega_2(t+\tau)]}\,. \tag{A.21}$$

As for the first order correlation function, we substitute a_ω with (A.2), so that most of the terms are trivial. We therefore get the simplified expression

$$\langle \hat{a}_{\omega_1} \hat{a}_{\omega_2} \rangle = [f_1(\omega_1)f_2(\omega_2) + f_3(\omega_1)f_4(\omega_2)]\,\delta(\omega_1+\omega_2)\,. \tag{A.22}$$

We compute

$$\int d\omega \frac{\omega^2}{|A(\omega)|^2} e^{i\omega t} = \frac{\pi\delta\nu^3}{2|\mu|} e^{-\delta\nu|\tau|}\left[|\mu|\cosh(\delta\nu|\mu\tau|) - \sinh(\delta\nu|\mu\tau|)\right]\,, \tag{A.23}$$

so that we obtain

$$\begin{aligned}
\langle \hat{a}_V(t+\tau)\,\hat{a}_V(t)\rangle &= \frac{1}{2\pi}\int d\omega\,[f_1(\omega)f_2(-\omega) + f_3(\omega)f_4(-\omega)]\,e^{i\omega t} \\
&= \frac{\mu\eta}{\pi}\int d\omega \frac{1}{|A(\omega)|^2}\left[|\mu|^2 + 1 + \frac{\omega^2}{\delta\nu^2}\right] e^{i\omega\tau} \\
&= \frac{\mu\eta}{\pi}\left\{\frac{(|\mu|^2+1)\pi\delta\nu\, e^{-\delta\nu|\tau|}}{2|\mu|(1-|\mu|^2)}\left[\sinh(\delta\nu|\mu\tau|) + |\mu|\cosh(\delta\nu|\mu\tau|)\right]\right. \\
&\quad \left. + \frac{\pi\delta\nu}{2|\mu|} e^{-\delta\nu|\tau|}\left[|\mu|\cosh(\delta\nu|\mu\tau|) - \sinh(\delta\nu|\mu\tau|)\right]\right\} \\
&= \frac{\mu\eta\,\delta\nu}{1-|\mu|^2} e^{-\delta\nu|\tau|}\left[|\mu|\sinh(\delta\nu|\mu\tau|) + \cosh(\delta\nu|\mu\tau|)\right] \\
&= \Phi_S e^{i\varphi_p - \chi}\left[\sinh(|\mu|x) + \frac{1}{|\mu|}\cosh(|\mu|x)\right]\,.
\end{aligned} \tag{A.24}$$

Finally, the second-order correlation function takes the form

$$G^{(2)}_{HH,VV}(\tau) = \Phi_C\Phi_S e^{i(\varphi_p - 2\varphi_{CS}) - \chi}\left[\sinh(|\mu|x) + \frac{1}{|\mu|}\cosh(|\mu|x)\right]\,. \tag{A.25}$$

A.2.3 $G^{(2)}_{VV,VV}$

We use the Fourier transform and the Bogoliubov transformation (A.2) similarly to what we did for the previous second-order correlation functions, with the difference that in this case there are more nonzero terms, as the average cannot be factorised:

$$\begin{aligned}
&\langle \hat{a}^\dagger_{\omega_1}\hat{a}^\dagger_{\omega_2}\hat{a}_{\omega_3}\hat{a}_{\omega_4}\rangle = \\
&\quad = A\delta(\omega_1+\omega_2)\delta(\omega_3+\omega_4) + B\delta(\omega_1-\omega_3)\delta(\omega_2-\omega_4) + C\delta(\omega_1-\omega_4)\delta(\omega_2-\omega_3),
\end{aligned} \tag{A.26}$$

where

$$A = [f_2^*(\omega_1)f_1^*(\omega_2) + f_4^*(\omega_1)f_3^*(\omega_2)]\,[f_1(\omega_3)f_2(\omega_4) + f_3(\omega_3)f_4(\omega_4)] \tag{A.27}$$

$$B = [f_2^*(\omega_1)f_2(\omega_3) + f_4^*(\omega_1)f_4(\omega_3)]\,[f_2^*(\omega_2)f_2(\omega_4) + f_4^*(\omega_2)f_4(\omega_4)] \tag{A.28}$$

$$C = [f_2^*(\omega_1)f_2(\omega_4) + f_4^*(\omega_1)f_4(\omega_4)]\,[f_2^*(\omega_2)f_2(\omega_3) + f_4^*(\omega_2)f_4(\omega_3)]\,. \tag{A.29}$$

$G^{(2)}_{VV,VV}$ is then a sum of integrals that simplify due to the delta functions in the expressions above:

$$G^{(2)}_{VV,VV}(\tau) = \mathcal{A} + \mathcal{B} + \mathcal{C}\,, \tag{A.30}$$

where

$$\begin{aligned}\mathcal{A} &= \frac{1}{(2\pi)^2}\int d\omega_1 d\omega_2 d\omega_3 d\omega_4 A\delta(\omega_1+\omega_2)\delta(\omega_3+\omega_4)e^{-i[\omega_1 t+\omega_2(t+\tau)-\omega_3(t+\tau)-\omega_4 t]} \\ &= |\langle\, \hat{a}_V(t+\tau)\hat{a}_V(t)\,\rangle|^2\,, \qquad (A.31)\\ \mathcal{B} &= \left[G^{(1)}_{V,V}(\tau)\right]^2\,, \qquad (A.32)\\ \mathcal{C} &= \left[\frac{1}{2\pi}\int d\omega\,\left(|f_2(\omega)|^2+|f_4(\omega)|^2\right)\right]^2 = {\Phi_S}^2\,. \qquad (A.33)\end{aligned}$$

We combine the expressions above with Eqs. (A.24) and (A.12), obtaining

$$G^{(2)}_{VV,VV}(\tau) = {\Phi_S}^2\left\{1+\frac{e^{-2x}}{|\mu|^2}\left[(1+|\mu|^2)\cosh(2|\mu|x)+2|\mu|\sinh(2|\mu|x)\right]\right\}. \tag{A.34}$$

The calculations reported in this Appendix give the elements of the two-photons ODM reported in Section 3.3.

BIBLIOGRAPHY

[AAS10] I. Afek, O. Ambar, and Y. Silberberg, *High-noon states by mixing quantum and classical light*, Science **328** (2010), 879–881.

[AAS+13] M. Abbarchi, A. Amo, V. G. Sala, D. D. Solnyshkov, H. Flayac, L. Ferrier, I. Sagnes, E. Galopin, A. Lemaitre, G. Malpuech, and J. Bloch, *Macroscopic quantum self-trapping and Josephson oscillations of exciton polaritons*, Nat Phys **9** (2013), 275–279.

[ASMS07] R. B. A. Adamson, L. K. Shalm, M. W. Mitchell, and A. M. Steinberg, *Multiparticle state tomography: Hidden differences*, Phys. Rev. Lett. **98** (2007), 043601.

[AWO+09] J. Appel, P. J. Windpassinger, D. Oblak, U. B. Hoff, N. Kjærgaard, and E. S. Polzik, *Mesoscopic atomic entanglement for precision measurements beyond the standard quantum limit*, Proc. Nat. Acad. Sci. **106** (2009), 10960–10965.

[BB94] I. Bialynicki-Birula, *On the wave function of the photon*, Acta Physica Polonica-Series A General Physics **86** (1994), 97–116.

[BCN+14] J. G. Bohnet, K. C. Cox, M. A. Norcia, J. M. Weiner, Z. Chen, and J. K. Thompson, *Reduced spin measurement back-action for a phase sensitivity ten times beyond the standard quantum limit*, Nature Photonics **8** (2014), 731–736.

[Bla01] E. D. Black, *An introduction to pound–drever–hall laser frequency stabilization*, American Journal of Physics **69** (2001), no. 1, 79–87.

[BLB+01] B. C. Buchler, P. K. Lam, H.-A. Bachor, U. L. Andersen, and T. C. Ralph, *Squeezing more from a quantum nondemolition measurement*, Physical Review A **65** (2001), 011803.

[BM13] Federica A. Beduini and Morgan W. Mitchell, *Optical spin squeezing: Bright beams as high-flux entangled photon sources*, Phys. Rev. Lett. **111** (2013), 143601.

[BMCC+14] N. Behbood, F. Martin Ciurana, G. Colangelo, M. Napolitano, G. Tóth, R. J. Sewell, and M. W. Mitchell, *Generation of macroscopic singlet states in a cold atomic ensemble*, Phys. Rev. Lett. **113** (2014), 093601.

[BTSL02] W. P. Bowen, N. Treps, R. Schnabel, and P. K. Lam, *Experimental demonstration of continuous variable polarization entanglement*, Phys. Rev. Lett. **89** (2002), 253601.

[BvFB+13] T. Berrada, S. van Frank, R. Bücker, T. Schumm, J.-F. Schaff, and J. Schmiedmayer, *Integrated mach–zehnder interferometer for bose–einstein condensates*, Nature communications **4** (2013).

[BZL+14] F. A. Beduini, J. A. Zielińska, V. G. Lucivero, Y. A. de Icaza Astiz, and M. W. Mitchell, *Interferometric measurement of the biphoton wave function*, Phys. Rev. Lett. **113** (2014), 183602.

[BZL+15] F. A. Beduini, J. A. Zielińska, V. G. Lucivero, Y. A. de Icaza Astiz, and M. W. Mitchell, *Macroscopic quantum state analyzed particle by particle*, Phys. Rev. Lett. **114** (2015), 120402.

[CBS+11] Z. Chen, J. G. Bohnet, S. R. Sankar, J. Dai, and J. K. Thompson, *Conditional spin squeezing of a large ensemble via the vacuum rabi splitting*, Phys. Rev. Lett. **106** (2011), 133601.

[CDMP+06] M. Caminati, F. De Martini, R. Perris, F. Sciarrino, and V. Secondi, *Nonseparable werner states in spontaneous parametric down-conversion*, Physical Review A **73** (2006), no. 3, 032312.

[CG84] M. J. Collett and C. W. Gardiner, *Squeezing of intracavity and traveling-wave light fields produced in parametric amplification*, Physical Review A **30** (1984), 1386.

[CKW00] V. Coffman, J. Kundu, and W. K. Wootters, *Distributed entanglement*, Phys. Rev. A **61** (2000), 052306.

[CSG+15] P Chen, C. Shu, X. Guo, M.T̃. Loy, M. and S. Du, *Measuring the biphoton temporal wave function with polarization-dependent and time-resolved two-photon interference*, Phys. Rev. Lett. **114** (2015), 010401.

[DEW+13] T. Douce, A. Eckstein, S. P. Walborn, A. Z. Khoury, S. Ducci, A. Keller, T. Coudreau, and P. Milman, *Direct measurement of the biphoton wigner function through two-photon interference*, Scientific reports **3** (2013).

[dIA15] Y. A. de Icaza Astiz, *Optimal signal recovery for pulsed balanced detection*, Ph.D. thesis, ICFO - The Institute of Photonic Sciences and Universidad Politècnica de Catalunya, 2015.

[DPFS04] B. Dayan, A. Pe'er, A. A. Friesem, and Y. Silberberg, *Two photon absorption and coherent control with broadband down-converted light*, Phys. Rev. Lett. **93** (2004), 023005.

[FLS65] R. P. Feynman, R. B. Leighton, and M. Sands, *Lectures on physics, vol. iii*, Addison-Wesley Reading, Mass., 1965.

[FPL+13] O. Firstenberg, T. Peyronel, Q.-Y. Liang, A. V. Gorshkov, M. D. Lukin, and V. Vuletic, *Attractive photons in a quantum nonlinear medium*, Nature **502** (2013), 71–75.

[Fra89] J. D. Franson, *Bell inequality for position and time*, Physical Review Letters **62** (1989), 2205.

[FRCdR13] J. Fekete, D. Rieländer, M. Cristiani, and H. de Riedmatten, *Ultranarrow-band photon-pair source compatible with solid state quantum memories and telecommunication networks*, Phys. Rev. Lett. **110** (2013), 220502.

[GHZ93] D. M. Greenberger, M. A. Horne, and A. Zeilinger, *Multiparticle interferometry and the superposition principle*, Physics Today **46** (1993), 22–22.

[Gla63] Roy J. Glauber, *The quantum theory of optical coherence*, Phys. Rev. **130** (1963), 2529–2539.

[GM87] R. Ghosh and L. Mandel, *Observation of nonclassical effects in the interference of two photons*, Physical Review Letters **59** (1987), 1903.

[GMSW02] Vittorio Giovannetti, Lorenzo Maccone, Jeffrey H. Shapiro, and Franco N. C. Wong, *Extended phase-matching conditions for improved entanglement generation*, Phys. Rev. A **66** (2002), 043813.

[GRA86] P. Grangier, G. Roger, and A. Aspect, *Experimental evidence for a photon anticorrelation effect on a beam splitter: a new light on single-photon interferences*, EPL (Europhysics Letters) **1** (1986), 173.

[GT09] O. Gühne and G. Tóth, *Entanglement detection*, Physics Reports **474** (2009), 1 – 75.

[GTB05] O. Gühne, G. Tóth, and H. J. Briegel, *Multipartite entanglement in spin chains*, New Journal of Physics **7** (2005), 229.

[GZN+10] C. Gross, T. Zibold, E. Nicklas, J. EstÃ¨ve, and M. K. Oberthaler, *Nonlinear atom interferometer surpasses classical precision limit*, Nature **464** (2010), 1165–1169.

[HHH96a] M. Horodecki, P. Horodecki, and R. Horodecki, *Separability of mixed states: necessary and sufficient conditions*, Physics Letters A **223** (1996), 1.

[HHH96b] R. Horodecki, M. Horodecki, and P. Horodecki, *Teleportation, bell's inequalities and inseparability*, Phys. Lett. A **222** (1996), 21.

[HOM87] C. K. Hong, Z. Y. Ou, and L. Mandel, *Measurement of subpicosecond time intervals between two photons by interference*, Physical Review Letters **59** (1987), 2044.

[HPS10] P. Hyllus, L. Pezzé, and A. Smerzi, *Entanglement and sensitivity in precision measurements with states of a fluctuating number of particles*, Phys. Rev. Lett. **105** (2010), 120501.

[Hu13] M.-L. Hu, *Relations between entanglement, bell-inequality violation and teleportation fidelity for the two-qubit x states*, Quantum information processing **12** (2013), 229–236.

[JKMW01] D. F. V. James, P. G. Kwiat, W. J. Munro, and A. G. White, *Measurement of qubits*, Phys. Rev. A **64** (2001), 052312.

[KBŻ+06] R. Kaltenbaek, B. Blauensteiner, M. Żukowski, M. Aspelmeyer, and A. Zeilinger, *Experimental interference of independent photons*, Physical review letters **96** (2006), 240502.

[KCL05] J. K. Korbicz, J. I. Cirac, and M. Lewenstein, *Spin squeezing inequalities and entanglement of N qubit states*, Physical Review Letters **95** (2005), 120502.

[KGL+06] J. K. Korbicz, O. Gühne, M. Lewenstein, H. Häffner, C. F. Roos, and R. Blatt, *Generalized spin-squeezing inequalities in n-qubit systems: Theory and experiment*, Phys. Rev. A **74** (2006), 052319.

[KLL+02] N. Korolkova, G. Leuchs, R. Loudon, T. C. Ralph, and C. Silberhorn, *Polarization squeezing and continuous-variable polarization entanglement*, Phys. Rev. A **65** (2002), 052306.

[KM98] A. Kuzmich and L. Mandel, *Sub-shot-noise interferometric measurements with two-photon states*, Quantum and Semiclassical Optics: Journal of the European Optical Society Part B **10** (1998), 493.

[KSVW10] J. Klaers, J. Schmitt, F. Vewinger, and M. Weitz, *Bose-einstein condensation of photons in an optical microcavity*, Nature **468** (2010), 545–548.

[KU93] M. Kitagawa and M. Ueda, *Squeezed spin states*, Phys. Rev. A **47** (1993), 5138–5143.

[KWKT08] O. Kuzucu, F. N. C. Wong, S. Kurimura, and Se. Tovstonog, *Joint temporal density measurements for two-photon state characterization*, Phys. Rev. Lett. **101** (2008), 153602.

[LK06] A. Luis and N. Korolkova, *Polarization squeezing and nonclassical properties of light*, Phys. Rev. A **74** (2006), 043817.

[LO01] Y. J. Lu and Z. Y. Ou, *Observation of nonclassical photon statistics due to quantum interference*, Phys. Rev. Lett. **88** (2001), 023601.

[LSSV10] I. D. Leroux, M. H. Schleier-Smith, and V. Vuletic, *Implementation of cavity squeezing of a collective atomic spin*, Phys. Rev. Lett. **104** (2010), 073602.

[MAE+11] M. Mehmet, S. Ast, T. Eberle, S. Steinlechner, H. Vahlbruch, and R. Schnabel, *Squeezed light at 1550 nm with a quantum noise reduction of 12.3 db*, Opt. Express **19** (2011), 25763–25772.

[Man99] L. Mandel, *Quantum effects in one-photon and two-photon interference*, Rev. Mod. Phys. **71** (1999), S274–S282.

[MB14] M. W. Mitchell and F. A. Beduini, *Extreme spin squeezing for photons*, New Journal of Physics **16** (2014), 073027.

[MFL13] O. Morin, C. Fabre, and J. Laurat, *Experimentally accessing the optimal temporal mode of traveling quantum light states*, Phys. Rev. Lett. **111** (2013), 213602.

[MLS04] M. W. Mitchell, J. S. Lundeen, and A. M. Steinberg, *Super-resolving phase measurements with a multiphoton entangled state*, Nature **429** (2004), 161–164 (English).

[MLS+08] P. J. Mosley, J. S. Lundeen, B. J. Smith, P. Wasylczyk, A. B. U'Ren, C. Silberhorn, and I. A. Walmsley, *Heralded generation of ultrafast single photons in pure quantum states*, Phys. Rev. Lett. **100** (2008), 133601.

[MMG+05] K. McKenzie, E. E Mikhailov, K. Goda, P. K. Lam, N. Grosse, M. B. Gray, N. Mavalvala, and D. E. McClelland, *Quantum noise locking*, Journal of Optics B: Quantum and Semiclassical Optics **7** (2005), S421.

[MSL+14] W. Müssel, H. Strobel, D. Linnemann, D. B. Hume, and M. K. Oberthaler, *Scalable spin squeezing for quantum-enhanced magnetometry with bose-einstein condensates*, Physical review letters **113** (2014), 103004.

[NNNH+06] J. S. Neergaard-Nielsen, B. Melholt Nielsen, C. Hettich, K. Mølmer, and E. S. Polzik, *Generation of a superposition of odd photon number states for quantum information networks*, Phys. Rev. Lett. **97** (2006), 083604.

[NOO+07] T. Nagata, R. Okamoto, J. L. O'Brien, K. Sasaki, and S. Takeuchi, *Beating the standard quantum limit with four-entangled photons*, Science **316** (2007), 726–729.

[NW49] T. D. Newton and E. P. Wigner, *Localized states for elementary systems*, Reviews of Modern Physics **21** (1949), 400.

[OSRT13] C. F. Ockeloen, R. Schmied, M. F. Riedel, and P. Treutlein, *Quantum metrology with a scanning probe atom interferometer*, Physical review letters **111** (2013), 143001.

[OTS06] R. Okamoto, S. Takeuchi, and K. Sasaki, *Tailoring two-photon interference with phase dispersion*, Phys. Rev. A **74** (2006), 011801.

[OU09] K. A. O'Donnell and A. B. U'Ren, *Time-resolved up-conversion of entangled photon pairs*, Phys. Rev. Lett. **103** (2009), 123602.

[PDFS05] A. Pe'er, B. Dayan, A. A. Friesem, and Y. Silberberg, *Temporal shaping of entangled photons*, Phys. Rev. Lett. **94** (2005), 073601.

[Per96] A. Peres, *Separability criterion for density matrices*, Physical Review Letters **77** (1996), 1413.

[PLB+09] G. Puentes, J. S. Lundeen, M. P. A. Branderhorst, H. B. Coldenstrodt-Ronge, B. J. Smith, and I. A. Walmsley, *Bridging particle and wave sensitivity in a configurable detector of positive operator-valued measures*, Phys. Rev. Lett. **102** (2009), 080404.

[Pre09] A. Predojević, *Rubidium resonant squeezed light from a diode-pumped optical-parametric oscillator*, Ph.D. thesis, ICFO-Institut de Ciències Fòtoniques and Departement de Física Aplicada y Simulación en Ciencias de Universidad Politècnica de Catalunya, 2009.

[PZCM08] A. Predojević, Z. Zhai, J. M. Caballero, and M. W. Mitchell, *Rubidium resonant squeezed light from a diode-pumped optical-parametric oscillator*, Physical Review A **78** (2008), 63820.

[QPB+15] Z. Qin, A. S. Prasad, T. Brannan, A. MacRae, A. Lezama, and A. I. Lvovsky, *Complete temporal characterization of a single photon*, Light: Science Applications **4** (2015), e298.

[Rad71] J. M. Radcliffe, *Some properties of coherent spin states*, Journal of Physics A: General Physics **4** (1971), 313.

[RBL03] J. Ries, B. Brezger, and A. I. Lvovsky, *Experimental vacuum squeezing in rubidium vapor via self-rotation*, Phys. Rev. A **68** (2003), 025801.

[RH12] C. Ren and H. F. Hofmann, *Analysis of the time-energy entanglement of down-converted photon pairs by correlated single-photon interference*, Phys. Rev. A **86** (2012), 043823.

[SA88] Y. H. Shih and C. O. Alley, *New type of einstein-podolsky-rosen-bohm experiment using pairs of light quanta produced by optical parametric down conversion*, Physical Review Letters **61** (1988), 2921.

[SAKYH09] S. Sensarn, I. Ali-Khan, G. Y. Yin, and S. E. Harris, *Resonant sum frequency generation with time-energy entangled photons*, Phys. Rev. Lett. **102** (2009), 053602.

[SBRF93] D. T. Smithey, M. Beck, M. G. Raymer, and A. Faridani, *Measurement of the wigner distribution and the density matrix of a light mode using optical homodyne tomography: Application to squeezed states and the vacuum*, Phys. Rev. Lett. **70** (1993), 1244–1247.

[SDCZ01] A. Sørensen, L.-M Duan, J. I. Cirac, and P. Zoller, *Many-particle entanglement with bose-einstein condensates*, Nature **409** (2001), 63–66.

[Sip95] J. E. Sipe, *Photon wave functions*, Physical Review A **52** (1995), 1875.

[SKN+12] R. J. Sewell, M. Koschorreck, M. Napolitano, B. Dubost, N. Behbood, and M. W. Mitchell, *Magnetic sensitivity beyond the projection noise limit by spin squeezing*, Phys. Rev. Lett. **109** (2012), 253605.

[SM01] A. S. Sørensen and K. Mølmer, *Entanglement and extreme spin squeezing*, Phys. Rev. Lett. **86** (2001), 4431–4434.

[SR07] B. J. Smith and M. G. Raymer, *Photon wave functions, wave-packet quantization of light, and coherence theory*, New Journal of Physics **9** (2007), 414.

[SSR95] A. V. Sergienko, Y. H. Shih, and M. H. Rubin, *Experimental evaluation of a two-photon wave packet in type-ii parametric downconversion*, JOSA B **12** (1995), no. 5, 859–862.

[SZ97] M. O. Scully and M. S. Zubairy, *Quantum optics*, Cambridge University Press, 1997.

[TM97] J. R. Torgerson and L. Mandel, *Photon antibunching in downconverted light*, J. Opt. Soc. Am. B **14** (1997), 2417–2423.

[VCS+07] A. Valencia, A. Ceré, X. Shi, G. Molina-Terriza, and J. P. Torres, *Shaping the waveform of entangled photons*, Phys. Rev. Lett. **99** (2007), 243601.

[VHET11] G. Vitagliano, P. Hyllus, I. L. Egusquiza, and G. Tóth, *Spin squeezing inequalities for arbitrary spin*, Phys. Rev. Lett. **107** (2011), 240502.

[WBI+92] D. J. Wineland, J. J. Bollinger, W. M. Itano, F. L. Moore, and D. J. Heinzen, *Spin squeezing and reduced quantum noise in spectroscopy*, Phys. Rev. A **46** (1992), R6797–R6800.

[WBIH94] D. J. Wineland, J. J. Bollinger, W. M. Itano, and D. J. Heinzen, *Squeezed atomic states and projection noise in spectroscopy*, Phys. Rev. A **50** (1994), 67–88.

[WCB+10] F. Wolfgramm, A. Cerè, F. A. Beduini, A. Predojević, M. Koschorreck, and M. W. Mitchell, *Squeezed-light optical magnetometry*, Physical Review Letters **105** (2010), 53601.

[WM02] X. Wang and K. Mølmer, *Pairwise entanglement in symmetric multi-qubit systems*, The European Physical Journal D **18** (2002), 385.

[Woo98] W. K. Wootters, *Entanglement of Formation of an Arbitrary State of Two Qubits*, Physical Review Letters **80** (1998), 2245.

[WS03] X. Wang and B. C. Sanders, *Spin squeezing and pairwise entanglement for symmetric multiqubit states*, Phys. Rev. A **68** (2003), 012101.

[WVB+13] F. Wolfgramm, C. Vitelli, F. A. Beduini, N. Godbout, and M. W. Mitchell, *Entanglement-enhanced probing of a delicate material system*, Nat Photon **7** (2013), 28–32.

[WXC+08] F. Wolfgramm, X. Xing, A. Cerè, A. Predojević, A. M. Steinberg, and M. W. Mitchell, *Bright filter-free source of indistinguishable photon pairs*, Opt. Express **16** (2008), no. 22, 18145–18151.

[ZANW12] J. A. Zielińska, Beduini F. A., Godbout N., and Mitchell M. W., *Ultranarrow Faraday rotation filter at the Rb D_1 line*, Opt. Lett. **37** (2012), 524–526.

[ZBLM14] J. A. Zielińska, F. A. Beduini, V. G. Lucivero, and M. W. Mitchell, *Atomic filtering for hybrid continuous-variable/discrete-variable quantum optics*, Optics Express **22** (2014), 25307–25317.

ACKNOWLEDGEMENTS

So long, and thanks for all the fish.

Douglas Adams, *The Hitchhiker's Guide to the Galaxy*

The first person to be acknowledged for this thesis is of course my supervisor, the Professor Morgan Mitchell. I learned innumerable things from him, who has always been there for clear explanations and wise advices. I appreciate a lot his way to support my work and at the same time to push me to improve it. These few words are not sufficient to express my gratitude, but I hope he knows how much I owe him.

The work behind this thesis would not have been possible nor so pleasant without the people of the *light* side of the group, with whom I spent so many hours wandering and wondering in the dark. I thank Alessandro, Florian (who taught me practically everything I know about the lab), Yannick (who adopted me since the beginning and introduced me to the ICFO world), Chiara (for her delightful mix of physics and gossip), Joanna (who chose to come back to our group after she had to stand me as a supervisor for a whole summer). Jia and Ricardo joined the group near the end of my thesis, so I spent more lunch time than lab time with them, but this doesn't mean that I have enjoyed less the time I spent with them. Last, but not least, the amazing Gianvito, who can recover the faintest signal with his magic fingers, cheer you up with just few words, and transform the lab in a disco.

From the *dark* side of the group, I cannot avoid to mention il presidente Mario, Naeimeh, who cared for all of us as a loving mum, and Giorgio, il mio bastian contrario preferito.

I owe a lot also to my officemates. First of all, Rob, who has been there for the longest time and who supported me and was at my side in a wide spectrum of activities that range from physics, to capoeira, bike rides and extreme walks, among the other things. Thanks also to Ferran, who always gets my jokes, even the worst ones (he knows that this is one of the best compliments). I cannot forget also my other officemate, Silvana, who had a very good taste to choose the posters for the office, and her lab mates, Thomas, Natali and Simon.

Thanks also to the numerous other Icfonians who made my work possible and my time here pleasant, but I'm afraid they are so many that I cannot list them all.

I also have to thank a huge group of people who made my first summer in Barcelona unforgettable: we had so much fun that we still keep in contact somehow even if we are scattered around the world. I hope not to forget anybody, but my life in Barcelona would have probably been not so happy if I hadn't started without Laura, Oliver, Felix, Sashka, Masha, Candan, Guillermo, Sabine, Pierre, Rafa, Daan, Koen, Lars, Osamu, Alex, Jordi, don Roberto, Valeria, and continued with Carmelo, Claudia, Luis José y la profe, mi nieto Roland, Lisa, Mustafa y Alessandro.

Some of the people I met that year played a special role in my life, becoming close and sincere friends. First of all, Mariale, who always stayed by my side, Philipp, the funniest German I've ever met, Nadia, with whom I got along from the first nanosecond, Michela, who continues talking to me even if she knows it can be dangerous, Gonzalo, who is never tired of talking with me for hours and hours about the craziest stuff, and Giacomo, my adoptive son.

I am very grateful also to the Professor Alejandra Valencia, who gave me in advance a wonderful gift for ending my PhD. Thanks also to all the group of Quantum Optics of the Universidad de los Andes in Bogotá for their warm welcome and for all the scientific (and not only) exchange.

Muito obrigada ao meu professor de capoeira Quirze/Cavalo e a tuda a galera do Palmares para todos os ensinamentos e o axé. They made my days lighter and gave my the energy to go on fighting, not only in the roda, but also in the lab.

I owe the happiness during these years not only to people here in Barcelona, but also to the ones I left in Italy, who they still make me feel as I never left. I must mention i ragazzi di via Celoria: la Giulia e Simone, la Cé, la Francy, la Ele, il Costa, il Robbo, il Manfredda (e le sue innumerevoli assenze) e le new entries Edoardo e Guido. Va ricordata anche la mia relazione a distanza con Ross, che è probabilmente l'unico non membro della mia famiglia che ha il record di visite e chiamate via Skype. Il vecchio Andrea Mac Cherry ancora non mi perdona di averlo abbandonato: inutili i tentativi di spiegargli che questo mio viaggio a Barcellona servisse solo per racimolare un po' di soldi per comprare la nostra tanto agognata distilleria di whisky nel Tennessee. Le ragioni per ringraziare il mitico Bella!Teo sono varie e numerose: prima fra tutte quella di far contenta la Lu, impresa assai ardua. Ho lasciato in fondo la Lu, solo perché è difficile dire a parole quello che le devo: ha sempre saputo qual era la scelta migliore per me – anche prima di me – e mi ha sempre appoggiato nelle mie imprese. Soprattutto, però, è sempre la mia amica, nonostante il tempo passi e le distanze crescano.

Un grazie infinite ai miei genitori, che mi sono sempre stati vicini, nonostante la distanza fisica. Se oggi sono arrivata fino a qui, lo devo soprattutto a loro e non posso fare altro che ringraziarli per tutto ciò che mi hanno dato ed insegnato. Devo ringraziare qui, perché dal vivo non lo faccio mai abbastanza, il mio fratellone Nicolò, che da sempre è il mio fan numero 1 e non fa altro che dimostrarlo. I ringraziamenti alla mia famiglia non si esauriscono qui, ma si estendono a tutta la grande tribù dei Beduini, di cui sono orgogliosa di essere membro ufficiale, e quella un po' più piccola dei Sanvito.

Gracias también a mi familia española adoptiva, la de los Paredes-Barato, que siempre me acogen como si hubiese estado con ellos desde siempre.

Por fin, llego a agradecer mi compañero de piso preferido, el Doctor David S., que nunca se olvidó de cuidarme a mi y a mi menta, a pesar de la distancia. Con él he compartido – y sigo compartiendo – aventuras, postrulzes, palabras y risas a carcajadas. Es mi consultor oficial y mi fuente de energia y espero seguir aprovechandome de él por mucho tiempo.